

POLITECNICO DI TORINO

Master's Degree in Electronic Engineering



Master's Degree Thesis

Numerical Computation of High Frequency Wave Propagation in Complex Media

Supervisors

Prof. GIUSEPPE VECCHI

Dr. ANDREA SCARABOSIO

Candidate

LEONARDO DI VINCENZO

07/2022

Abstract

The link communication from/to satellite, re-entry or space vehicles is often subject to degradation known as black-out. To assess this issue, radio frequency (RF) wave propagation through complex media (such as ionosphere, plasmas and complex gas mixtures) must be considered. Asymptotic techniques such as ray or beam tracing can be used to predict EM propagation in these inhomogeneous media where the radiation can be refracted, reflected and/or absorbed compared to free-space propagation. Coupled with integral equations for the free-space part of the simulation domain the model provides a powerful numerical tool to design antennas for critical applications and for calculating the Radar Cross Section (RCS) of objects surrounded by complex media such as hypersonic plasma. The ray tracing method effectively decomposes the wavefront with plane wave represented by one or more rays and follow the propagation using the Eikonal approximation valid for short wavelength. Contrary to ray tracing in homogeneous media, where the ray trajectories are straight lines, here a ray can be curved due to the continuous variation of the refractive index (inhomogeneity). A numerical code capable of simulating the behavior of rays and following their trajectory within complex media has been developed at LINKS Foundation. One of the limitations of this model and consequently of the numerical code is the fact that in order to have reliable results, a sufficiently dense grid of rays must be generated which interacts with objects in the "scene" while traversing it (ray traversal); this involves an enormous amount of computational time. The first part of this thesis work focused precisely on this problem: speeding up the ray traversal process; this was done by using special data structures such as K-D Trees or Octrees that can subdivide the physical space (the scene) into boxes and then through an appropriate traversal algorithm identify which boxes were hit by the ray in such a way as to follow its trajectory. In the second part, on the contrary, improvements were made to the physical model, thus enabling the simulation of electromagnetic scattering situations not present in the original code, that were limited to the calculation of the Radar Cross Section considering only perfectly reflective and impenetrable surfaces (PEC); in particular the equations for boundary surfaces between different and possibly lossy dielectrics have been introduced, enabling the simulation of scattering with penetrable dielectrics bodies with sharp boundaries. Due to the secondary rays generated at the discontinuities the bookkeeping of rays is more complicated and has to be implemented efficiently. As initial test cases, the Radar Cross Section of dielectric spheres was calculated and compared with the results obtained with exact solutions derived from Mie's series.

*“Born To Lose, Live To Win”
Lemmy Kilmister*

Table of Contents

| | |
|--|-----------|
| List of Tables | VI |
| List of Figures | VII |
| Acronyms | XII |
| 1 Introduction | 1 |
| 2 High Frequency Wave in Complex Media | 3 |
| 2.1 Electromagnetic Wave | 3 |
| 2.1.1 Maxwell's Equations | 3 |
| 2.1.2 Material Equations | 4 |
| 2.1.3 The wave equation and the velocity of light | 5 |
| 2.1.4 Plane Wave | 6 |
| 2.1.5 Time-Harmonic Waves | 8 |
| 2.1.6 The laws of refraction and reflection | 10 |
| 2.1.7 Fresnel formulae | 12 |
| 2.2 Complex Media | 15 |
| 2.3 Geometrical Optics and Ray Theory | 17 |
| 2.3.1 Approximation for very short wavelengths | 17 |
| 2.3.2 Eikonal equation for <i>GO</i> | 17 |
| 2.3.3 The light rays and the intensity law of geometrical optics . . | 19 |
| 2.3.4 The differential equation of light rays | 22 |
| 2.4 Electromagnetic Scattering | 25 |
| 2.4.1 Definition of RCS | 27 |
| 2.4.2 RCS prediction techniques | 30 |
| 3 LACE RT Code | 36 |
| 3.1 Physical Model | 37 |
| 3.2 Numerical Model | 39 |
| 3.2.1 Ray Tube Approach | 41 |

| | | |
|----------|--|-----------|
| 4 | Methods for Fast Ray Tracing | 45 |
| 4.1 | Spatial Subdivision | 46 |
| 4.1.1 | Octree | 46 |
| 4.1.2 | K-D Tree | 47 |
| 4.2 | K-D Tree vs. Octree | 49 |
| 4.3 | Ray Traversal algorithm using K-D Tree | 52 |
| 4.3.1 | Point Location | 55 |
| 4.3.2 | Ray Traversal | 59 |
| 4.4 | Benchmark of Numerical Model | 64 |
| 4.5 | Ray Tracing for a 'Segmented' Ray | 65 |
| 5 | Electromagnetic Scattering by Penetrable Dielectric using up- graded LACE RT Code | 68 |
| 5.1 | Formulation of the Scattering Problem | 69 |
| 5.2 | Reflection/Refraction at the Curved Scatterer Boundary | 70 |
| 5.2.1 | Numerical Simulation of Ray Trajectories | 71 |
| 5.3 | Correct bookkeeping of rays | 72 |
| 5.4 | Test Cases & Numerical Results | 74 |
| 5.4.1 | Dielectric With Losses | 74 |
| 5.4.2 | Dielectric Without Losses | 80 |
| 6 | Summary & Conclusions | 83 |
| A | Discussion on Eikonal validity for inhomogeneous media | 87 |
| B | Octree/K-D Tree comparison for different geometries | 89 |
| C | Benchmark of Numerical Model | 91 |
| D | Fresnel Coefficients for Lossy Materials | 93 |
| D.1 | TE Polarization | 93 |
| D.2 | TM Polarization | 95 |
| D.3 | True Angle of Refraction | 96 |
| | Bibliography | 97 |

List of Tables

| | | |
|-----|--|----|
| 4.1 | The first line refers to 30% of the points, the second to 10%, and the last to 1%. | 49 |
| 4.2 | The first line refers to 30% of the points, the second to 10%, and the last to 1%. | 49 |
| 4.3 | The first line refers to 30% of the points, the second to 10%, and the last to 1%. | 50 |
| 4.4 | The first line refers to 30% of the points, the second to 10%, and the last to 1%. | 50 |
| 4.5 | Neighbor-Link | 61 |

List of Figures

| | | |
|------|---|----|
| 2.1 | Plane wave propagation | 7 |
| 2.2 | Wave fronts | 7 |
| 2.3 | Illustration of the laws of reflection and refraction | 10 |
| 2.4 | Illustration of the laws of refraction(a) and reflection(b) | 11 |
| 2.5 | Refraction and reflection of a plane wave. Plane of incidence | 12 |
| 2.6 | Two different dispersion curves: a) non-dispersive medium, b) dispersive medium | 15 |
| 2.7 | Diagram of dispersion in Newton's prism | 16 |
| 2.8 | Illustrating the meaning of the relation $ns = \nabla S$ | 20 |
| 2.9 | Illustrating the intensity law | 21 |
| 2.10 | Illustrating the 'curved' ray | 23 |
| 2.11 | Bending a ray in a inhomogeneous(complex) medium | 24 |
| 2.12 | Concept of RCS | 27 |
| 2.13 | RCS of a perfectly conducting sphere as a function of its electrical size ka | 28 |
| 2.14 | Log-log plot of the data displayed in Fig. 2.13 | 29 |
| 2.15 | The MoM divides the body surface into a collection of discrete patches | 33 |
| 2.16 | The GO RCS of a doubly curved surface depends on the principal radii of curvature at the specular point. The specular point is that point on the surface where the surface normal points toward the radar | 34 |
| 3.1 | Algorithm overview with input and output data. | 36 |
| 3.2 | Schematic of the physical model. Inhomogeneous media (here plasma surrounding a vessel) are enclosed by an equivalent surface (dashed red line) on which equivalent currents radiate to the outside. | 38 |
| 3.3 | Sketch of the adopted ray tube propagation scheme. | 41 |
| 3.4 | Ray trajectories (red lines) from a dipole source above a small simplified vessel, in free space. The spherical equivalence surface is also depicted (coloured). | 44 |
| 3.5 | Electric field on a spherical equivalent surface for the configuration in Fig. 3.4. | 44 |

| | | |
|------|---|----|
| 4.1 | Generation of the spatial subdivision (left) and the corresponding data structure (right) | 47 |
| 4.2 | Octree Example | 47 |
| 4.3 | A 3-dimensional k-d tree. The first split (the red vertical plane) cuts the root cell (white) into two subcells, each of which is then split (by the green horizontal planes) into two subcells. Finally, four cells are split (by the four blue vertical planes) into two subcells. Since there is no more splitting, the final eight are called leaf cells. | 48 |
| 4.4 | Spatial subdivision using Octree | 51 |
| 4.5 | Spatial subdivision using K-D Tree | 51 |
| 4.6 | Simple scene with three triangles with a corresponding kd-tree with three leaves (boxes) and three inner nodes (circles). | 53 |
| 4.7 | Pseudo-code for Point Location[8] | 53 |
| 4.8 | Pseudo-code for Sequential(Classic) Ray Traversal[8] | 54 |
| 4.9 | Test on the CLASSIC point location module | 57 |
| 4.10 | Test on the INTEGER point location module | 57 |
| 4.11 | Flowchart of the new INTEGER location module | 58 |
| 4.12 | Sequential Traversal (100 rays):the blue asterisks indicate the points of intersection between the rays and the mesh found using the Brut Force method while in red those found using the K-D Tree (the spatial subdivision structure has been omitted for image clarity). | 60 |
| 4.13 | Orientation of a leaf box in the 3D space | 61 |
| 4.14 | Neighbor-Link Test | 62 |
| 4.15 | Test Neighbor-Link Traversal (100 rays):the blue asterisks indicate the points of intersection between the rays and the mesh found using the Brut Force method while in yellow those found using the K-D Tree with Neighbor-Link (the spatial subdivision structure has been omitted for image clarity). | 63 |
| 4.16 | Computational Time Performance (Vehicle) | 64 |
| 4.17 | Benchmark for the segmented version of the Ray Tracing | 66 |
| 4.18 | Testing the algorithm adapted to the segmented line. From the figure, the ray constructed using line segments can be seen and in green the point of impact with the geometry is highlighted confirming that the algorithm works correctly. | 67 |
| 5.1 | Geometry of the Scattering Problem | 69 |
| 5.2 | Local coordinate systems for the incident, reflected and refracted rays at the scatterer boundary. | 70 |

| | | |
|------|---|----|
| 5.3 | Results of simulation of ray reflections and refractions for an homogeneous dielectric sphere with $\epsilon_r = 14$. Two focal points can be seen: one inside the sphere generated by the the refracted wavefront at the first boundary; and one just outside the sphere generated by the wavefront encountering the boundaries three times and being transmitted-reflected-transmitted respectively. | 72 |
| 5.4 | Schematic of the operation of the numerical code with the new modules. | 73 |
| 5.5 | RCS for increasing ϵ_r and $ka=35$ | 75 |
| 5.6 | Monostatic RCS of a sphere. PEC and lossy characterization using the MECA method taken from [12]. An high degree of overlapping in the curves of Mie and MECA clearly demonstrates the accuracy of the high frequency technique. | 76 |
| 5.7 | RCS comparison for increasing ka and fixed ϵ (2.2). The trend described turns out to be very similar to that in Fig. 5.6; this goes to confirm what was said earlier, namely, that even in areas where the solutions is not exact, the hybrid code tends to behave like the MECA numerical method for dielectrics and like the PO for PEC[5] | 77 |
| 5.8 | RCS comparison for $ka=10$ ($\phi = 0$); θ Polarization | 78 |
| 5.9 | RCS comparison for $ka=10$ ($\phi = 90$); θ Polarization | 78 |
| 5.10 | RCS comparison for $ka=35$ ($\phi = 0$); θ Polarization | 79 |
| 5.11 | RCS comparison for $ka=35$ ($\phi = 90$); θ Polarization | 79 |
| 5.12 | RCS comparison ($\epsilon_r = 30$) considering 3 reflections. Improvement can be observed in the calculation of back and forward scattering but a deterioration in the 'lateral' part of the field. | 81 |
| 5.13 | RCS comparison ($\epsilon_r = 14$) considering 3 reflections. Improvement can be observed in the calculation of the 'lateral' part of the field but a deterioration in back and forward scattering. | 81 |
| 5.14 | RCS comparison ($\epsilon_r = 30$) considering 3 reflections. Improvement can be observed in the calculation of back and forward scattering but a deterioration in the 'lateral' part of the field. | 82 |
| 5.15 | RCS comparison ($\epsilon_r = 14$) considering 3 reflections. Improvement can be observed in the calculation of the 'lateral' part of the field but a deterioration in back and forward scattering. | 82 |
| B.1 | K-D Tree Sphere | 89 |
| B.2 | Octree Sphere | 89 |
| B.3 | K-D Tree 2 Spheres | 90 |
| B.4 | Octree 2 Spheres | 90 |
| B.5 | K-D Tree Spheres & Cylinder | 90 |
| B.6 | Octree Spheres & Cylinder | 90 |

| | | |
|-----|--|----|
| C.1 | Computational Time Performance (Sphere) | 91 |
| C.2 | Computational Time Performance (2 Sphere) | 92 |
| C.3 | Computational Time Performance (Sphere & Cylinder) | 92 |

Acronyms

GO

Geometrical Optics

RCS

Radar Cross Section

PEC

Perfect Electric Conductor

MoM

Method of Moments

PO

Physical Optics

LACE

Laboratorio Antenne e Compatibilità Elettromagnetica

RT

Ray Tracer

CFD

Complex Fluid Dynamics

ESA

European Space Agency

RF

Radio Frequency

GPS

Global Positioning System

FEM

Finite Element Modelling

FDTD

Finite Difference Time Domain

MECA

Modified Equivalent Current Approximation

Chapter 1

Introduction

Hypersonic flight regime is conventionally defined for $\text{Mach} > 5$; in these conditions, air ionization and heat shield ablation generate a plasma sheath around re-entering hypersonic vehicles.

This ionized plasma layer reflects and attenuates propagating electromagnetic waves to a point where total RF blackout can and does occur. RF blackout is of special concern for hypersonic vehicles because continuous contact with ground stations and GPS satellites is required for communication and navigation. The degree of plasma formation and signal attenuation varies considerably depending on many factors. Some factors that impact RF attenuation are re-entry velocity, vehicle design, heat shield impurity levels, and antenna placement.

Clearly a way to minimise or remove the disruption would provide a significant advantage for future experiments and missions, allowing the transmission of more data and a safer control of the vehicle during a delicate phase or the re-entry.

One possible solution to overcome this problem is to study the propagation of radio frequency waves within complex media such as the ionosphere, plasmas, and complex gas mixtures. Asymptotic techniques such as ray or beam tracing can be used to predict EM propagation in these inhomogeneous media where the radiation can be refracted, reflected and/or absorbed compared to free-space propagation.

A numerical code using these asymptotic techniques combined with integral equations for the free-space part of the simulation domain was developed at LINKS Foundation.

The problem was addressed with a hybrid approach to develop the numerical code. Equivalence Theorem to separate the inhomogeneous plasma region from the surrounding free space via an equivalent (Huygens) surface has been used, and the Eikonal approximation to Maxwell equations in the large inhomogeneous region for obtaining equivalent currents on the separating surface. Then, the scattered field via (exact) free space radiation of these surface equivalent currents has been obtained. The ray tracing method used effectively decompose the wavefront with

plane wave represented by one or more rays and follow the propagation using the Eikonal approximation valid for short wavelength. Contrary to ray tracing in homogeneous media, where the ray trajectories are straight lines, here a ray can be curved due to the continuous variation of the refractive index (inhomogeneity).

One of the limitations of this model and consequently of the numerical code is the fact that in order to have reliable results, a sufficiently dense grid of rays must be generated which interacts with objects in the "scene" while traversing it (ray traversal); this involves an enormous amount of computational time. The first part of this thesis work focused precisely on this problem: speeding up the ray traversal process; this was done by using special data structures such as K-D Trees or Octrees that can subdivide the physical space (the scene) into boxes and then through an appropriate traversal algorithm identify which boxes were hit by the ray in such a way as to follow its trajectory.

In the second part, on the contrary, improvements were made to the physical model, thus enabling the simulation of electromagnetic scattering situations not present in the original code, that were limited to the calculation of the Radar Cross Section considering only perfectly reflective and impenetrable surfaces (PEC); in particular the equations for boundary surfaces between different and possibly lossy dielectrics have been introduced, enabling the simulation of scattering with penetrable dielectrics bodies with sharp boundaries. Due to the secondary rays generated at the discontinuities the bookkeeping of rays is more complicated and has to be implemented efficiently.

Chapter 2 will describe from a purely theoretical point of view electromagnetic waves starting with Maxwell's equations and then moving on to the definition of plane waves to the problem of electromagnetic scattering and then to the definition and estimation of the Radar Cross Section (RCS).

Chapter 3 will describe in detail the numerical code used as a starting point for this research project; analyzing both the physical and numerical models used with their respective approximations.

Chapter 4 will describe in detail the methods used to speed up the Ray Traversal process; starting with the selection of the space division structure used and ending with the results of the numerical model and its advantages brought.

Finally, Chapter 5 will describe the improvements made on the physical model and physical situations that can be handled by the code with respective results.

Chapter 2

High Frequency Wave in Complex Media

2.1 Electromagnetic Wave

2.1.1 Maxwell's Equations

The state of excitation which is established in space by the presence of electric charges is said to constitute an electromagnetic field. It is represented by two vectors, E and B , called the electric vector and the magnetic induction respectively[1]. To describe the effect of the field on material objects, it is necessary to introduce a second set of vectors, the electric current density j , the electric displacement D , and the magnetic vector H . The space and time derivatives of the five vectors are related by the Macroscopic Maxwell's equations, which hold at every point in whose neighbourhood the physical properties of the medium are continuous:

$$\nabla \times H - \frac{1}{c} \dot{D} = \frac{4\pi}{c} j \quad (2.1)$$

$$\nabla \times E + \frac{1}{c} \dot{B} = 0 \quad (2.2)$$

the dot denoting differentiation with respect to time and c is the velocity of light in the vacuum that is approximately equal to $3 \times 10^{10} cm/s$.

They are supplemented by two scalar relations:

$$\nabla \cdot D = 4\pi\rho \quad (2.3)$$

$$\nabla \cdot B = 0 \quad (2.4)$$

The 2.3 may be regarded as a defining equation for the electric charge density ρ and 2.4 may be said to imply that no free magnetic poles exist.

2.1.2 Material Equations

The Maxwell's equations 2.1-2.4 connect the five basic quantities $\mathbf{E}, \mathbf{H}, \mathbf{B}, \mathbf{D}$ and \mathbf{j} . To allow a unique determination of the field vectors from a given distribution of currents and charges, these equations must be supplemented by relations which describe the behaviour of substances under the influence of the field. These relations are known as material equations or constitutive relations. In general they are rather complicated; but if the field is time-harmonic, and if the bodies are at rest, or in very slow motion relative to each other, and if the material is isotropic (i.e. when its physical properties at each point are independent of direction), they take usually the relatively simple form:

$$\mathbf{j} = \sigma\mathbf{E} \quad (2.5)$$

$$\mathbf{D} = \epsilon\mathbf{E} \quad (2.6)$$

$$\mathbf{B} = \mu\mathbf{H} \quad (2.7)$$

Here σ is called specific conductivity. ϵ is known as the dielectric constant (or permittivity) and μ is called the magnetic permeability. Eq. 2.5 is the differential form of Ohm's law. Substances for which $\sigma \neq 0$ (or more precisely is not negligibly small) are called conductors. Metals are very good conductors, but there are other classes of good conducting materials such as plasmas (ionised gas). In metals the conductivity decreases with increasing temperature. However, in other classes of materials, known as semiconductors (e.g. germanium), conductivity increases with temperature over a wide range. Substances for which σ is negligibly small are called insulator or dielectrics. Their electric and magnetic properties are then completely determined by ϵ and μ . For most substances the magnetic permeability μ is practically unity. If this is not the case, i.e. if μ differs appreciably from unity, we say that the substance is magnetic. Of particular interest for this thesis work are the so-called inhomogeneous or complex media, where the permittivity and permeability parameters have a dependence on position in space; they are therefore

in the form $\epsilon(r)$, $\mu(r)$. In particular, unitary permeability and a variable dielectric permittivity profile will be considered.

2.1.3 The wave equation and the velocity of light

Maxwell's equations relate the field vectors by means of simultaneous differential equations. On elimination is possible to obtain differential equations which each of the vectors must separately satisfy. Confining the attention to that part of the field which contains no charges or currents, i.e. where $j = 0$ and $\rho = 0$. First, by substituting for \mathbf{B} from the material equation 2.7 into the second Maxwell equation 2.2, dividing both sides by μ and applying the curl operator we have:

$$\nabla \times \left(\frac{1}{\mu} \nabla \times \mathbf{E} \right) + \frac{1}{c} \nabla \times \dot{H} = 0 \quad (2.8)$$

Next, by differentiating the first Maxwell equation 2.1 with respect to time, use the material equation 2.5 for \mathbf{D} , and eliminating $\nabla \times \dot{H}$ between the resulting equation and 2.8 it's possible to obtain:

$$\nabla \times \left(\frac{1}{\mu} \nabla \times \mathbf{E} \right) + \frac{\epsilon}{c^2} \ddot{E} = 0 \quad (2.9)$$

Using the identities $\nabla \times (u\mathbf{v}) = u\nabla \times (\mathbf{v}) + (\nabla u) \times \mathbf{v}$ and $\nabla \times (\nabla \times \mathbf{v}) = \nabla(\nabla \cdot \mathbf{v}) - \nabla^2$, 2.9 becomes:

$$\nabla^2 \mathbf{E} - \frac{\epsilon\mu}{c^2} \ddot{\mathbf{E}} + (\nabla \ln \mu) \times \nabla \times \mathbf{E} - \nabla(\nabla \cdot \mathbf{E}) = 0 \quad (2.10)$$

Also from 2.3, using again the material equation for \mathbf{D} and applying the identity $\nabla \cdot u\mathbf{v} = u\nabla \cdot \mathbf{v} + \mathbf{v} \cdot \nabla u$ we find:

$$\epsilon \nabla \cdot \mathbf{E} + \mathbf{E} \cdot \nabla \epsilon = 0 \quad (2.11)$$

Hence 2.10 may be written in the form:

$$\nabla^2 \mathbf{E} - \frac{\epsilon\mu}{c^2} \ddot{\mathbf{E}} + (\nabla \ln \mu) \times \nabla \times \mathbf{E} + \nabla(\mathbf{E} \cdot \nabla \ln \epsilon) = 0 \quad (2.12)$$

In a similar way it's possible to obtain an equation for \mathbf{H} alone:

$$\nabla^2 \mathbf{H} - \frac{\epsilon\mu}{c^2} \ddot{\mathbf{H}} + (\nabla \ln \epsilon) \times \nabla \times \mathbf{H} + \nabla(\mathbf{H} \cdot \nabla \ln \mu) = 0 \quad (2.13)$$

In particular, if the medium is homogeneous, $\nabla \ln \epsilon = \nabla \ln \mu = 0$, and 2.12 and 2.13 reduce to:

$$\nabla^2 \mathbf{E} - \frac{\epsilon\mu}{c^2} \ddot{\mathbf{E}} = 0; \nabla^2 \mathbf{H} - \frac{\epsilon\mu}{c^2} \ddot{\mathbf{H}} = 0 \quad (2.14)$$

2.1.4 Plane Wave

In a homogeneous medium in regions free of current and charges, each rectangular component $V(\mathbf{r}, t)$ of the field vectors satisfies, according to 2.14, the homogeneous wave equation

$$\nabla^2 \mathbf{V} - \frac{1}{v^2} \ddot{\mathbf{V}} = 0; \quad (2.15)$$

where the double dot represent the double differentiation with respect to time. The simplest solution of this equation is called *plane wave* and it will be examined in the following.

Let $\mathbf{r}(x, y, z)$ be a position of a point P in space and $\mathbf{s}(s_x, s_y, s_z)$ a unit vector in a fixed direction. Any solution of 2.15 of the form

$$V = V(\mathbf{r} \cdot \mathbf{s}, t) \quad (2.16)$$

is said to represent a *plane wave*, since at each instant of time V is constant over each of the planes

$$\mathbf{r} \cdot \mathbf{s} = \text{constant} \quad (2.17)$$

which are perpendicular to the unit vector \mathbf{s} .

It will be convenient to choose a new set of Cartesian axes $O\xi, O\eta, O\zeta$ with $O\zeta$ in the direction of s . Then

$$\mathbf{r} \cdot \mathbf{s} = \zeta \quad (2.18)$$

and one has

$$\frac{\partial}{\partial x} = s_x \frac{\partial}{\partial \zeta}; \quad \frac{\partial}{\partial y} = s_y \frac{\partial}{\partial \zeta}; \quad \frac{\partial}{\partial z} = s_z \frac{\partial}{\partial \zeta}; \quad (2.19)$$

From these relations one easily finds that

$$\nabla^2 \mathbf{V} = \frac{\partial^2 V}{\partial \zeta^2} \quad (2.20)$$

so that 2.15 becomes

$$\frac{\partial^2 V}{\partial \zeta^2} - \frac{1}{v^2} \frac{\partial^2 V}{\partial t^2} = 0; \quad (2.21)$$

If one set:

$$\zeta - vt = p; \quad \zeta + vt = q; \quad (2.22)$$

2.21 takes the form

$$\frac{\partial^2 V}{\partial p \partial q} = 0; \quad (2.23)$$

The general solution of this equation is

$$V = V_1(p) + V_2(q) = V_1(\mathbf{r} \cdot \mathbf{s} - vt) + V_2(\mathbf{r} \cdot \mathbf{s} + vt) \quad (2.24)$$

where V_1 and V_2 are arbitrary functions. It's possible to see that the argument of V_1 is unchanged when (ζ, t) is replaced by $(\zeta + v\tau, t + \tau)$, where τ is arbitrary. Hence V_1 represents a disturbance which is propagated with velocity v in the positive ζ direction. Similarly $V_2(\zeta + vt)$ represents a disturbance which is propagated with velocity v in the negative ζ direction.

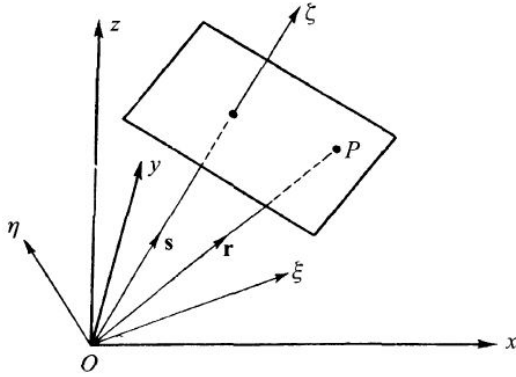


Figure 2.1: Plane wave propagation

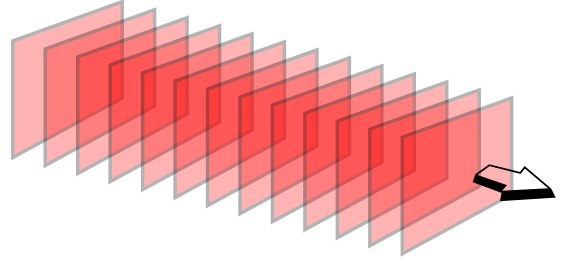


Figure 2.2: Wave fronts

2.1.5 Time-Harmonic Waves

At a point r_0 in space the wave disturbance is a function of time only:

$$V(r_0, t) = F(t) \quad (2.25)$$

The case when F is periodic is of particular interest. Accordingly one consider the case when F has the form

$$F(t) = a \cos(\omega t + \delta) \quad (2.26)$$

Here $a(> 0)$ is called the *amplitude*, and the argument $\omega t + \delta$ of the cosine term is called *phase*. The quantity

$$v = \frac{\omega}{2\pi} = \frac{1}{T} \quad (2.27)$$

is called the *frequency* and represents the number of vibrations per second, ω is called the *angular frequency* and gives the number of vibrations in 2π seconds. Since F remains unchanged when t is replaced by $t+T$, T is called *period* of the vibrations. Wave functions (i.e. solution of the wave equations) of the form 2.26 are said to be *time harmonic* with respect to time.

Let's first consider a wave function which represent a *harmonic plane wave* propagated in the direction specified by a unit vector \mathbf{s} . According to the definition of the plane wave given in the previous section, it is obtained on replacing t by $t - \mathbf{r} \cdot \mathbf{s}/v$ in 2.26:

$$V(\mathbf{r}, t) = a \cos \left[\omega \left(t - \frac{\mathbf{r} \cdot \mathbf{s}}{v} \right) + \delta \right] \quad (2.28)$$

Eq. 2.28 remains unchanged when $\mathbf{r} \cdot \mathbf{s}$ is replaced by $\mathbf{r} \cdot \mathbf{s} + \lambda$, where:

$$\lambda = v \frac{2\pi}{\omega} = vT \quad (2.29)$$

The length λ is called the *wavelength*. It is also useful to define a *vacuum wavelength* λ_0 as

$$\lambda_0 = cT = n\lambda \quad (2.30)$$

this is the wavelength which corresponds to a harmonic wave of the same frequency propagated in *vacuo*.

It is also convenient to define vectors \mathbf{k}_0 and \mathbf{k} in the direction \mathbf{s} of propagation, whose lengths are respectively

$$k_0 = 2\pi k = \frac{2\pi}{\lambda_0} = \frac{\omega}{c} \quad (2.31)$$

and

$$k = nk_0 = \frac{2\pi}{\lambda} = \frac{n\omega}{c} = \frac{\omega}{v} \quad (2.32)$$

The vector $\mathbf{k} = k\mathbf{s}$ is called the *wave vector* or the *propagation vector* in the medium, $\mathbf{k}_0 = k_0\mathbf{s}$ being the corresponding vector in the vacuum.

In order to make more understandable the derivation of the Eikonal equation for the geometric optics approximation and the curvilinear trajectories of rays within a complex medium that will be described in later sections, it is appropriate to consider a time-harmonic wave of a more complicated form. A general time-harmonic, real, scalar wave of frequency ω may be defined as a real solution of the wave equation, of the form

$$V(\mathbf{r}, t) = a(\mathbf{r}) \cos[\omega t - g(\mathbf{r})] \quad (2.33)$$

$a(> 0)$ and g being real scalar functions of positions. The surfaces

$$g(\mathbf{r}) = \text{constant} \quad (2.34)$$

are called *cophasal surfaces* or *wave surfaces*. In contrast with the previous case, the surface of constant amplitude of the wave do not, in general, coincide with the surfaces of constant phase. Such a wave is said to be *inhomogeneous*. Calculations with harmonic waves are simplified by the use of exponential instead of trigonometric functions. Eq. 2.33 may be written as:

$$V(\mathbf{r}, t) = \text{Re}[U(\mathbf{r})e^{-i\omega t}] \quad (2.35)$$

where

$$U(\mathbf{r}) = a(\mathbf{r})e^{ig(\mathbf{r})} \quad (2.36)$$

On substitution from 2.36 into the wave equation 2.15, one finds that U must satisfy the equation

$$\nabla^2 U + n^2 k_0^2 U = 0 \quad (2.37)$$

U is called *complex amplitude* of the wave. In particular, for a plane wave one has

$$g(\mathbf{r}) = \omega \left(\frac{\mathbf{r} \cdot \mathbf{s}}{v} \right) - \delta = k(\mathbf{r} \cdot \mathbf{s}) - \delta = \mathbf{k} \cdot \mathbf{s} - \delta \quad (2.38)$$

2.1.6 The laws of refraction and reflection

Starting from 2.79 it follows, on account of the identity $\nabla \times (\nabla f) = 0$, that the vector $n\mathbf{s} = n\mathbf{dr}/ds$, called sometimes the ray vector, satisfies the relation

$$\nabla \times (n\mathbf{s}) = 0 \quad (2.39)$$

Considering a discontinuity surface T and replacing it by a transition layer throughout which ϵ, μ and n change rapidly but continuously from their values near T on one side to their values near T on the other. Next one takes a plane element of area with its sides P_1Q_1 and P_2Q_2 parallel and with P_1P_2 and Q_1Q_2 perpendicular to T (see fig.2.5). If \mathbf{b} denotes the unit normal to this area, then we have from ??, on integrating throughout the area and applying Stoke's theorem:

$$\int (\nabla \times n\mathbf{s}) \cdot \mathbf{b} dS = \int n\mathbf{s} \cdot d\mathbf{r} = 0 \quad (2.40)$$

the second integral being taken along the boundary curve $P_1Q_1Q_2P_2$. Proceeding to the limit as the height $\delta h \rightarrow 0$, in a strictly similar manner as the derivation of the continuity of the tangential components, one obtains:

$$\mathbf{n}_{12} \times (n_2\mathbf{s}_2 - n_1\mathbf{s}_1) = 0 \quad (2.41)$$

where \mathbf{n}_{12} is the unit normal to the boundary surface pointing from the first into the second medium. Eq.2.41 implies that the tangential component of the ray vector $n\mathbf{s}$ is continuous across the surface or, what amounts to the same thing, the vector \mathbf{N}_{12} is normal to the surface.

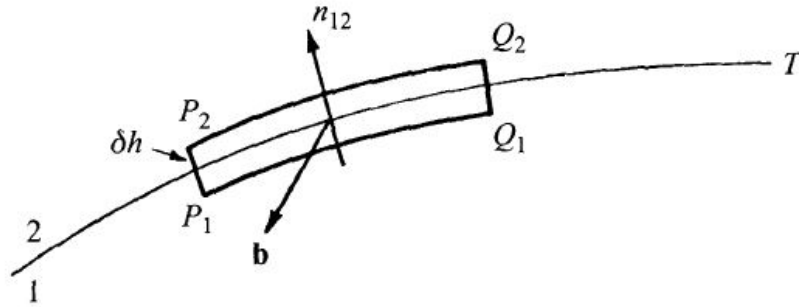


Figure 2.3: Illustration of the laws of reflection and refraction

Let θ_1 and θ_2 be the angles which the incident ray and the refracted ray make with the normal \mathbf{n}_{12} to the surface. Then it follows from 2.41 that:

$$n_2(\mathbf{n}_{12} \times \mathbf{s}_2) = n_1(\mathbf{n}_{12} \times \mathbf{s}_1) \quad (2.42)$$

so that

$$n_2 \sin \theta_2 = n_1 \sin \theta_1 \quad (2.43)$$

Eq. 2.42 implies that the refracted ray lies in the same plane as the incident ray and the normal to the surface (the plane of incidence) and 2.43 shows that the ratio of the sine of the angle of refraction to the sine of the angle of incidence is equal to the ratio n_1/n_2 of the refractive indices. These two results express the *law of refraction (Snell's law)*. One must expect that there will be another wave, the reflected wave, propagated back into the first medium. Setting $n_1 = n_2$ in 2.42 and 2.43 it follows that the reflected ray lies in the plane of incidence and that $\sin \theta_2 = \sin \theta_1$; hence

$$\theta_2 = \pi - \theta_1 \quad (2.44)$$

The last results express the *law of reflection*.

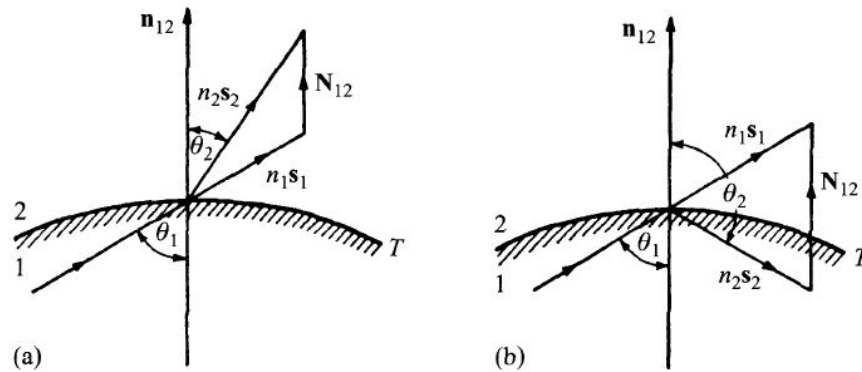


Figure 2.4: Illustration of the laws of refraction(a) and reflection(b)

2.1.7 Fresnel formulae

This section will describe how the amplitude of the field varies when applying the laws of reflection and refraction in the case where the incident field is represented by a plane time-harmonic wave. Recalling the definition of a plane time-harmonic wave (2.28) let A be the amplitude of the electric vector of the incident field. One takes A to be complex, with its phase equal to the constant part of the argument of the wave function; the variable part is

$$\tau_i = \omega \left(t - \frac{\mathbf{r} \cdot \mathbf{s}^{(i)}}{v_1} \right) = \omega \left(t - \frac{x \sin \theta_i + z \sin \theta_i}{v_1} \right) \quad (2.45)$$

In the following each vector will be resolved into components parallel (denoted by subscript \parallel) and perpendicular (subscript \perp) to the plane of incidence. The choice of the positive directions for parallel components is indicated in the figure below. The perpendicular components must be visualized at right angles to the plane of the figure.

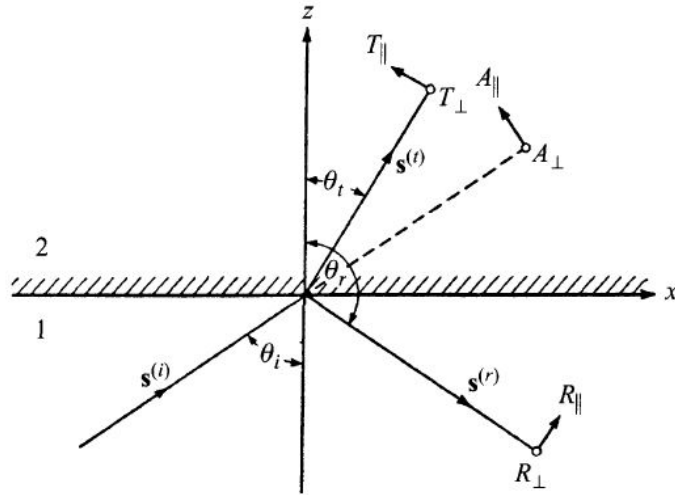


Figure 2.5: Refraction and reflection of a plane wave. Plane of incidence

The components of the electric vector of the incident field then are:

$$E_x^{(i)} = -A_{\parallel} \cos \theta_i e^{-i\tau_i}; \quad E_y^{(i)} = A_{\perp} e^{-i\tau_i}; \quad E_z^{(i)} = A_{\parallel} \sin \theta_i e^{-i\tau_i}; \quad (2.46)$$

The components of the magnetic vector are immediately obtained by using the following equality for a plane wave considering $\mu = 1$:

$$\mathbf{H} = \sqrt{\epsilon} \mathbf{s} \times \mathbf{E} \quad (2.47)$$

This gives:

$$H_x^{(i)} = -A_{\perp} \cos \theta_i \sqrt{\epsilon_1} e^{-i\tau_i}; \quad H_y^{(i)} = -A_{\parallel} \sqrt{\epsilon_1} e^{-i\tau_i}; \quad H_z^{(i)} = A_{\perp} \sin \theta_i \sqrt{\epsilon_1} e^{-i\tau_i}; \quad (2.48)$$

Similarly if T and R are the complex amplitudes of the transmitted and reflected waves, the corresponding components of the electric and magnetic vectors are:

TransmittedField :

$$E_x^{(t)} = -T_{\parallel} \cos \theta_t e^{-i\tau_t}; \quad E_y^{(t)} = T_{\perp} e^{-i\tau_t}; \quad E_z^{(t)} = T_{\parallel} \sin \theta_t e^{-i\tau_t};$$

$$H_x^{(t)} = -T_{\perp} \cos \theta_t \sqrt{\epsilon_2} e^{-i\tau_t}; \quad H_y^{(t)} = -T_{\parallel} \sqrt{\epsilon_2} e^{-i\tau_t}; \quad H_z^{(t)} = T_{\perp} \sin \theta_t \sqrt{\epsilon_2} e^{-i\tau_t}; \quad (2.49)$$

with

$$\tau_t = \omega \left(t - \frac{\mathbf{r} \cdot \mathbf{s}^{(t)}}{v_2} \right) = \omega \left(t - \frac{x \sin \theta_t + z \sin \theta_t}{v_2} \right) \quad (2.50)$$

ReflectedField :

$$E_x^{(r)} = -R_{\parallel} \cos \theta_r e^{-i\tau_r}; \quad E_y^{(r)} = R_{\perp} e^{-i\tau_r}; \quad E_z^{(r)} = R_{\parallel} \sin \theta_r e^{-i\tau_r};$$

$$H_x^{(r)} = -R_{\perp} \cos \theta_r \sqrt{\epsilon_1} e^{-i\tau_r}; \quad H_y^{(r)} = -R_{\parallel} \sqrt{\epsilon_1} e^{-i\tau_r}; \quad H_z^{(r)} = R_{\perp} \sin \theta_r \sqrt{\epsilon_1} e^{-i\tau_r}; \quad (2.51)$$

with

$$\tau_r = \omega \left(t - \frac{\mathbf{r} \cdot \mathbf{s}^{(r)}}{v_1} \right) = \omega \left(t - \frac{x \sin \theta_r + z \sin \theta_r}{v_1} \right) \quad (2.52)$$

Imposing the boundary conditions that the tangential components of \mathbf{E} and \mathbf{H} should be continuous at the interface between two media it follows that:

$$\begin{aligned} E_x^{(i)} + E_x^{(r)} &= E_x^{(t)} \\ E_y^{(i)} + E_y^{(r)} &= E_y^{(t)} \\ H_x^{(i)} + H_x^{(r)} &= H_x^{(t)} \\ H_y^{(i)} + H_y^{(r)} &= H_y^{(t)} \end{aligned} \quad (2.53)$$

On substituting into 2.53 for all the components the relations for \mathbf{D} and \mathbf{B} and using the fact that $\cos \theta_r = \cos(\pi - \theta_i) = -\cos \theta_i$, one obtains the four relations:

$$\begin{aligned}
 \cos \theta_i (A_{\parallel} - R_{\parallel}) &= \cos \theta_t T_{\parallel} \\
 A_{\perp} + R_{\perp} &= T_{\perp} \\
 \sqrt{\epsilon_1} \cos \theta_i (A_{\perp} - R_{\perp}) &= \sqrt{\epsilon_2} \cos \theta_t T_{\perp} \\
 \sqrt{\epsilon_1} (A_{\parallel} + R_{\parallel}) &= \sqrt{\epsilon_2} T_{\parallel}
 \end{aligned} \tag{2.54}$$

It is possible to note that the equations 2.54 fall into two groups, one which contains only the components parallel to the plane of incidence, whilst the other contains only those which are perpendicular to the plane of incidence. These two kinds of waves are, therefore, independent of one another. Solving 2.54 for the components of the reflected and transmitted waves in terms of those of the incident wave and using the Maxwell's relation $n = \sqrt{\epsilon}$ one gets the so called *Fresnel formulae*:

$$\begin{aligned}
 T_{\parallel} &= \frac{2n_1 \cos \theta_i}{n_2 \cos \theta_i + n_1 \cos \theta_t} A_{\parallel} \\
 T_{\perp} &= \frac{2n_1 \cos \theta_i}{n_2 \cos \theta_i + n_1 \cos \theta_t} A_{\perp} \\
 R_{\parallel} &= \frac{n_2 \cos \theta_i - n_1 \cos \theta_t}{n_2 \cos \theta_i + n_1 \cos \theta_t} A_{\parallel} \\
 R_{\perp} &= \frac{n_2 \cos \theta_i - n_1 \cos \theta_t}{n_2 \cos \theta_i + n_1 \cos \theta_t} A_{\perp}
 \end{aligned} \tag{2.55}$$

In the following, test results refer to lossy media; to understand how reflection and transmission coefficients and their respective angles vary when lossy media are considered refer to Appendix F.

2.2 Complex Media

A complex medium will be understood in this discussion to mean a **dispersive, potentially dissipative** and **non-homogeneous** medium.

In physics, the term dispersion denotes the phenomenon in which a wave, during its propagation, undergoes an elongation in space of its waveform or wavefront or wave envelope due to the dependence of the refractive index and the permittivity ϵ of the medium itself on frequency. As a further consequential effect there is contraction of the frequency spectrum of the perturbation and scattering in space of the energy associated with the envelope itself with global conservation of total energy.

The speed of propagation of a wave thus depends on its wavelength.

The relationship between pulsation and wave number is no longer constant, that is, the dependence between pulsation and wave number is no longer expressed through a simple linear law. In the case of propagation in dispersive media, it will be necessary to express ω as a generic function of k , $\omega(k)$. The relation that links the pulsation to the wave number takes the name of dispersion relation. The explicit form of the dispersion relation will depend on the particular case under consideration.

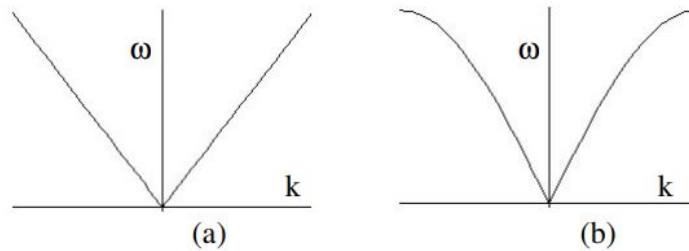


Figure 2.6: Two different dispersion curves: a) non-dispersive medium, b) dispersive medium

In the case where there is propagation of a wave packet in a dispersive medium, the different Fourier components of the packet will have different phase velocities. Under these conditions the faster components of the packet will overpower the slower ones and the packet will expand by deforming during the motion. Thus in the case of a perturbation moving in a dispersive medium the phase velocity will no longer represent the velocity of the perturbation. In this case a new quantity, called the group velocity v_g , which measures the velocity of the wave packet maximum. One it can be shown that, for wave packets whose Fourier transform is sufficiently narrow around an average value k_0 of the wave vector, the group velocity is equal to the derivative of the pulsation with respect to the wave vector calculated for k_0 :

$$v_g = \frac{d\omega}{dk} \quad (2.56)$$

Taking into consideration the propagation of white light in a dispersive medium. The colors of the components correspond to the wavelengths. As with true visible light to red corresponds the maximum wavelength, to violet the minimum.

In a well-known experiment Newton demonstrated that sunlight is actually a mixture of light of various colors. He, through a prism, exploiting the phenomenon of refraction was able to break down a beam of sunlight into its component colors.

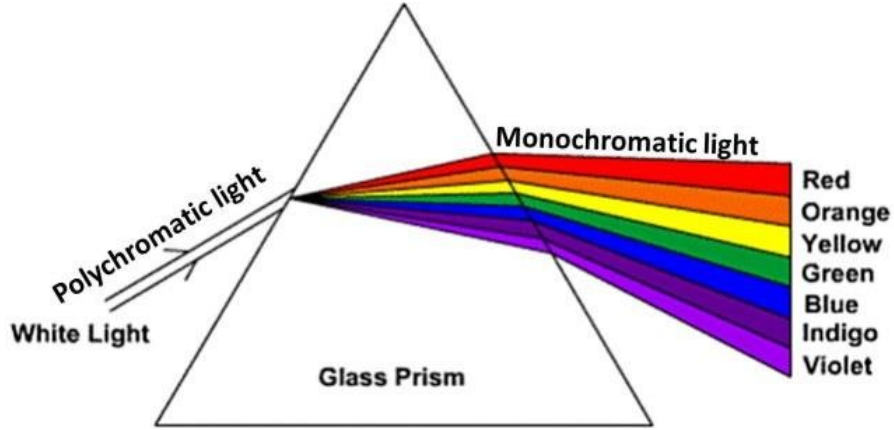


Figure 2.7: Diagram of dispersion in Newton's prism

Regarding the property of non-homogeneity, it means the lack of spatial symmetry of the microscopic structure of the medium.

An example of such a propagation medium that will be discussed in detail below is the hypersonic plasma, whose dielectric permittivity is given by the following relationship:

$$\epsilon_r(\mathbf{r}) = 1 - \frac{\omega_{pe}^2(\mathbf{r})}{\omega(\omega - i\nu_c(\mathbf{r}))} \quad (2.57)$$

where $\omega_{pe}^2 = n_e e^2 / (\epsilon_0 m_e)$ is the electron plasma frequency (squared), n_e the electron density, m_e the electron mass, ϵ_0 the vacuum permittivity and ν_c is the neutral-plasma collision frequency.

2.3 Geometrical Optics and Ray Theory

2.3.1 Approximation for very short wavelengths

The electromagnetic field associated with the propagation of visible light is characterized by very rapidly oscillations or, what amount to the same thing, by the smallness of the wavelength. It may therefore be expected that a good first approximation to the propagation laws in such cases may be obtained by a complete neglect of the fitness of the wavelength; this approximation can be made also for object that are electrically large with respect to the operating frequency; this is the case in analysis of this thesis work. The branch of optics which is characterized by the neglect of the wavelength is known as *geometrical optics*, since in this approximation the optical laws may be formulated in the language of geometry. The energy may then be regarded as being transported along certain curves (*light rays*).

2.3.2 Eikonal equation for GO

In the following, the fundamental equations of geometric optics will be derived from the equation 2.37 described in 2.1.5 and in the case of complex (inhomogeneous) time-invariant media in which the refractive index n is a function of the position $n(\mathbf{r}) = n(x, y, z)$. Moreover, if the electromagnetic wave is monochromatic, i.e. a pure harmonic expressible as $U(x, y, z)e^{-i\omega t}$, with pulsation ω , we can solve the equation 2.37 by applying the method of separation in the spatial (x,y,z) and temporal variables t:

$$\frac{\partial U(x, y, z)}{\partial x^2} + \frac{\partial U(x, y, z)}{\partial y^2} + \frac{\partial U(x, y, z)}{\partial z^2} + k_0^2 n^2(x, y, z)U(x, y, z) = 0 \quad (2.58)$$

By expressing $U(x, y, z)$ as 2.36 and differentiating with respect to x one obtain:

$$\frac{\partial U}{\partial x} = \frac{\partial A}{\partial x} e^{ik_0 S} + A e^{ik_0 S} i k_0 \frac{\partial S}{\partial x} = \left[\frac{\partial A}{\partial x} + i k_0 A \frac{\partial S}{\partial x} \right] e^{ik_0 S} \quad (2.59)$$

where for brevity we have omitted the explicit dependence of S and A on (x,y,z). Differentiating again with respect to x gives:

$$\begin{aligned}
 \frac{\partial^2 U}{\partial x^2} &= \left[\frac{\partial^2 A}{\partial x^2} + ik_0 \left(\frac{\partial A}{\partial x} \frac{\partial S}{\partial x} + A \frac{\partial^2 S}{\partial x^2} \right) \right] e^{ik_0 S} + \left[\frac{\partial A}{\partial x} + ik_0 A \frac{\partial S}{\partial x} \right] e^{ik_0 S} ik_0 \frac{\partial S}{\partial x} = \\
 & \left[\frac{\partial^2 A}{\partial x^2} + ik_0 \left(\frac{\partial A}{\partial x} \frac{\partial S}{\partial x} + A \frac{\partial^2 S}{\partial x^2} \right) + ik_0 \frac{\partial S}{\partial x} \left(\frac{\partial A}{\partial x} + ik_0 A \frac{\partial S}{\partial x} \right) \right] e^{ik_0 S} = \\
 & \left[\frac{\partial^2 A}{\partial x^2} + 2ik_0 \frac{\partial A}{\partial x} \frac{\partial S}{\partial x} + ik_0 A \frac{\partial^2 S}{\partial x^2} - k_0^2 A \left(\frac{\partial S}{\partial x} \right)^2 \right] e^{ik_0 S}
 \end{aligned} \tag{2.60}$$

By differentiating $U(x, y, z)$ with respect to y and z as well, we obtain expressions quite similar to the previous one, only with the variables y and z instead of x . Below are the various differentiations for calculating the scalar Laplacian:

$$\begin{aligned}
 \nabla^2 U &= \frac{\partial^2 U}{\partial x^2} + \frac{\partial^2 U}{\partial y^2} + \frac{\partial^2 U}{\partial z^2} = \\
 & \left[\frac{\partial^2 A}{\partial x^2} + 2ik_0 \frac{\partial A}{\partial x} \frac{\partial S}{\partial x} + ik_0 A \frac{\partial^2 S}{\partial x^2} - k_0^2 A \left(\frac{\partial S}{\partial x} \right)^2 \right] e^{ik_0 S} + \\
 & \left[\frac{\partial^2 A}{\partial y^2} + 2ik_0 \frac{\partial A}{\partial y} \frac{\partial S}{\partial y} + ik_0 A \frac{\partial^2 S}{\partial y^2} - k_0^2 A \left(\frac{\partial S}{\partial y} \right)^2 \right] e^{ik_0 S} + \\
 & \left[\frac{\partial^2 A}{\partial z^2} + 2ik_0 \frac{\partial A}{\partial z} \frac{\partial S}{\partial z} + ik_0 A \frac{\partial^2 S}{\partial z^2} - k_0^2 A \left(\frac{\partial S}{\partial z} \right)^2 \right] e^{ik_0 S} = \\
 & \left[\nabla^2 A + 2ik_0 \nabla A \nabla S + ik_0 A \nabla^2 S - k_0^2 A |\nabla S|^2 \right] e^{ik_0 S}
 \end{aligned} \tag{2.61}$$

By substituting the equations 2.61 and 2.37 inside 2.36, since the exponential term $e^{ik_0 S}$ cannot be equal to zero, it is deduced:

$$\begin{aligned}
 \nabla^2 A + 2ik_0 \nabla A \nabla S + ik_0 A \nabla^2 S - k_0^2 A |\nabla S|^2 + k_0^2 n^2 A &= \\
 \nabla^2 A + k_0^2 A (n^2 - |\nabla S|^2) + ik_0 (A \nabla^2 S + 2 \nabla A \nabla S) &= 0
 \end{aligned} \tag{2.62}$$

By separating the real part and the imaginary part, we get the equations:

$$\nabla^2 A + k_0^2 A (n^2 - |\nabla S|^2) = 0 \tag{2.63}$$

$$k_0 (A \nabla^2 S + 2 \nabla A \nabla S) = 0 \tag{2.64}$$

At this point one can introduce the approximation that leads to geometric optics; it consists in admitting that in the 2.63 the term $\nabla^2 A$ is negligible compared to the other two:

$$\nabla^2 A \ll k_0^2 A (n^2 - |\nabla S|^2) \tag{2.65}$$

Since the latter are multiplied by k_0^2 and therefore have a weight that grows as ω^2 that is $1/\lambda^2$, we use to say that geometric optics is the limit of ondulatory optics in the hypothesis of relatively high frequencies $\omega \rightarrow \infty$ (or low wavelengths $\lambda \rightarrow 0$) that is the assumption described in the previous section.

Introducing the approximation 2.65 in 2.63, since we exclude the trivial solution in which the amplitude A is equal to zero, we obtain the equation:

$$\nabla S \cdot \nabla S = |\nabla S|^2 = n^2 \quad (2.66)$$

where as before $n = \sqrt{\epsilon\mu}$ is the refractive index. The function S is often called the *Eikonal* and 2.66 is known as the *Eikonal equation*; it is the basic equation of geometrical optics and it describes the spatial variation of the phase and relates it to the refractive index. The surfaces

$$S(\mathbf{r}) = \text{constant} \quad (2.67)$$

may be called *geometrical wave surfaces* or the *geometrical wave-fronts*.

2.3.3 The light rays and the intensity law of geometrical optics

Starting from the *Eikonal equation* derived in the previous section one has:

$$\mathbf{s} = \frac{\nabla S}{n} = \frac{\nabla S}{|\nabla S|} \quad (2.68)$$

and is possible to demonstrate that s is in the direction of the average Poynting vector. Hence the average Poynting vector is in the direction of the normal to the geometrical wave-front. The *geometrical light rays* may be now defined as the orthogonal trajectories to the geometrical wave fronts $S = \text{constant}$. One shall regard them as oriented curves whose direction coincides everywhere with the direction of the average Poynting vector. If $r(s)$ denotes the position vector of a point P on a ray, considered as a function of the length of arc s of the ray, then $d\mathbf{r}/ds = \mathbf{s}$, and the equation of the ray may be written as

$$n \frac{d\mathbf{r}}{ds} = \nabla S \quad (2.69)$$

and it can be demonstrated that at every point the electric and magnetic vectors are orthogonal to the ray. Considering now two neighbouring wave-fronts $S = \text{constant}$ and $S + dS = \text{constant}$ (2.8). Then:

$$\frac{dS}{ds} = \frac{d\mathbf{r}}{ds} \cdot \nabla S = \mathbf{n} \quad (2.70)$$

Hence the distance ds between points on the opposite ends of a normal cutting the two wave-fronts is inversely proportional to the refractive index.

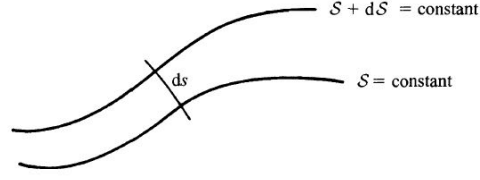


Figure 2.8: Illustrating the meaning of the relation $ns = \nabla S$

The integral $\int_C n ds$ taken along a curve C is known as the *optical length* of the curve. Denoting by square brackets the optical length of the ray which joins point P_1 and P_2 , one has

$$[P_1 P_2] = \int_{P_1}^{P_2} n ds = S(P_2) - S(P_1) \quad (2.71)$$

Since the average energy density is propagated with the velocity $v = c/n$ along the ray

$$n ds = \frac{c}{v} ds = c dt \quad (2.72)$$

where dt is the time needed for the energy to travel the distance ds along the ray; hence

$$[P_1 P_2] = c \int_{P_1}^{P_2} dt \quad (2.73)$$

so the optical length $[P_1 P_2]$ is equal to the product of the vacuum velocity of light and the time needed for light to travel from P_1 to P_2 . The intensity of light I is defined as the absolute value of the time average of the Poynting vector:

$$I = |\mathbf{S}| \quad (2.74)$$

and the conservation law gives

$$\nabla \cdot (I \mathbf{s}) = 0 \quad (2.75)$$

To see the implications of this relation is possible to take a narrow tube formed by all the rays proceeding from an element dS_1 of a wave front $S(\mathbf{r} = a_1$ with a_1 constant, and denoting by dS_2 the corresponding element in which these rays intersect another wave-front $S(\mathbf{r} = a_2$. Integrating 2.75 throughout the tube and applying Gauss'theorem one obtain:

$$\int I \mathbf{s} \cdot \mathbf{v} dS = 0 \quad (2.76)$$

\mathbf{v} denoting the outward normal to the tube. Now

$$\begin{aligned} \mathbf{s} \cdot \mathbf{v} &= 1 \text{ on } dS_2 \\ &= -1 \text{ on } dS_1 \\ &= 0 \text{ elsewhere} \end{aligned} \quad (2.77)$$

so that 2.76 reduces to:

$$I_1 dS_1 = I_2 dS_2 \quad (2.78)$$

I_1 and I_2 denotes the intensity on dS_1 and on dS_2 respectively. Hence $I dS$ remains constant along a tube of rays. This result expresses the *intensity law of geometrical optics*.

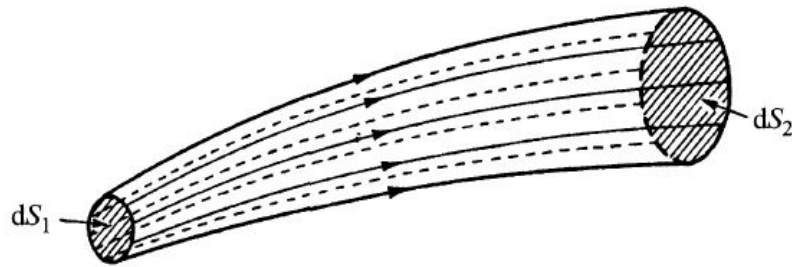


Figure 2.9: Illustrating the intensity law

2.3.4 The differential equation of light rays

The light rays have been defined as the orthogonal trajectories to the geometrical wavefronts $S(x,y,z)=\text{constant}$ and if \mathbf{r} is a position vector of a typical point on a ray and s the length of the ray measured from a fixed point on it, then

$$n \frac{d\mathbf{r}}{ds} = \nabla S \quad (2.79)$$

This equation specifies the rays by means of the function S , but one can easily derive from it a differential equation which specifies the rays directly in terms of the refractive index function $n(\mathbf{r})$ which is the case of interest of this thesis work since dealing with complex media.

Differentiating 2.79 with respect to s one obtain:

$$\begin{aligned} \frac{d}{ds} \left(n \frac{d\mathbf{r}}{ds} \right) &= \frac{d}{ds} (\nabla S) \\ &= \frac{d\mathbf{r}}{ds} \cdot \nabla (\nabla S) \\ &= \frac{1}{n} \nabla S \cdot \nabla (\nabla S) \\ &= \frac{1}{2n} \nabla [(\nabla S)^2] \\ &= \frac{1}{2n} \nabla n^2 \end{aligned} \quad (2.80)$$

i.e

$$\frac{d}{ds} \left(n \frac{d\mathbf{r}}{ds} \right) = \nabla n \quad (2.81)$$

This is the vector form of the differential equations of the light rays. In particular, in a *homogeneous* medium $n=\text{constant}$ and 2.81 reduces to:

$$\frac{d^2 \mathbf{r}}{ds^2} = 0 \quad (2.82)$$

whence

$$\mathbf{r} = s\mathbf{a} + \mathbf{b} \quad (2.83)$$

\mathbf{a} and \mathbf{b} being constant vectors. Eq. 2.83 is a vector equation of a straight line in the direction of the vector \mathbf{a} , passing through the point $\mathbf{r} = \mathbf{b}$. Hence in a homogeneous medium the light rays have the form of a straight lines.

Let's now consider rays in a complex medium which has a spherical symmetry, i.e. the refractive index depends only on the distance r from a fixed point O :

$$n = n(r) \tag{2.84}$$

This case is approximately realized by the earth's atmosphere, when the curvature of the earth is taken into account of in situation of ionized gas in general.

Consider the variation of the vector $\mathbf{r} \times [n(r)\mathbf{s}]$ along the ray. One has:

$$\frac{d}{ds}(\mathbf{r} \times n\mathbf{s}) = \frac{d\mathbf{r}}{ds} \times n\mathbf{s} + \mathbf{r} \times \frac{d}{ds}(n\mathbf{s}) \tag{2.85}$$

Since $d\mathbf{r}/ds = \mathbf{s}$, the first term on the right vanished. The second term may, on account of 2.81 be written as $\mathbf{r} \times \nabla n$. Now from 2.84:

$$\nabla n = \frac{\mathbf{r}}{r} \frac{dn}{dr} \tag{2.86}$$

so that the second term on the right-hand side of 2.85 also vanished. Hence

$$\mathbf{r}\mathbf{s} = \text{constant} \tag{2.87}$$

This relation implies that all the rays are plane curves, situated in a plane through the origin, and that along each ray

$$nr \sin \phi = \text{constant} \tag{2.88}$$

where ϕ is the angle between the position vector \mathbf{r} and the tangent at the point \mathbf{r} on the ray (see 2.10).

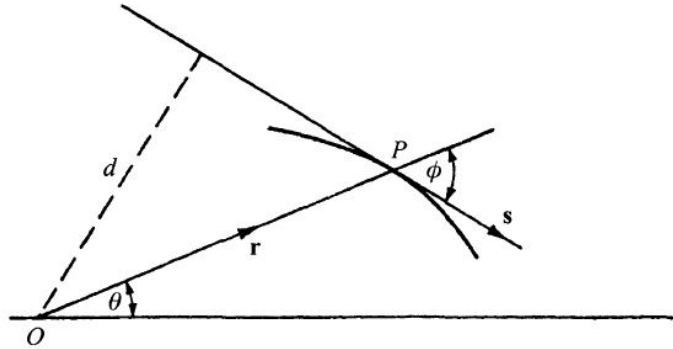


Figure 2.10: Illustrating the 'curved' ray

Returning to the general case and considering the *curvature vector* of a ray, i.e. the vector

$$\mathbf{K} = \frac{d\mathbf{s}}{ds} = \frac{1}{\rho}\mathbf{v} \quad (2.89)$$

whose magnitude $1/\rho$ is the reciprocal of the radius of curvature; \mathbf{v} is the unit principal normal at a typical point of the ray. From 2.81 and 2.89 it follows that

$$n\mathbf{K} = \nabla n - \frac{dn}{ds}\mathbf{s} \quad (2.90)$$

This relation shows that the gradient of the refractive index lies in the osculating plane of the ray. If one multiplies 2.90 scalarly by \mathbf{K} and use 2.89 finds that

$$|\mathbf{K}| = \frac{1}{\rho} = \mathbf{v} \cdot \nabla \ln n \quad (2.91)$$

Since ρ is always positive, this implies that as one proceeds along the principal normal the refractive index increases so *the ray bends towards the region of higher refractive index*.

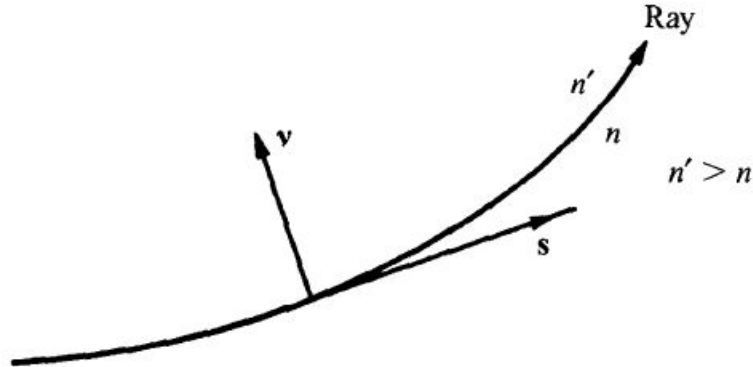


Figure 2.11: Bending a ray in an inhomogeneous(complex) medium

2.4 Electromagnetic Scattering

The scattering of electromagnetic waves by systems whose individual dimensions are small compared with a wavelength is a common and important occurrence. In such interactions it is convenient to think of the incident (radiation) fields as inducing electric and magnetic multipoles that oscillate in definite phase relationship with the incident wave and radiate energy in directions other than the direction of incidence. The exact form of the angular distribution of radiated energy is governed by the *coherent superposition* of multipoles induced by the incident fields and in general depends on the state of polarization of the incident wave. If the wavelength of the radiation is long compared to the size of the scatterer, only the lowest multipoles, usually electric and magnetic dipoles, are important. Furthermore, in these circumstances the induced dipoles can be calculated from static or quasi-static boundary-value problems[2].

The customary basic situation is for a plane monochromatic wave to be incident on a scatterer. For simplicity the surrounding medium is taken to have $\mu_r = \epsilon_r = 1$. If the incident direction is defined by the unit vector \mathbf{n}_0 , and the incident polarization vector is ϵ_0 , the incident fields are

$$\mathbf{E}_{inc} = \epsilon_0 E_0 e^{ikn_0 \cdot \mathbf{x}} \quad (2.92)$$

$$\mathbf{H}_{inc} = \mathbf{n}_0 \times \mathbf{E}_{inc} / Z_0 \quad (2.93)$$

where $k = \omega/c$ and a time-dependence $e^{-i\omega t}$ is understood. These fields induce dipole moments \mathbf{p} and \mathbf{m} in the small scatterer and these dipoles radiate energy in all directions. Far away from the scatterer, the scattered(radiated) fields are found to be:

$$\mathbf{E}_{sc} = \frac{1}{4\pi\epsilon_0} k^2 \frac{e^{ikr}}{r} [(\mathbf{n} \times \mathbf{p}) \times \mathbf{n} - \mathbf{n} \times \mathbf{m}/c] \quad (2.94)$$

$$\mathbf{H}_{sc} = \mathbf{n} \times \mathbf{E}_{sc} / Z_0 \quad (2.95)$$

where \mathbf{n} is a unit vector in the direction of observation and r is the distance away from the scatterer. The power radiated in the direction \mathbf{n} with polarization ϵ , per unit solid angle, per unit incident flux(power per unit area) in the direction \mathbf{n}_0 with polarization ϵ_0 , is a quantity with dimensions of area per unit solid angle. It is called the *differential scattering cross section*:

$$\frac{d\sigma}{d\Omega}(n, \epsilon, n_0, \epsilon_0) = \frac{r^2 \frac{1}{2Z_0} |\epsilon^* \cdot \mathbf{E}_{sc}|^2}{\frac{1}{2Z_0} |\epsilon_0^* \cdot \mathbf{E}_{inc}|^2} \quad (2.96)$$

Since instruments called radar are usually used to measure electromagnetic scattering of objects; the scattering cross section will be referred to in the following as *radar cross section*.

A radar detects or tracks a target, and sometimes can identify it, only because there is an echo signal. It is therefore critical in the design and operation of radars to be able to quantify or otherwise describe the echo, especially in terms of such target characteristics as size, shape and orientation. For that purpose the target is ascribed an effective area called the *radar cross section*. The echo characteristics depend in strong measure on the size and nature of the target surfaces exposed to the radar beam and on the incident wave frequency. The variation is small for electrically small targets (targets less than a wavelength size) because the incident wavelength is too long to resolve target details. On the other hand, the flat, singly curved and doubly curved surfaces of electrically large targets each give rise to different echo characteristics [3].

The radar cross sections of simple bodies can be computed exactly by a solution of the wave equation in a coordinate system for which a constant coordinate coincides with the surface of the body. The exact solution requires that the electric and magnetic fields just inside and outside the surface satisfy certain conditions that depend on the electromagnetic properties of the material of which the body is made.

An alternative approach is the solution of the integral equations governing the distribution of induced fields on target surfaces. The most useful approach at solution is known as the *method of moments*, in which the integral equations are reduced to a system of linear homogeneous equations. Alternatives to these exact solutions are several approximate methods that may be applied with reasonable accuracy to electrically large target features. They include the theories of geometrical and physical optics, the geometrical and physical theories of diffraction, and the method of equivalent currents.

2.4.1 Definition of RCS

An object exposed to an electromagnetic wave disperses incident energy in all directions. This spatial distribution of energy is called *scattering*, and the object itself is often called a *scatterer*. The energy scattered back to the source of the wave (called backscattering) constitutes the *radar echo* of the object. The intensity of the echo is described explicitly by the radar cross section of the object. The formal definition of radar cross section is:

$$\sigma = \lim_{R \rightarrow \infty} 4\pi R^2 \frac{|E_s|^2}{|E_0|^2} \quad (2.97)$$

where E_0 is the electric-field strength of the incident wave impinging on the target and E_s is the electric-field strength of the scattered wave at the radar. This permits one to calculate the scattered power density on the surface of a large sphere of radius R centered on the scattering object. R is typically taken to be the range from the radar to the target.

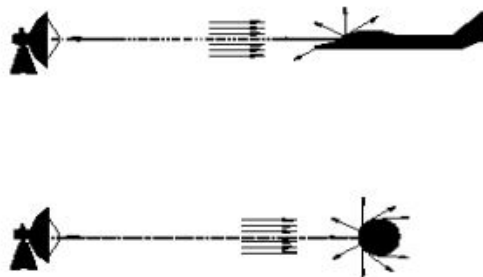


Figure 2.12: Concept of RCS

The limiting process in 2.97 is not always an absolute requirement. In both measurement and analysis, the radar receiver and transmitter are usually taken to be in the far field of the target, and at that distance the scattered field E_s decays inversely with the distance R . Thus, the R^2 term in the numerator is canceled by an identical but implicit R^2 term in the denominator. Consequently the dependence of the RCS on R , and the need to form the limit, usually disappears. Radar cross section is therefore a comparison of the scattered power density at the receiver with the incident power density at the target.

It is often necessary to measure or calculate the power scattered in some other direction than back to the transmitter, a *bistatic* situation. A bistatic RCS may be defined for this case as well as for backscattering, provided it is understood that the distance R is measured from the target to the receiver.

Example of RCS characteristics on simple object

Because of its pure radial symmetry, the PEC sphere is the simplest of all three-dimensional scatterers. Despite the simplicity of its geometrical surface, however, and the invariance of its echo with orientation, the RCS of the sphere varies considerably with electrical size. The exact solution for the scattering by a conducting sphere is known as the Mie series, and it is shown in the figure below.

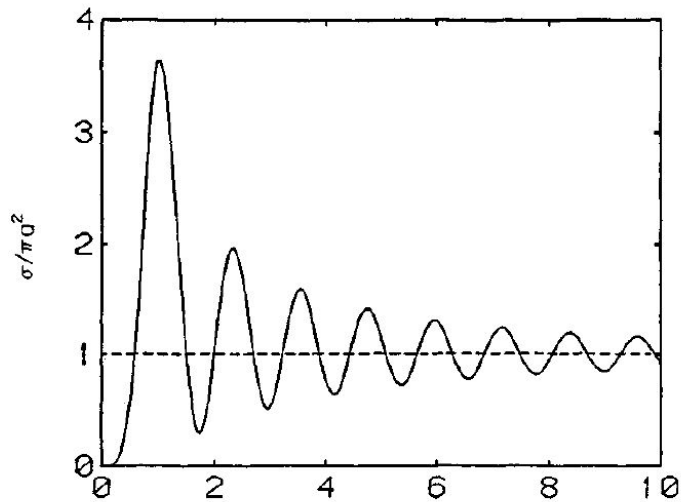


Figure 2.13: RCS of a perfectly conducting sphere as a function of its electrical size ka

The parameter $ka = 2/\lambda$ is the circumference of the sphere expressed in wavelengths, and the RCS is shown normalized with respect to the projected area of the sphere. The RCS rises quickly from a value of zero to a peak near $ka = 1$ and then executes a series of decaying undulations as the sphere becomes electrically larger. The undulations are due to the interference of two distinct contributions to the echo, one a *specular reflection* from the front of the sphere and the other a *creeping wave* that skirts the shadowed side. The two go in and out of phase because the difference in their electrical path lengths increases continuously with increasing ka . The undulations become weaker with increasing ka because the creeping wave loses more energy the longer the electrical path traveled around the shadowed side.

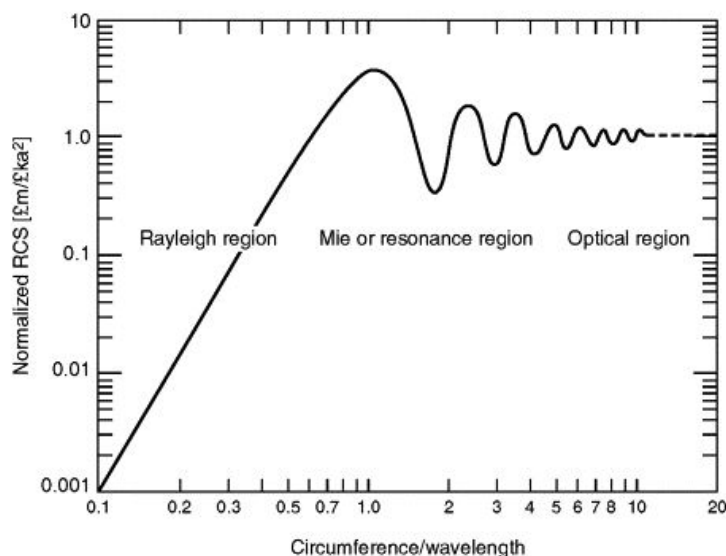


Figure 2.14: Log-log plot of the data displayed in Fig. 2.13

The log-log plot of Fig.2.14 reveals the rapid rise in the RCS in the region $0 < ka < 1$, which is known as the *Reyleigh region*. Here the normalized RCS increases with the fourth power of ka , a feature shared by other electrically small or thin structures. The central region characterized by the interference between the specular and creeping-wave contributions is known as the *resonance region*. There is no clear upper boundary for this part of the curve, but a value near $ka = 10$ is accepted. The region $ka > 10$ is dominated by the specular return from the front of the sphere and is called the *optics region*. For spheres of these sizes the geometric optics approximation πa^2 is usually an adequate representation of the magnitude of the RCS.

The echoes of all scattering objects, and not just the perfectly conducting sphere, can be grouped according to the electrical-size characteristics of the object. The dimensions of a Rayleigh scatterer are much less than a wavelength, and the RCS is proportional to the square of the volume of the body. Resonant scatterers are generally of the order of one-half to 10 wavelength in size, for which neither Rayleigh nor optics approximations are available for making estimates or predictions.

The echo characteristics of permeable (dielectric) bodies can be more complicated than those of perfect conductors because energy may enter the body and suffer several internal bounces before emerging.

2.4.2 RCS prediction techniques

Although the complexity and size of most scattering objects preclude the application of exact methods of radar cross sections prediction, exact solutions for simple bodies provide valuable checks for approximate methods. The exact methods are restricted to relatively simple or relatively small objects in the Reyleigh and resonant regions, while most of the approximate methods have been developed for the optics region. There are exceptions to these general limitations, of course; The exact solutions for many objects can be used for large bodies in the optics region if one uses arithmetic of sufficient precision, and many of the optics approximations can be extended to bodies of modest electrical size in the resonance region. Low frequency approximations developed for the Reyleigh region can extend nearly into the resonance region.

Exact Methods

Differential Equations The exact methods are based on either the integral or differential form of Maxwell's equations. Maxwell's four differential equations constitute a succinct statement of the relationship between electric and magnetic fields produced by currents and charges and by each other. The four equations may be manipulated for isotropic source-free regions to generate the wave equation described in Chapter 2:

$$\nabla^2 \mathbf{F} + k^2 \mathbf{F} = 0 \quad (2.98)$$

where \mathbf{F} represents either the electric field or the magnetic field. The wave equation is a second order differential equation which may be solved as a boundary-value problem when the fields on the surface of the scattering obstacle are specified. The fields are typically represented as the sum of known and unknown components (incident and scattered fields), and the boundary conditions are the known relationships that must be satisfied between the fields (both electric and magnetic) just inside and just outside the surface of the obstacle exposed to the incident wave. Those boundary conditions are particularly simple for solid conducting or dielectric objects.

The boundary conditions involve all three components of the vector fields, and the surface of the body is described. The solution of the wave equation is most useful for those systems in which the equation is separable into ordinary differential equations in each of the variables. The scattered fields are to be determined in the actual solution of the problem. The solution allows the fields to be calculated at any point in space, which in RCS problems is the limit as the distance from the obstacle becomes infinite.

An example of a solution of the wave equation is the following infinite series for a

perfectly conducting sphere:

$$\frac{\sigma}{\pi a} = \left| \sum_{n=1}^{\infty} \frac{(-1)^n (2n+1)}{f_n(ka) [ka f_{n-1}(ka) - n f_n(ka)]} \right|^2 \quad (2.99)$$

The function $f_n(x)$ is a combination of spherical Bessel functions of order n and may be formed from the two immediately lower order functions by means of the recursion relationship

$$f_n(x) = \frac{2n-1}{x} f_{n-1}(x) - f_{n-2}(x) \quad (2.100)$$

An efficient computational algorithm may be developed by using the two lowest orders as starting values

$$f_0(x) = 1 \quad (2.101)$$

$$f_1(x) = (1/x) - i \quad (2.102)$$

Integral Equations (MoM) Maxwell's equations may also be manipulated to generate a pair of integral equations (known as the Stratton-Chu equations):

$$E_s = \oint [ikZ_0(\mathbf{n} \times \mathbf{H})\psi + (\mathbf{n} \times \mathbf{E}) \times \nabla\psi + (\mathbf{n} \cdot \mathbf{E})\nabla\psi] dS \quad (2.103)$$

$$H_s = \oint [-ikY_0(\mathbf{n} \times \mathbf{E})\psi + (\mathbf{n} \times \mathbf{H}) \times \nabla\psi + (\mathbf{n} \cdot \mathbf{H})\nabla\psi] dS \quad (2.104)$$

where \mathbf{n} is the unit surface normal erected at the surface patch dS and the Green's function ψ is:

$$\psi = \frac{e^{ikr}}{4\pi r} \quad (2.105)$$

The distance r in 2.105 is measured from the surface patch dS to the point at which the scattered fields are desired. These expressions state that if the total electric and magnetic field distributions are known over a closed surface S , the scattered fields anywhere in space may be computed by summing (integrating) those surface field distributions.

The surface field distributions may be interpreted as induced electric and magnetic currents and charges, which become unknowns to be determined in a solution. The two equations are coupled because the unknowns appear in both. Unknown quantities also appear on both sides of the equations because the induced fields include the known incident field intensity and the unknown scattered field intensity. The method of solution is known as the *method of moments*, reducing the integral

equations to a collection of homogeneous linear equations which may be solved by matrix techniques.

The solution of the integral equations begins with the specification of the relation between the incident and scattered fields on the surface S , as governed by the material of which the object is made. If the body is perfectly conducting or if the electric and magnetic surface fields can be related by a constant (the surface impedance boundary conditions), the equations become decoupled, and only one or the other need to be solved. If the body is not homogeneous, the fields must be sampled at intervals within its interior volume, complicating the solution.

Once the boundary conditions have been specified, the surface S is splitted into a collection of small discrete patches, as suggested in Fig. 2.15. The patches must be small enough (typically less than 0.2λ) that the unknown currents and charges on each patch are constant or at least can be described by simple functions. A weighing function may be assigned to each patch, and the problem is essentially solved when the amplitude and phase of those functions have been determined.

The point of observation is forced down to a general surface patch, whereupon the fields on the left sides of eq.2.103 and 2.104 are those due to the coupling of the fields on all other patches, plus the incident fields and a 'self-field'. The self-field (or current or charge) is moved to the right side of the equations, leaving only the known incident field on the left side. When the process is repeated for each patch on the surface, a system of $2n$ linear homogeneous equations in $2n$ unknowns is generated. If the boundary conditions permit the decoupling of the equations, the number of unknowns may be helved. The coefficients of the resulting matrix involve only the electrical distances (in wavelengths) between all patches taken by pairs and the orientation of the patch surface normals. The unknown fields may be found by inverting the resulting matrix and multiplying the inverted matrix by a column matrix representing the incident field at each patch. The surface fields are then summed in integrals like eq.2.103 and 2.104 to obtain the scattered field, which then may be inserted in eq. 2.97 to compute RCS.

The method of moments has become a powerful tool in the prediction and analysis of electromagnetic scattering, but it has three limitations however.

First because of computer memory and processing time both increase rapidly with the electrical size of the object, MOM is economically restricted to objects not much more than a few wavelengths, or perhaps a few dozen wavelengths, in size. The second limitation is that MOM yields numbers, not formulas, and is therefore a numerical experimental tool. Third, the solutions for some objects may contain spurious resonances that do not actually exist, thereby reducing the confidence one may have in applying the method to arbitrary structures.

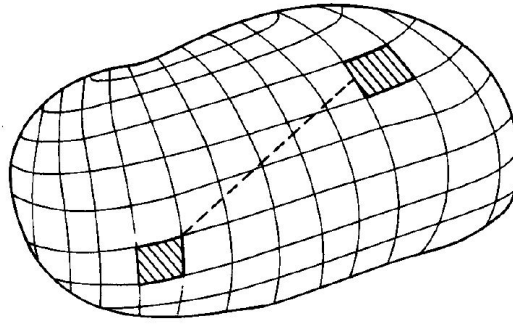


Figure 2.15: The MoM divides the body surface into a collection of discrete patches

Approximate Methods

Approximate methods for computing scattered fields are available in both the Rayleigh and the optics regions. Rayleigh region approximations may be derived by expanding the wave equation in a power series of the wavenumber k . The expansion is quasi-static for small wavenumbers (long wavelengths compared with typical body dimensions), and higher order terms become progressively more difficult to obtain. The RCS pattern of a Rayleigh scatterer is very broad, especially if the object has similar transverse and longitudinal dimensions. The magnitude of the echo is proportional to the square of the volume of the object and varies as the fourth power of the frequency of the incident wave.

Several approximate methods have been devised for the optic region, each with its particular advantage and limitations. The most mature of the methods are *geometrical optics* and *physical optics approximation*, with later methods attacking the problem of diffraction from edges and shadow boundaries. While the general accuracy of the optics region approximations improves as the scattering obstacle becomes electrically larger, some of them give reasonably accurate results (within 1 or 2 dB) for objects as small as a wavelength or so.

The theory of geometric optics is based on the conservation of energy within a slender fictitious tube called a ray as described in Sec. 2.3.3. The direction of propagation is along the tube, and contours of equal phase are perpendicular to it. In a lossless medium, all the energy entering the tube at one end must come out to the other as seen in previous chapter, but energy losses within the medium may also be accounted for. An incident wave may be represented as a collection of a large number of rays, and when a ray strikes a surface, part of the energy is reflected and part is transmitted across the surface. The amplitude and phase of the reflected and transmitted rays depends on the properties of the media on either side of the surface. The reflection is perfect if the surface is PEC, and no energy

is transmitted across the boundary. When energy can pass through the surface, transmitted rays are bent toward the surface normal in crossing a surface into an electrically denser medium (higher index of refraction) and away from the surface normal into a less dense medium. This bending of rays is called refraction.

Depending on surface curvature and body material, reflected and transmitted rays may diverge from one another or they may converge toward each other. This dependence is the basis for the design of lenses and reflectors at radar wavelengths as well as optical wavelengths.

The reduction in intensity as the rays diverge (spread away) from the point of reflection can be calculated from the curvatures of the reflecting surface and the incident wave at the specular point [4], that point on the surface where the angle of reflection equals the angle of incidence. The principal radius of curvature of the surface are measured in two orthogonal planes at the specular point, as shown in Fig. 2.16 . When the incident wave is planar and the direction of interest is back toward the source, the geometric optics RCS is simply:

$$\sigma = \pi a_1 a_2 \tag{2.106}$$

where a_1 and a_2 are the radii of curvature of the body surface at the specular point.

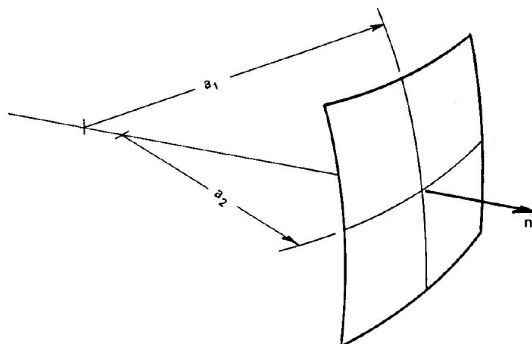


Figure 2.16: The GO RCS of a doubly curved surface depends on the principal radii of curvature at the specular point. The specular point is that point on the surface where the surface normal points toward the radar

This formula becomes exact in the optical limit of vanishing wavelengths and is probably accurate to 10 or 15 percent for radii of curvatures as small as 2 or 3 wavelengths. It assumes that the specular point is not close to an edge. When applied to dielectric objects, the expression should be multiplied by the square of the voltage reflection coefficient associated with the material properties of the object. Internal reflections should also be accounted for, and the phase of internally reflected rays adjusted according to the electrical path lengths traverse within the

body material. The net RCS should be computed as the coherent sum of the surface reflection plus all significant internal reflections. Eq. 2.106 fails when one or both surface radii of curvature at the specular point become infinite, yielding infinite RCS, which is obviously wrong. This occurs for flat and singly curved surfaces.

The theory of physical optics (PO) is a suitable alternative for bodies with flat and singly curved features. The theory is based on two approximations in the application of eq. 2.98 and 2.99, both of which are reasonably effective approximations in a host of practical cases. The first is the *far-field approximation*, which assumes that the distance from the scattering obstacle to the point of observation is large compared with any dimension of the obstacle itself. This allows one to replace the gradient of Green's function with:

$$\nabla\psi = ik\psi_0\mathbf{s} \quad (2.107)$$

$$\psi_0 = \frac{e^{ik\mathbf{r}\cdot\mathbf{s}} e^{ikR_0}}{a_0} \quad (2.108)$$

where \mathbf{r} is the position vector of integration patch dS and \mathbf{s} is a unit vector pointing from an origin in or near the object to the far-field observation point, usually back toward the radar. R_0 is the distance from the origin of the object to the far-field observation point.

The second is the *tangent plane approximation*, in which the tangential field component $\mathbf{n} \times \mathbf{E}$ and $\mathbf{n} \times \mathbf{H}$ are approximated by their geometric optics values. That is, a tangent plane is passed through the surface coordinate at the patch dS , and the total surface fields are taken to be precisely those that would have existed had the surface at dS been infinite and perfectly flat. Thus the unknown in the integrals of the previous equations may be expressed entirely in terms of the known incident field values. The problem then becomes one of evaluating one of the two integrals and substituting the result into eq. 2.97 to obtain RCS.

Chapter 3

LACE RT Code

At the heart of this thesis work is a computational code developed at the Antennas and Electromagnetic Compatibility Laboratory at the LINKS Foundation[5]. It has been realized with the aim of studying the propagation of electromagnetic waves within complex media such as the plasma formed in vehicles flying through atmosphere in hypersonic regime ($Mach > 5$). It is possible to study the propagation properties of RF waves and try to mitigate detrimental effect on the radio links, the so-called RF blackout or brownout in case partial reduction of the signal strength. Similarly the radar return, the RCS described in the previous chapter can be evaluated in support and development of radar systems. This problem of calculating the far-field was addressed with a hybrid approach, first applying the Equivalence Theorem to separate the inhomogeneous plasma region from the surrounding free space via an equivalent (Huygens) surface, and the Eikonal approximation to Maxwell equations in the large inhomogeneous region (ray-tracing) for obtaining equivalent currents on the separating surface. Then, the diffuse field was obtained via the (exact) free-space radiation of these equivalent surface currents. This chapter will describe the physical and numerical model used in the code.

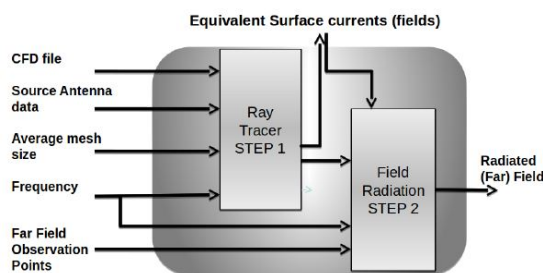


Figure 3.1: Algorithm overview with input and output data.

3.1 Physical Model

The medium is supposed to be stationary; a time-dependence $\exp(-i\omega t)$ in the EM fields is assumed and suppressed, with $\omega = 2\pi f$ being the angular frequency at frequency f . One is interested in the frequency range where the plasma response is dominated by the electron motion; considering collisional effects in the plasma and neutral particles, but as the the wave phase velocity is much greater than plasma thermal velocity, temperature and higher order collective kinetic effects can be left out. This is the so-called collisional unmagnetised “cold plasma” approximation in standard literature. In this regime the dielectric tensor is diagonal and the proper plasma constitutive relation is:

$$\epsilon_r(\mathbf{r}) = 1 - \frac{\omega_{pe}^2(\mathbf{r})}{\omega(\omega - i\nu_c(\mathbf{r}))} \quad (3.1)$$

where $\omega_{pe}^2 = n_e e^2 / (\epsilon_0 m_e)$ is the electron plasma frequency (squared), n_e the electron density, m_e the electron mass, ϵ_0 the vacuum permittivity and ν_c is the neutral-plasma collision frequency. Equation 3.1 is also equivalent to well-known Appleton-Hartree equation (in the special case of no magnetic field), which has been extensively applied to ionospheric propagation. For multi species partially ionised plasmas the collision frequency is related to temperature via:

$$\nu_c(\mathbf{r}) = \sum_{\alpha} n_{\alpha,0}(\mathbf{r}) \sigma_{\alpha,0}(T_e(\mathbf{r})) \sqrt{\frac{8k_B T_e(\mathbf{r})}{\pi m_e}} \quad (3.2)$$

with T_e being the electron temperature, n_0 the neutral density, k_B the Boltzmann constant and $\sigma_{\alpha,0}$ is the neutral-electron scattering cross section for the neutral specie α . The collisional frequency is a function of T_e through both the electron mean velocity and the scattering cross section. In a single ideal gas approximation a representative value of σ_c for hot air is $1 \cdot 10^{-19} m^{-2}$.

In this model, the spatial distribution of the hypersonic flow and of the related plasma parameters are known in numerical form from CFD simulations. Hence, data representation must be made consistent with the EM model. It has been necessary to compute both the relative electric permittivity and its gradient for a very high number of spatial locations; due to data origin, the gradient has to be computed numerically. If not done with care, this step may lead to inaccurate EM field calculation and/or very high computational cost. Moreover, the plasma profiles are typically computed in CFD simulation on an unstructured spatial grid. Most of the accurate and fast multivariate interpolation methods are available for regular gridded data set only, which makes the gradient calculation a critical data processing. It has been chosen to process the CFD 3D plasma profiles in two steps. First, by interpolating $\epsilon(r)$ on a regular rectangular grid with typical resolution of $\approx \lambda/5$. Second, by fitting the regular grid using a global cubic spline, that allows a

rapid and smooth evaluation of the gradient, which is continuous by construction. The overall physical model of the scattering problem is shown in Fig. 3.2. There are one or more impenetrable objects (in black) immersed into an inhomogeneous medium (coloured map) defined by the dielectric function $\epsilon(r)$ (possibly complex).

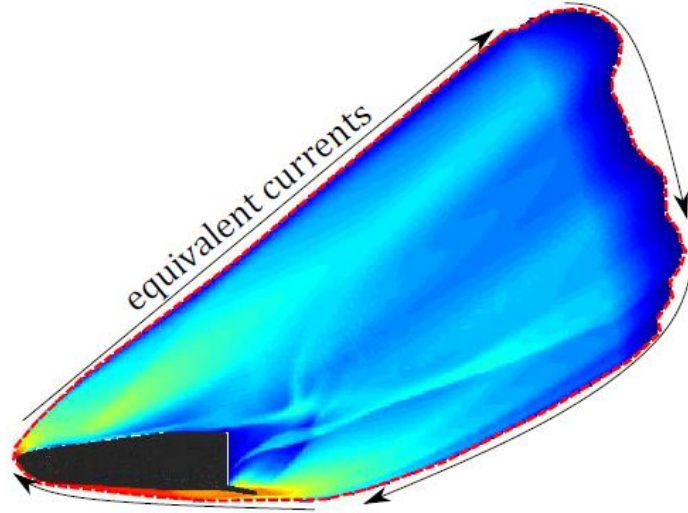


Figure 3.2: Schematic of the physical model. Inhomogeneous media (here plasma surrounding a vessel) are enclosed by an equivalent surface (dashed red line) on which equivalent currents radiate to the outside.

The source can be internal to the inhomogeneous dielectric, as is the case for an antenna on a vehicle, or external, such as an incident plane wave, as it is the case for RCS computations. Equivalence Theorem has been employed to separate the inhomogeneous [4] region from the surrounding free space via an equivalent (Huygens) surface. The scattered field is obtained via free space radiation of the magnetic and electric surface equivalent currents $\mathbf{M}_s = -\mathbf{n} \times \mathbf{E}$ and $\mathbf{J}_s = \mathbf{n} \times \mathbf{H}$, where \mathbf{E} and \mathbf{H} are the electric and magnetic fields on the equivalence surface, and \mathbf{n} is the surface normal unit vector.

Of particular interest are situations where the plasma volume is electrically large, and its density varies slowly compared to the operational wavelength λ ; hence, it's possible to employ the Eikonal approximation to Maxwell equations in the inhomogeneous region; under these conditions the applied method is more efficient than the full-wave methods such as FEM or FDTD, where the computational cost becomes prohibitive. Note that the mentioned use of the Equivalence Theorem

does not involve any approximation for radiation outside the inhomogeneous region. Rays originate either from the antenna location (radio link case) or from outside the plasma region (RCS case). There is no physical discontinuity between plasma and free space, avoiding the need to generate both reflected and refracted rays at interfaces. Regardless of their origin point, rays are followed (Ray Tracing) until they intersect the equivalent surface, where their contribution to the (equivalent) field is calculated. For the case of incident wave source, where rays start outside the equivalent surface, both entrance and exit intersections are considered. Once the fields at the equivalent surface are calculated by ray-tracing, they are converted to surface current via the Equivalence Theorem and made radiate in free space generating the far total (radio link case) or scattered (RCS case) field.

The Eikonal solution is an approximate one, and thus it is convenient to limit its region of application as much as possible; hence, the equivalence surface is chosen to enclose only points where plasma effects are not negligible (from that point outwards, radiation is exact). However, there are situations where rays encounter caustics, and on such surfaces the field approximation is inaccurate; when this happens close to the equivalence surface, it is then necessary to move such a surface outwards.

3.2 Numerical Model

To compute the electromagnetic wave propagation into inhomogeneous media the classical Eikonal theory described in Sec. 2.2.2 has been adopted. The Eikonal field approximation can be expressed as follows:

$$\mathbf{E}(\mathbf{r}) = \mathbf{e}(\mathbf{r})E(\mathbf{r})e^{ik_0S(\mathbf{r})} \quad (3.3)$$

where $E(\mathbf{r})$ is a slowly varying field, \mathbf{e} is the unit polarisation vector, and $S(\mathbf{r})$ is the normalised Eikonal phase function (defining the wave-front surface). This ansatz is inserted into Maxwell equations, with the assumption that the medium properties are weakly dependent on the spatial coordinate (see below for discussion of validity), which yields the hierarchy of equations for the Eikonal function, energy (power density) and the polarization. In the following the specific choices for the numerical implementation of this set of equations will be described. First, the ray trajectory equation is expressed as a system of first order Ordinary Differential Equations (ODEs) using the normalised wavevector $\xi = \nabla S$ as dynamic variable and the electrical path length differential $d\sigma = Re(\sqrt{\epsilon_r})ds$, where s is the arc-length along the trajectory; this results in:

$$\frac{d\mathbf{r}}{d\sigma} = \frac{\xi}{Re(\epsilon_r)} \quad (3.4)$$

$$\frac{d}{d\sigma} = \frac{1}{2\text{Re}(\epsilon_r)} \nabla \text{Re}(\epsilon_r) \quad (3.5)$$

To the next order of the hierarchy, one has the power density and polarization transport, that assume the solution of the trajectory equations. The complex polarisation unit vector \hat{e} obeys the following equation along the ray trajectory:

$$\frac{d\hat{e}}{d\sigma} = -\left(\hat{e} \cdot \frac{d\xi}{d\sigma}\right) \frac{\xi}{|\xi|^2} \quad (3.6)$$

As the trajectory equations 3.4, this equation is integrated with standard ordinary differential equations (ODE) techniques. 3.4 and 3.5 have been chosen because they have shown to be more stable in complex geometries; this results from the absence of high order curve differentials that would need to be computing after ray tracing. Furthermore, these formulas are easily integrated into ODE solution involved in ray tracing, which enables more efficient and accurate computations. Energy transport requires considering that the plasma is possibly lossy due to collisions; moderate dissipation is assumed. The transport equation for the field energy can be cast into the form of a divergence equation with a linear dissipation term coming from the anti-hermitian part of the dielectric tensor (simply $\text{Im}(\epsilon(r))$ in the isotropic case) as:

$$\nabla \cdot (v\hat{\mathbf{t}}U) = ck_0 \frac{\text{Im}(\epsilon_r)}{\text{Re}(\epsilon_r)} U \quad (3.7)$$

where c is the vacuum speed of light, $\hat{\mathbf{t}}$ is the unit vector along the trajectory, k_0 is the free-space wave number and $U = \text{Re}(\epsilon_r)|E|^2$ is the electromagnetic energy density in Eikonal approximation. Equation 3.7 shows the interplay between:

1. the divergence of rays due to the local variations of the local index
2. the energy absorption by the lossy medium, embedded in the imaginary part of ϵ_r
3. the wave amplitude $|E|$

Phase and amplitude transport in our case result in the following relationship between (complex) amplitudes at two points P_1 and P_2 along a ray path:

$$E(P_2) = E(P_1) \sqrt{\frac{\text{Re}(n_2)}{\text{Re}(n_1)}} DF \exp(i\Phi - \alpha) \quad (3.8)$$

where $n_l = \sqrt{\epsilon_r(P_l)}$ is the complex refractive index evaluated at P_l , with $l = 1, 2$, and

$$\alpha = k_0/2 \int_{\gamma} \frac{Im(\epsilon_r(\mathbf{r}))}{Re(\epsilon_r(\mathbf{r}))} d\sigma, \Phi = k_0 \int_{\gamma} d\sigma \quad (3.9)$$

where γ is a parametrization of the ray trajectory between points P_1 and P_2 , namely $\gamma : [\sigma_1, \sigma_2] \rightarrow \mathbb{R}^3$ with $\gamma(\sigma_1) = P_1$ and $\gamma(\sigma_2) = P_2$ and γ obeys to 3.4 and 3.5. In 3.8 DF indicates the divergence factor that accounts for divergence of the infinitesimal ray tube (i.e. along an individual ray) in a lossless medium; it represents the shrinking or expansion of the wave front surface along its propagation. The medium properties needed for evaluating the ray path and equations (3.8,3.9) are either computed from analytical models or via numerical interpolation of gridded data.

3.2.1 Ray Tube Approach

Because of the expected complexity of the ray set as a whole, a shift from a ray-based approach, as common in the related literature, to a ray-tube based description of the relevant field quantities has been performed. This allows to include collective effects such as ray folds (e.g. caustics) that are not directly present in the individual ray descriptors, and to express amplitude and radiation in a more effective manner. To do this, rays have been grouped in bundles of three, that represents the discretization of the wavefront with triangular patches (see figure 3.3), on the basis of geometrical contiguity at launch; this only entails proper bookkeeping of trajectories. Each three-ray bundle is a ray-tube in the adopted scheme.

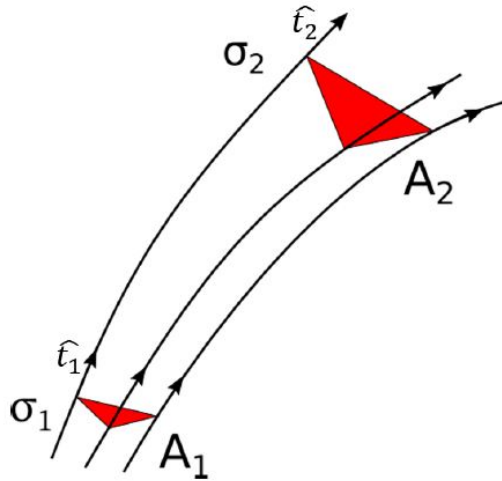


Figure 3.3: Sketch of the adopted ray tube propagation scheme.

As a first step, the equivalence surface (ES) is converted into a triangular tessellation using standard algorithms; the triangular cells have a typical side length varying in the range from $\lambda/10$ to $\lambda/3$. As said earlier on, the equivalence surface is arbitrary and may coincide with the boundary of the scattering media. Alternatively, a canonical shape such as a sphere can be chosen to encapsulate the media volume. The nodes (vertices) of the mesh determine ray launch directions. For sources in the plasma region (e.g. antennas mounted on a vehicle) ray starting directions are obtained by the directions of the vertices of the equivalent surface mesh as seen from the source location. For a plane wave source, rays start all parallel from a plane just outside the equivalence surface, with initial direction normal to the starting plane; their location (and density) is determined by back-projecting the mesh nodes along the wave direction onto the starting plane.

The initial associated field intensity and polarisation may be sampled from input antenna data or may be provided in analytical form. In figure 6 it is shown a set of rays (red lines) launched from a point just above a simple vessel (black), in free space. The rays point toward the spherical equivalence surface nodes and they are stopped at the intersection. Rays that encounter the impenetrable vessel (or any other such body) are reflected, i.e. they are stopped and re-launched with new initial conditions according to the usual specular reflection laws for fully reflective objects. A limitation of this code is precisely the fact that it can only handle reflections on PEC surfaces and thus with a simple formulation of the reflection laws; what was done through this thesis project was precisely to make it capable of handling reflections on dielectrics and thus calculating the right Fresnel coefficients and the right ray trajectories and amplitudes. Figure 7 shows an example of the electric field on the equivalence surface.

Amplitude and Radiation

Convenience of the ray-tube description is immediately evident for the amplitude calculation, and the ensuing radiation. The divergence factor (DF) appearing in amplitude propagation 3.8 can in principle be expressed in terms of the local surface principal radii. Although mathematically exact, this formulation contains higher order derivatives of the Eikonal function which may be subject to large error when the medium properties are not known analytically but resulting from other numerical calculations or measurements, as in CFD originating plasmas.

With reference to the notation of Fig. 3.3, we have that the divergence factor can be related to the changes in the front surface area simply with the relation

$$DF = \sqrt{A_1/A_2}.$$

At a difference with other approaches, the radiated field is obtained consistently with the ray-tube based approach described above. That means that the (far)

radiated field is expressed as the sum of the radiation from the patches ΔT_i defined by the intersection of the ray tubes with the chosen equivalence surface,

$$\mathbf{E}_s(r, \theta, \phi) = \sum_i \mathbf{E}_{s,i}(r, \theta, \phi) \quad (3.10)$$

an example of these patches is shown in the simple case of Fig. 3.5. The field on each triangular patch is approximated with constant magnitude and linear phase variation. The electric field vector \mathbf{E}_i is obtained as the average of the three values pertinent to the three rays of any tube, as per 3.8, 3.6 (note that the divergence factor is intrinsically a tube property, while phase, attenuation and polarization are properties of individual rays). The magnetic field \mathbf{H}_i is likewise obtained from the three values at the rays, in turn related to the electric field there by the local ray impedance relationship, and the wavefront normal $\hat{\mathbf{t}}_i$ is likewise the average of the three ray wave front normals.

With these assumptions, the patch radiated fields can be expressed as:

$$\mathbf{E}_{s,i}(r, \theta, \phi) = \frac{-ik_0}{4\pi} \frac{e^{ik_0 r}}{r} e^{-ik_0 \hat{\mathbf{r}} \cdot \mathbf{r}_i} S_i(\theta, \phi) \mathbf{a}_i \quad (3.11)$$

with

$$\mathbf{a}_i = \hat{\theta}(-\hat{\phi} \cdot \mathbf{M}_i + \hat{\theta} \cdot Z_0 \mathbf{J}_i) + \hat{\phi}(\hat{\theta} \cdot \mathbf{M}_i + \hat{\phi} \cdot Z_0 \mathbf{J}_i) \quad (3.12)$$

$$S_i(\theta, \phi) = \frac{1}{\Delta T_i} \int_{\Delta T_i} e^{ik_0(\hat{\mathbf{r}} - \hat{\mathbf{t}}) \cdot (\mathbf{r}' - \mathbf{r}_i)} d\Sigma' \quad (3.13)$$

$$\mathbf{M}_i = -\hat{\mathbf{n}}_i \times \mathbf{E}_i; \mathbf{J}_i = \hat{\mathbf{n}}_i \times \mathbf{H}_i; \quad (3.14)$$

where \mathbf{r}_i , $\hat{\mathbf{n}}_i$ and ΔT_i are the patch centroid, normal unit vector and the surface area respectively, $\hat{\theta}$, $\hat{\phi}$ are the unit vectors in the directions θ , ϕ and $\hat{\mathbf{r}}(\theta, \phi)$ the unit vector which points from the origin to the observation point, and Z_0 is the free space impedance. It turns out that the radiation shape factor S_i can be conveniently written in closed form for quick and efficient radiation calculation. We observe that this ray-tube based approach to radiation does not require to assign a surface area to individual rays on the equivalent surface. Also, in presence of complex inhomogeneity, tubes with rays diverging far apart are expected to have lower accuracy; as they result in larger areas, their contribution to radiated field is weaker: this results in an intrinsic robustness.

Folds

It is well known that the Eikonal approximation breaks down near caustics where the field becomes singular. One is, in general, not interested in the field near

the caustics; thus, the equivalent surface is generally placed sufficiently far from them (although one must often compromise with other numerical constraints). Nevertheless, caution must be taken when a ray tube passes throughout one these singular regions. Caustics arise when the ray field folds. The wave front folding affects the phase of the field carried by the wave with a phase shift of $\pi/2$ radians. These events must be accounted for, so that the proper phase shifts can be applied to the ray tube field. Caustics may be, in principle, detected by calculating the principal radii of the wave front, but again high order numerical derivatives can make this a very difficult task. Instead, the crossing of rays forming the ray tube which occurs when passing through the caustic point has been detected and a phase shift correction has been applied when needed.

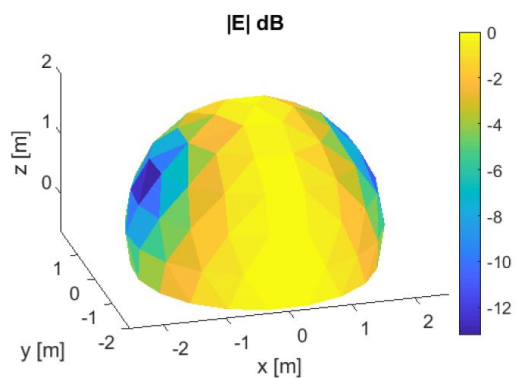
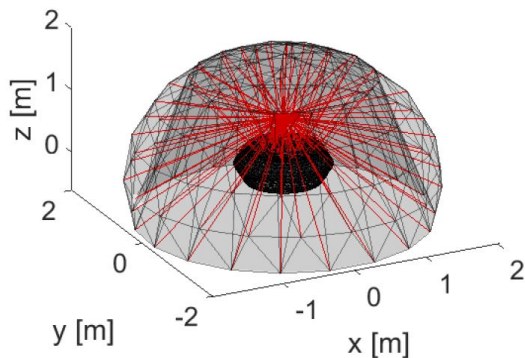


Figure 3.4: Ray trajectories (red lines) from a dipole source above a small simplified vessel, in free space. The spherical equivalence surface is also depicted (coloured).

Figure 3.5: Electric field on a spherical equivalent surface for the configuration in Fig. 3.4.

Chapter 4

Methods for Fast Ray Tracing

The classical methods also used in Computer Graphics to accelerate the ray tracing process use data structures that can divide the physical volume into subvolumes; at that point the ray tracing algorithm is divided into two main parts: a first part called Point Location where the box where a generic point is located (e.g., the first point of intersection between the ray and the box) is identified, and a second part called Ray Traversal where by exploiting the Point Location function all the intersected boxes are identified and the intersection check is performed with the object mesh patches contained in the individual boxes following the ray trajectory. The major difference between the classical Ray Traversal and the one considered in this thesis work is the trajectory of the rays; this is because in classical Ray Traversal algorithms the trajectories are considered rectilinear because the propagation of light in a vacuum is considered in order to recreate high-fidelity images; in the case of the propagation of electromagnetic waves within complex media as described in the previous chapters, the ray trajectories tend to be curvilinear; for this reason the ray is structured in a segmented manner so that curved trajectories can be modeled.

The standard method for ray traversal that will be abbreviated as Brut Force provides, once created the surface mesh of the object on which you want to calculate the reflections, to examine one by one every single patch of the mesh and check if there is an intersection with the ray; this obviously leads to an explosion of calculation time if you consider very large meshes.

To overcome this problem, binary data structures were used[6] to divide the space into multiple sub-regions and as a result an algorithm was created that allows the intersection test to be performed on only a small portion of the patches that make up the mesh and not on all of them as is done in the standard method (Brut Force).

The algorithm was implemented in MATLAB and the results showed a significant decrease in computation time confirming what was expected from the theory.

Tests were performed considering four different types of geometries with increasing complexity in order to consider multiple practical applications.

In the following, all the steps that led to the writing of this prototype algorithm will be described, starting from the description of the binary structures for the division of space until you get to the various modules that make up the algorithm; in the last part of this chapter will be presented and commented the numerical results and a version of the algorithm adaptable to the numerical model contained in the code described in the previous chapter will be presented.

4.1 Spatial Subdivision

Hierarchical data structures are important representation techniques in the domains of computer vision, image processing, computer graphics, robotics, and geographic information systems. They are based on the principle of recursive decomposition (similar to divide and conquer methods). They are used primarily as devices to sort data of more than one dimension and different spatial types.

There are several types of hierarchical structures capable of dividing physical space recursively; in this chapter the Octree and K-D tree respectively will be considered as the most efficient ones capable of handling a three-dimensional space.

4.1.1 Octree

Typically an Octree is a hierarchical data structure showing how objects are distributed in the object space, which has been mainly used in image processing or solid modeling areas. Conventional octree construction divides a three-dimensional space for each axis using the spatial median, obtains eight subspaces, which can be represented by an octree. The root node of an octree represents the entire object space. If the entire space contains more objects than a given limit, the space is divided into eight sub-spaces represented by eight children nodes. A subspace thus created is defined as a voxel. These voxels are further divided into eight voxels, and this process is repeated until the voxels satisfy the given criteria. In general, the criteria used to determine whether or not the given octree should be divided further depend upon the number of objects intersecting with a voxel and the maximum depth of an octree allowed [7].

However, the octree contains cell boundaries that are static and their location is independent of the objects. This independence makes the more intersections. The kd-tree, on the other hand, places the boundaries around the objects, especially if the empty space is cut off, thus it can result in much higher intersection probability. Furthermore, conventional octree construction uses uniform voxels to get spatial

partition, which leads to higher depth of the tree, and generates much empty nodes which waste much memory.

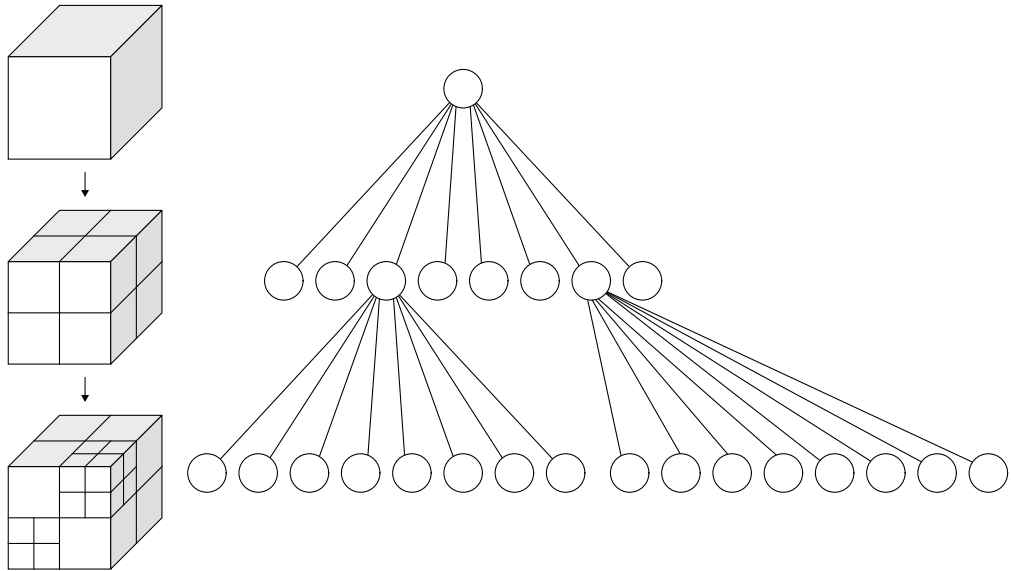


Figure 4.1: Generation of the spatial subdivision (left) and the corresponding data structure (right)

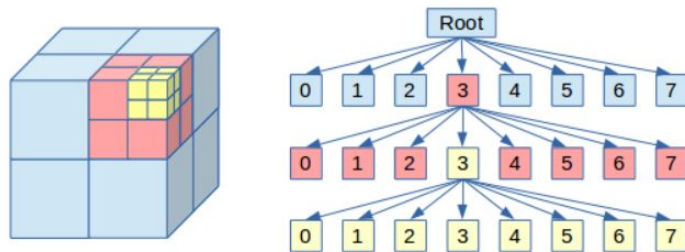


Figure 4.2: Octree Example

4.1.2 K-D Tree

A K-D Tree (also called as K-Dimensional Tree) is a binary search tree where data in each node is a K-Dimensional point in space. In short, it is a space partitioning data structure for organizing points in a K-Dimensional space.

Every non-leaf node can be thought of as implicitly generating a splitting hyperplane that divides the space into two parts, known as half-spaces. Points to the left

of this hyperplane are represented by the left subtree of that node and points to the right of the hyperplane are represented by the right subtree. The hyperplane direction is chosen in the following way: every node in the tree is associated with one of the k dimensions, with the hyperplane perpendicular to that dimension's axis. So, for example, if for a particular split the "x" axis is chosen, all points in the subtree with a smaller "x" value than the node will appear in the left subtree and all points with a larger "x" value will be in the right subtree. In such a case, the hyperplane would be set by the x value of the point, and its normal would be the unit x-axis.

Considering for sake of simplicity a 2D-Tree one has that the root would have an x-aligned plane, the root's children would both have y-aligned planes, the root's grandchildren would all have x-aligned planes, and the root's great-grandchildren would all have y-aligned planes and so on.

The choice of splitting plane can be made according to several criteria such as choosing the center of gravity of the volume to be split or the median of the points contained within the box.

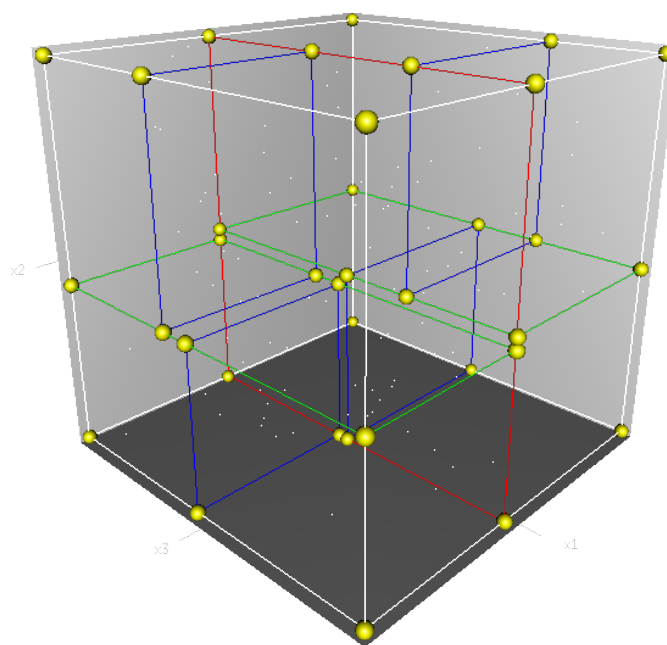


Figure 4.3: A 3-dimensional k-d tree. The first split (the red vertical plane) cuts the root cell (white) into two subcells, each of which is then split (by the green horizontal planes) into two subcells. Finally, four cells are split (by the four blue vertical planes) into two subcells. Since there is no more splitting, the final eight are called leaf cells.

4.2 K-D Tree vs. Octree

Considering the meshes of four different geometries (sphere, two spheres, sphere & cylinder, vehicle) a comparison was made between the two different spatial division methods in terms of tree levels and leaf boxes generated. This was done to check the efficiency and memory occupancy of both structures. The levels of the data structure represent the number of divisions made and a node is associated with each level, while the leaf boxes represent the last level of the structure (tree) and indicate the minimum size of the bounding boxes beyond which it is not possible to divide; this is because a criterion is imposed on the algorithm to stop space division once a defined number of mesh points (i.e., 200) are contained in a generated box. The comparison was made by setting this number of points equal to 30% 10% and 1% of the total number of mesh points for each individual geometry.

| SPHERE | | | |
|---------------|-----------------|-----------------|-----------------|
| Octree | | K-D Tree | |
| # of Levels | # of Leaf Boxes | # of Levels | # of Leaf Boxes |
| 2 | 9 | 2 | 4 |
| 3 | 73 | 5 | 16 |
| 4 | 457 | 8 | 128 |

Table 4.1: The first line refers to 30% of the points, the second to 10%, and the last to 1%.

| 2 SPHERES | | | |
|------------------|-----------------|-----------------|-----------------|
| Octree | | K-D Tree | |
| # of Levels | # of Leaf Boxes | # of Levels | # of Leaf Boxes |
| 2 | 9 | 2 | 4 |
| 4 | 73 | 5 | 16 |
| 5 | 457 | 8 | 128 |

Table 4.2: The first line refers to 30% of the points, the second to 10%, and the last to 1%.

| SPHERE & CYLINDER | | | |
|------------------------------|-----------------|-------------|-----------------|
| Octree | | K-D Tree | |
| # of Levels | # of Leaf Boxes | # of Levels | # of Leaf Boxes |
| 2 | 9 | 3 | 4 |
| 3 | 65 | 5 | 16 |
| 4 | 425 | 8 | 128 |

Table 4.3: The first line refers to 30% of the points, the second to 10%, and the last to 1%.

| VEHICLE | | | |
|----------------|-----------------|-------------|-----------------|
| Octree | | K-D Tree | |
| # of Levels | # of Leaf Boxes | # of Levels | # of Leaf Boxes |
| 2 | 9 | 2 | 4 |
| 3 | 41 | 5 | 16 |
| 5 | 729 | 8 | 128 |

Table 4.4: The first line refers to 30% of the points, the second to 10%, and the last to 1%.

Looking at the tables above, it can be seen that the K-D Tree algorithm always generates the same number of levels and leaf boxes because it goes to divide the space by 'chasing' the points that are there; Octree instead divides regardless of the points contained in a box the space into eight subboxes until the number of stop points is reached. Furthermore, it can be observed that as the complexity of the geometry increases, the number of leaf boxes generated by the Octree tends to explode while those generated by the K-D Tree tend to remain constant, this at the expense of a slight increase in the number of levels (nodes) generated. In conclusion, to accelerate the ray tracing process, the K-D Tree algorithm was chosen. The comparison of the spatial subdivision generated by the two algorithms on the vehicle is shown in Fig. 4.4 and 4.5 while for other geometries see Appendix C.

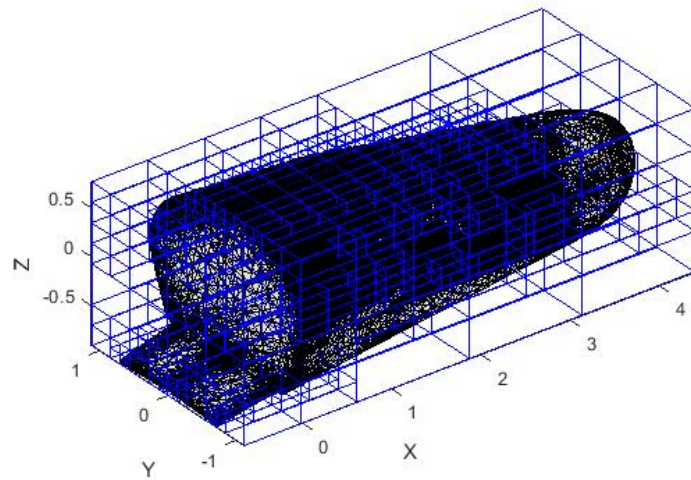


Figure 4.4: Spatial subdivision using Octree

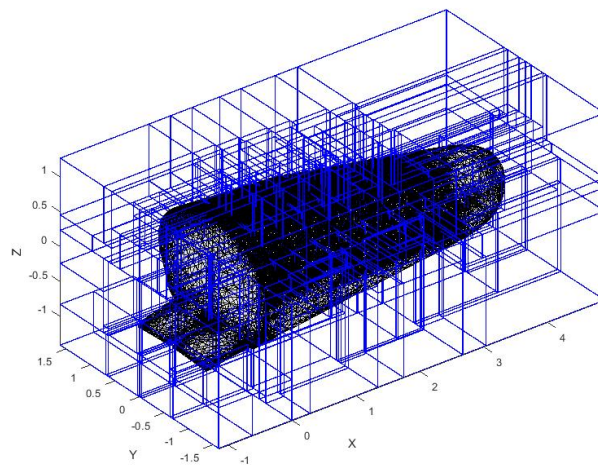


Figure 4.5: Spatial subdivision using K-D Tree

4.3 Ray Traversal algorithm using K-D Tree

In the following, straight rays modeling propagation within homogeneous media will be considered first, and ray traversal optimization algorithms will be used starting from the basic algorithms using the K-D Tree structure.

Using the basic algorithm, first a ray is intersected with an axis aligned box that covers the whole scene. This will return entry and exit distances. These will represent an interval on which an intersection of the ray with the scene is valid. When there is no intersection between the ray and the box the function returns no intersection. Otherwise one will continue by progressively finding all leaves that the ray pierces by point-location queries on the kd-tree [8].

One will start with a point that is on the entry of the ray into the scene box or if the ray origin is inside of the box this point will be the ray origin. This step is called leaf location. It is implemented by traversing the kd-tree from the root downwards: in each inner node we traverse to the child which includes the half-space containing our search point. When a leaf is found the ray is intersected with all the objects referenced in the leaf (there may be none). If there is no valid intersection that lies inside the leaf box, the next leaf location search occurs. This requires computing the exit point of the ray on the bounding box associated with the leaf. To avoid visiting the same leaf, the new point to search is moved along the ray path by a small epsilon outside the box. This is repeated until an intersection is found or the next point is outside the scene bounding box.

As this sequential (Classical) traversal algorithm has to visit the exactly same sequence of nodes several times, it is not very efficient, though it does need constant local memory for its execution which is beneficial for parallel implementations.

Moreover, the numerical stability of the algorithm is dependent on the choice of the epsilon. For scenes with very large models and/or ones that lead to kd-trees with cells having one extent equal to zero a choice of a wrong epsilon can lead to an endless loop due to the rounding of floating-point values.

After correctly implementing the optimization algorithm for straight rays, we moved on to modeling curvilinear rays by segmented lines and applied the same algorithm on the latter.

The implementation was done with different types of Leaf Location and Ray Traversal; so that multiple versions of the same algorithm could be compared so that the best one could be chosen to be used then within the LACE RT Code described in Chapter 4.

In particular for the Leaf Location the classical version and an 'original' one called then Integer Location was implemented; while for the Ray Traversal also a classical version called Sequential Traversal and one using another data structure called Neighbor Links was implemented. A pseudo-code of the implemented algorithm is given below[8].

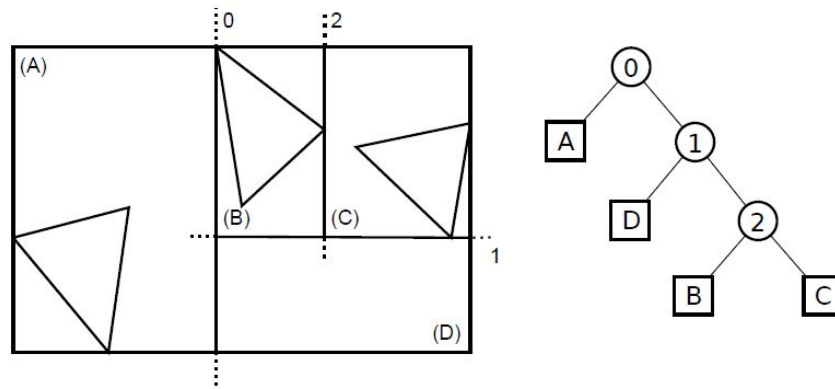


Figure 4.6: Simple scene with three triangles with a corresponding kd-tree with three leaves (boxes) and three inner nodes (circles).

```

1 Locate Leaf ( node, point)
2 begin
3   current node ← node;
4   if point lies outside node's AABB then
5     | return no leaf exists;
6   end
7   while current node is not a leaf do
8     | if point is to the left of the node's splitting plane then
9       | current node ← current node's left child;
10    | else
11    | current node ← current node's right child;
12    | end
13  end
14  return current node
15 end

```

Figure 4.7: Pseudo-code for Point Location[8]

```

16 Kd-tree Sequential Traversal:
17 begin
18   (entry distance, exit distance) ← intersect ray with root's
    AABB;
19   if ray does not intersect AABB then
20     | return no object intersected;
21   end
22   if ray has origin in AABB then
23     | point = ray origin;
24   else
25     | point = ray origin + ray direction * ( entry distance +
    eps );
26   end
    /* this will locate first leaf */
27   current node = Locate Leaf ( tree root node, point);
28   while current node is leaf do
    /* current node is a leaf while point is inside tree root
    node's AABB, see Locate Leaf lines 4-6 */
29     (entry distance, exit distance) ← intersect ray with
    current node's AABB;
30     if current node is not empty leaf then
31       | intersect ray with each object;
32       | if any intersection exists inside the leaf then
33         | | return closest object to the ray origin;
34       | end
35     end
    /* point just a bit outside the current node */
36     point = ray origin + ray direction * ( exit distance +
    eps );
37     current node = Locate Leaf ( tree root node,
    point);
38   end
39   return no object intersected;
40 end

```

Figure 4.8: Pseudo-code for Sequential(Classic) Ray Traversal[8]

4.3.1 Point Location

The Point Location function is responsible for identifying in which box leaf a generic test point is contained. To do this it takes as input the same K-D Tree structure and a generic test point (e.g., it can be the point of impact of the ray with the root box and translated by a constant epsilon) and outputs the index of the data structure corresponding to the box leaf containing the point. To do this it descends the tree starting from the root box and descending to the right or left respectively if the same coordinates of the test point are to the right or left of the splitting plane considered.

Classic Location

The classical point location method broadly follows the pseudo-code described in Fig.4.7 .Once the coordinates of the point under test are taken as input, a check is made on the various dimensions starting from the root node and then gradually moving down the tree to the leaf boxes.

For example the first check is done on the first coordinate of the point (x), if it is less than the first dimension on which the split of the space surrounding the object was done then it will proceed in the left branch of the tree, if it is greater then in the right branch; before performing the check on the second dimension operating with the same method but referring to the second dimension of the split (y), a check is performed to verify whether the current node is a leaf or not; in case it is a leaf the search stops and the corresponding index is provided in the output, otherwise the search continues by repeating the procedure on the second dimension and then verifying that the corresponding node is a leaf or not and so on. Below are the results of a test performed on the module, and it can be seen that the results are as expected, in red the test point is plotted and the leaf box that was detected by the function is highlighted, and the point falls exactly within it.

Integer Location

In this newly implemented method, an attempt has been made to optimize the classical method in terms of execution time while going, however, to increase memory occupancy.

This is because the idea behind this method is to create a three-dimensional mapping matrix once at the beginning of the algorithm. The elements of such a matrix will be the indexes of all box leaves generated by the K-D Tree structure; then taking the data structure each index of the box leaves is 'mapped' within a slot of the matrix: hence the name mapping matrix.

To do this, a new subroutine was created that taking as input the data structure of the K-D Tree goes to first identify all the values along each coordinate where cuts

were made in the three dimensions and saving these values within three vectors. The sizes of these three vectors will also go into determining the size of the mapping matrix.

Instead, in the second step, the coordinates of each of the two maximum and minimum points describing a box leaf are compared with the vectors containing the values of the cuts, and it is identified which of these values lie between the extremes of a box leaf.

The final result of this operation will be an $nx \times ny \times nz$ matrix where going to select the element of the matrix pointed by a triplet of integers representing which cut is considered along each dimension (e.g. (4,2,3) means that the fourth cut is considered along the x-coordinate, the second along the y-coordinate, and the third along the z-coordinate) will result in the output directly in the index of the corresponding box leaf.

In the Point Location function at this point the generic test point will be taken as input, its individual coordinates will be isolated, and a subtraction will be made between the test point coordinate and the vector containing all the values of the cuts along that coordinate: the index of the value less than zero contained in the vector resulting from this operation will be the index to point to along that coordinate within the mapping matrix.

The results of the test performed on this module are shown in Fig 4.10 and it can be seen that the results are the same as those of the classical method, while a schematic of the algorithm is shown in Fig 4.11.

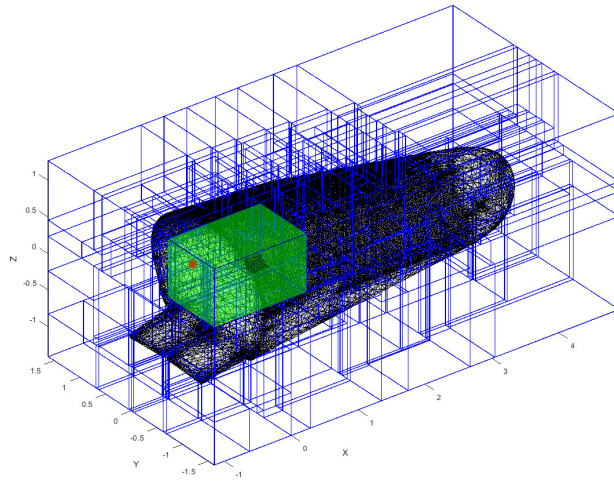


Figure 4.9: Test on the CLASSIC point location module

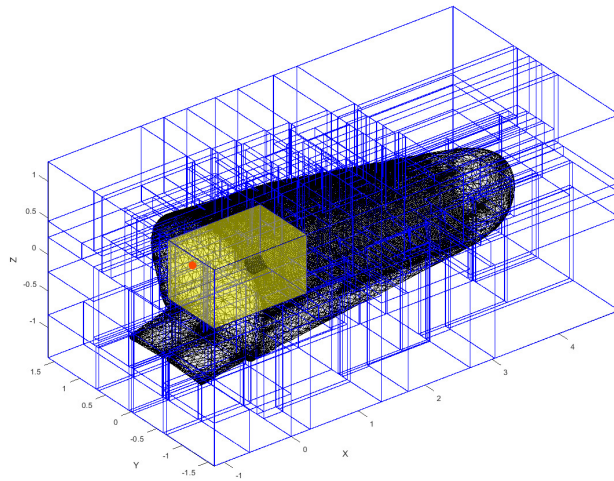


Figure 4.10: Test on the INTEGER point location module

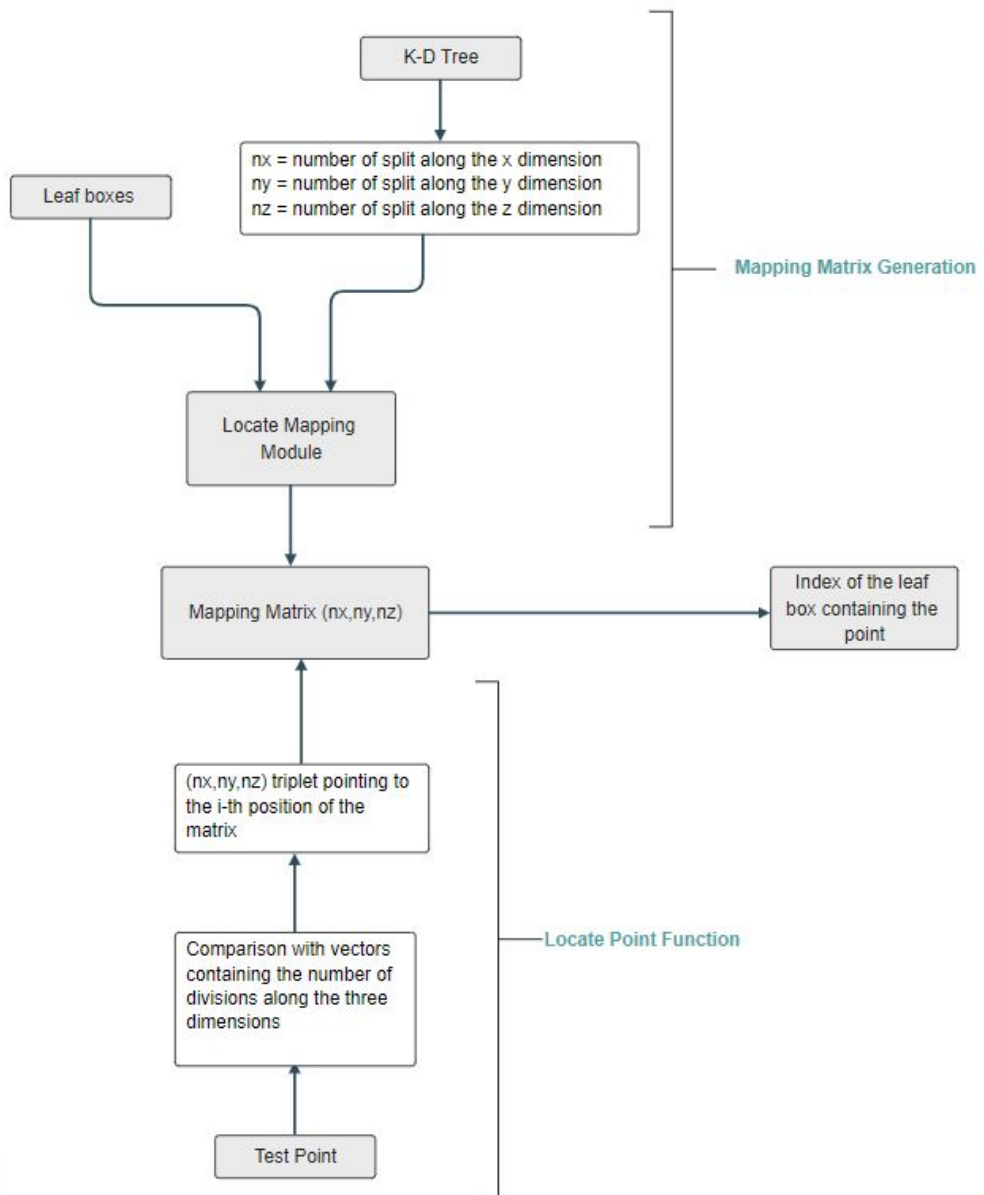


Figure 4.11: Flowchart of the new INTEGER location module

4.3.2 Ray Traversal

Once the Point Location subroutines were generated, we moved on to the next implementation, which was Ray Traversal, whereby we 'chase' the ray by exploiting the location information. The following will describe the two traversal modes implemented.

Sequential Traversal

In this 'classical' version, the pseudo-code of Fig.4.8 has been followed. In particular, once the ray has been generated, the point of impact with the root box is first searched [9] through a special subroutine; once this is done, the point is shifted by an infinitesimal amount within the root box in such a way as to ensure the correct operation of the Point Location routine; then the leaf box in which the point falls is located using the latter. Then a second intersection check is performed, but this time directly on the patches constituting the mesh; here we can see the significant advantage of this algorithm since having included in a preliminary step the information of the patches belonging to each box leaf this second intersection test is performed only on this sub-set, significantly increasing the execution time as will be shown later. If there is no intersection with the patches contained in the box leaf the exit point from the leaf is identified and also translated by the same infinitesimal amount so as to bring it into the adjacent leaf then repeating the Point Location and check on the patches. The algorithm stops in cases where the intersection with the patch is found or the ray exits the root box.

Fig. 4.12 shows the results of the full traversal algorithm, in particular the impact points with the mesh patches are highlighted. In red are the points found using the K-D Tree structure while with blue asterisk those using the Brut Force method. From the figure it can be seen that they are perfectly coincident, this result is for a test performed with 100 rays having common origin but random direction[10], tests up to 5000 rays were performed and the results were always the same: perfect coincidence between the impact points found using the Brut Force method and using the K-D Tree structure. This was to be sure that the ray tracing algorithm implemented in this way would lead to exact results. The spatial division is not shown in the image in order to have greater clarity.

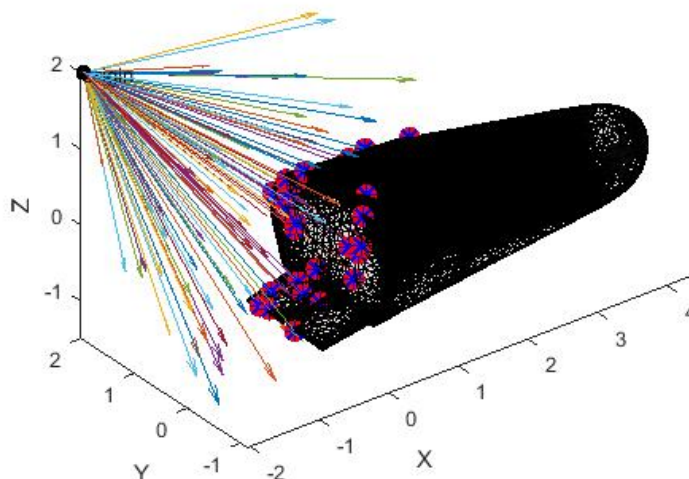


Figure 4.12: Sequential Traversal (100 rays):the blue asterisks indicate the points of intersection between the rays and the mesh found using the Brut Force method while in red those found using the K-D Tree (the spatial subdivision structure has been omitted for image clarity).

Neighbor-Link Traversal

In contrast to the sequential version of traversal, in this second implemented method if there was no impact in the first leaf box detected the next test is done directly in all its neighbors (hence the name Neighbor-Link) without using the Point Location function again.

This is at the expense of an increase in the memory used because one has to build in a preliminary step the Neighbor-Link, so there was a need to add a new field to the data structure that includes the information of the neighbors for each leaf box; to carry out this procedure a new subroutine was created that performs the check for each leaf box and detects its adjacent ones, i.e. with at least one vertex in common or in the case where a vertex of a leaf box is within the area bounded by a face of another box.

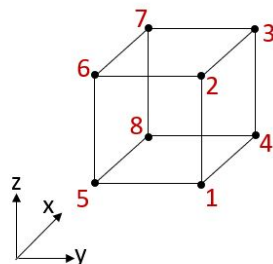


Figure 4.13: Orientation of a leaf box in the 3D space

Starting from the orientation given in three-dimensional space to the leaf boxes described in Fig. 4.12, within the subroutine to create the Neighbor-Link, box faces were defined starting from the vertices (e.g., face 1 is the one defined by vertices 1 2 3 4) and the faces adjacent to them were identified. A summary of all the faces with their respective adjacencies is given in the table below. The adjacent faces refer to the hypothetical neighboring boxes.

| Neighbor-Link | | | |
|----------------------|---------------|----------------------|-------------------------------|
| Face | Vertex | Adjacent Face | Vertex (Adjacent Face) |
| 1 | 1-2-3-4 | 3 | 5-8-7-6 |
| 2 | 1-5-6-2 | 4 | 8-4-3-7 |
| 3 | 5-8-7-6 | 1 | 1-2-3-4 |
| 4 | 8-4-3-7 | 2 | 1-5-6-2 |
| 5 | 2-6-7-3 | 6 | 4-8-5-1 |
| 6 | 4-8-5-1 | 5 | 2-6-7-3 |

Table 4.5: Neighbor-Link

Once the faces were defined, checks were made to see if each of the vertices of adjacent faces fell within the area described by the face considered for the leaf used for the test.

The results of the Neighbor-Link construction are presented in Fig. 4.13 where a flaw in the structure namely an 'overestimation' of the neighbors is also highlighted.

In other words all neighbors of a given leaf box are identified, but at the same time some neighbors of the neighbors themselves are also identified, this is because the check was performed by generating two grafted loops, one considering a test leaf in order and a second considering the leaf with the next index following the order of the structure, this led to having faces other than the neighboring one being considered neighbors.

This however only leads to a slight increase in memory occupied but does not negatively affect the Ray Traversal results as will be shown below, red highlights a test leaf box while yellow highlights all nearby 'effective' and also 'overestimated' leaf boxes.

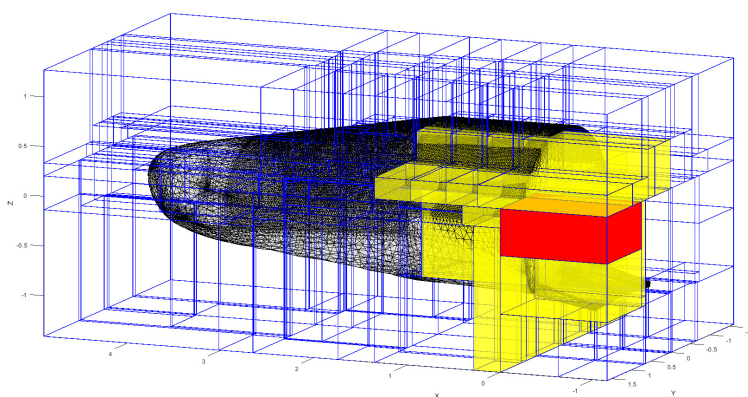


Figure 4.14: Neighbor-Link Test

Fig. 4.14 on the other hand shows the results of the test for Ray Traversal using the generated structure; as for Sequential Traversal also in this case tests up to 5000 rays were performed and it was highlighted what was said above on that having in the given structure a few more neighbors does not affect the traversal operation in the least since we have again that the points intersected with the Brut Force method and using the K-D Tree are perfectly coincident; in the figure in yellow are highlighted those found with Neighbor-Link while with blue asterisk those found with Brut Force.

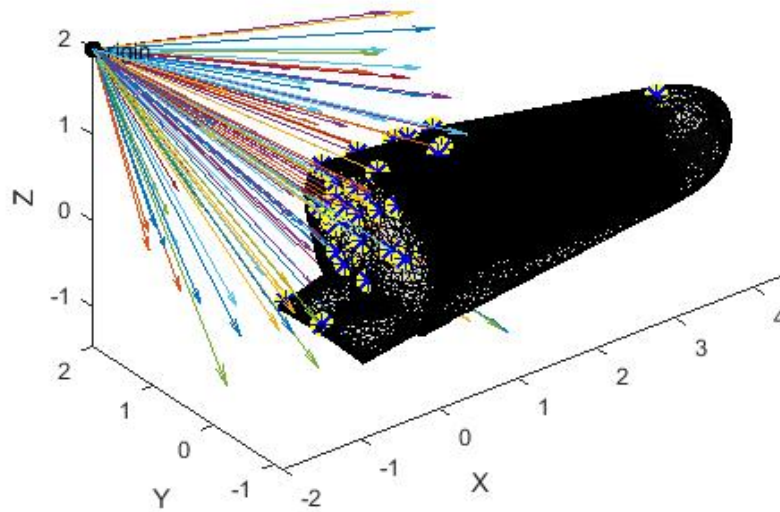


Figure 4.15: Test Neighbor-Link Traversal (100 rays):the blue asterisks indicate the points of intersection between the rays and the mesh found using the Brute Force method while in yellow those found using the K-D Tree with Neighbor-Link (the spatial subdivision structure has been omitted for image clarity).

4.4 Benchmark of Numerical Model

Once the proper functioning of the algorithm was assured, simulations were carried out for increasing numbers of rays, starting from 10 up to 5,000, and computational time measurements were taken. The simulations were carried out using an Intel(R) Core(TM) i7-4500U CPU @ 1.80GHz 2.40 GHz and considering the four geometries and algorithms described in the chapter. What was observed from the results is that by using the data structures for subdividing the space (K-D Tree) there is a significant improvement in terms of computational time (on the order of $10^2 - 10^3$ s); with regard to the various types of algorithms there is that for a low number of rays slight differences in execution time can be seen, but as this number increases they all tend to converge asymptotically to the same performance. Only results for the most complex geometry i.e., the vehicle, are reported in this section; for other results look at Appendix C.

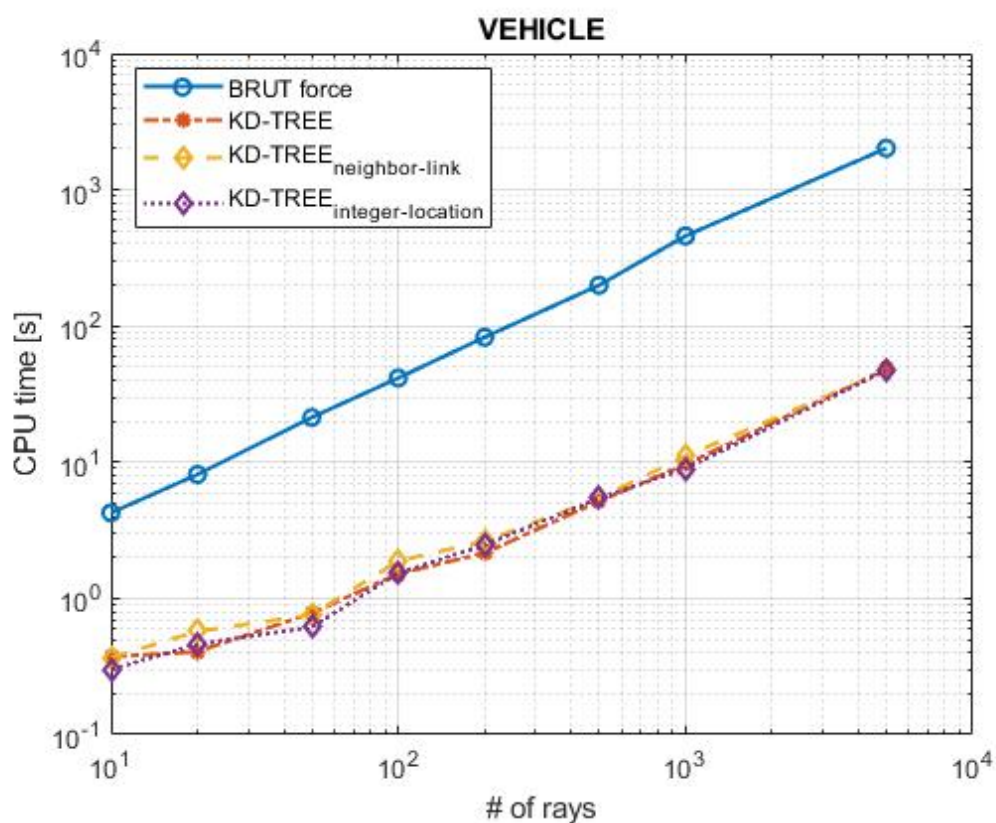


Figure 4.16: Computational Time Performance (Vehicle)

4.5 Ray Tracing for a 'Segmented' Ray

This section describes the ray traversal optimization algorithm for a ray formed by a 'segmented' line; this is because the idea behind this first part of the thesis is to apply conventional ray traversal optimization and speedup algorithms in the radio frequency domain where rays can assume curvilinear trajectories when propagating within complex media as described in Chapter 2.

Following the numerical model implemented within the code described in Chapter 3, the trajectory of the ray is constructed by small 'segments' defined by a time step that indicates the progress of the ray along its trajectory; from here we have that eventually the entire ray will be described by a 'segmented' line so that any curvatures can be considered.

For this reason within the MATLAB prototype of the ray traversal algorithm, the ray generation part was modified; whereas in the first classical version with straight lines each individual ray was described by an origin point and a vector describing its direction, in this new version each ray is defined by a series of points representing the start and end points of each segment and a time step describing the length of these segments. In particular, a time step of 0.2 seconds and a number of steps of 40 were chosen to validate that the algorithm works correctly.

The operation of the algorithm is as follows: starting from the start point one advances one time step at a time, at first a check is made to see if the end point of the current segment intersects the root box, if so one proceeds with the Point Location function on that point, if not one proceeds to the next step and adds another segment to the ray; once the intersection with the root box and the next box leaf containing the end point of the segment is found a check is made to see if that segment intersects one of the patches of the object mesh, in this case this check will be an intersection check between segment and triangle and no longer between line and triangle; if a collision has occurred between the current segment and one of the patches the traversal stops and moves on to the next ray; in case no collision had occurred with the mesh it was passed to the step, then to the segment, next; here, once the Point Location step was carried out again, it was checked whether the box in which there was the endpoint of the segment was a 'neighbor' of the previous box going to exploit the information contained in the Neighbor-Link; if it was, the collision check with the mesh was performed again; if it was not, the classical traversal algorithm was performed again by taking the start point of the segment as the origin and stopping it if the point location function returned the index of the box leaf where the end point of the segment lay.

In Fig. 4.17 the performance in terms of computational time is highlighted, again comparing with the classical method shows that there are huge improvements of the order of 10^3 seconds, the simulations were carried out starting from a small number of rays up to 1000.

Fig. 4.18 instead, shows the result of a test performed using a time step of 0.2 s is a number of steps equal to 40 to generate the ray; as can be seen, the point of impact is highlighted in green and represents the correct operation of the algorithm.

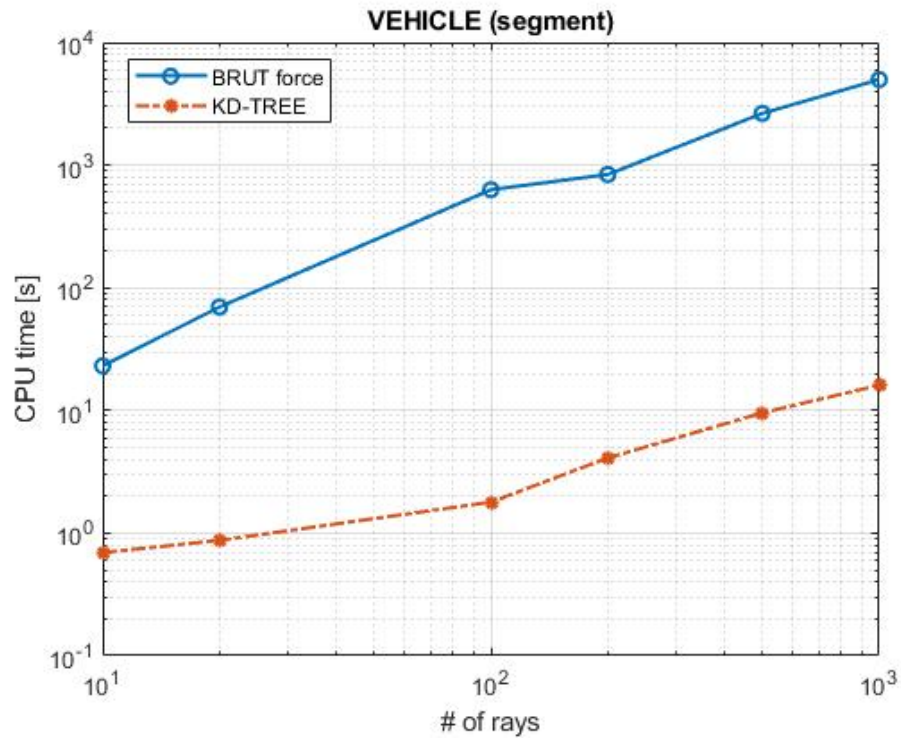


Figure 4.17: Benchmark for the segmented version of the Ray Tracing

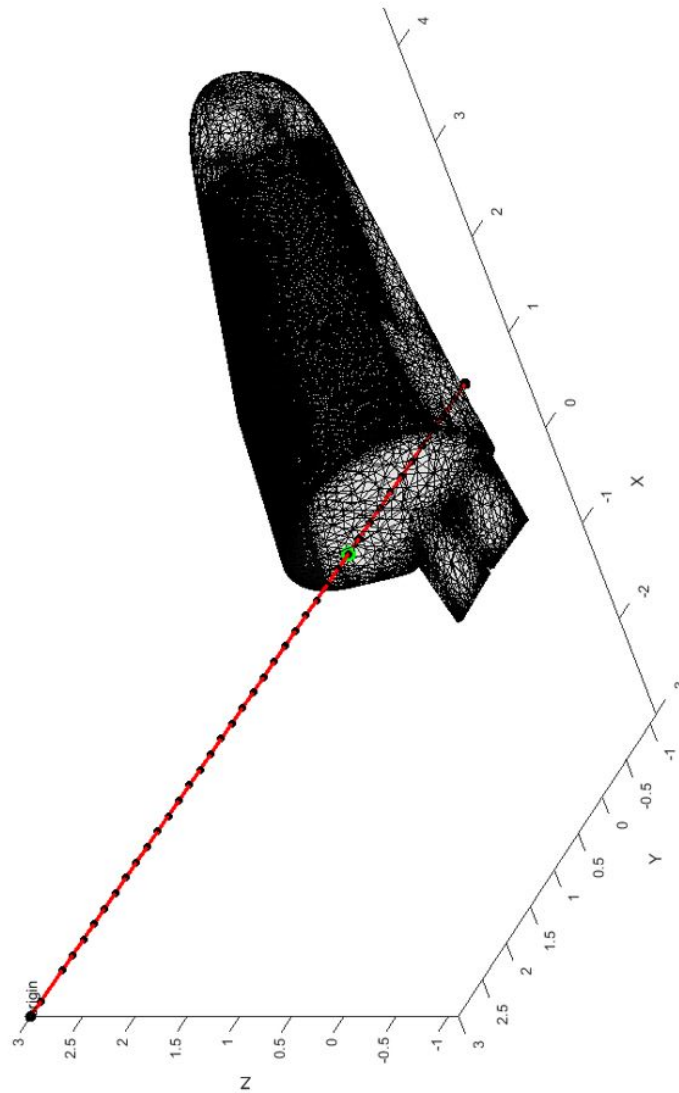


Figure 4.18: Testing the algorithm adapted to the segmented line. From the figure, the ray constructed using line segments can be seen and in green the point of impact with the geometry is highlighted confirming that the algorithm works correctly.

Chapter 5

Electromagnetic Scattering by Penetrable Dielectric using upgrated LACE RT Code

In the second part of this thesis work, improvements have been made directly on the code described in Chapter 3 in order to broaden physical situations that can be handled. In the original code, ray reflections were considered only on a completely reflective and impenetrable surface (PEC), whereas we wanted to consider the case of (possibly lossy) dielectric interface; by doing so, the rays will not only be reflected, but once the surface is impacted, wavefronts will be generated, one reflected and one refracted, in accordance with when described in the Chapter 2. In order to accomplish the above, several subroutines were added to the existing code; the main purpose is first to compute the reflection and transmission coefficients at the interface and consequently the amplitudes and directions of the transmitted and reflected field starting from a given incident field, once the computation of the trajectory of all primary rays is finished, the trajectories of the secondary rays are computed from appropriate initial conditions and so on. For validation of the correct operation of the code, homogeneous dielectric sphere was considered, and once the RCS was calculated, it was compared with the Mie series [4]. Detailed procedures and results will be discussed later in the chapter.

5.1 Formulation of the Scattering Problem

A dielectric, which is defined by the constitutive parameters ϵ and μ (or refractive index $n = \sqrt{\epsilon_r \mu_r}$) is illuminated by an incident plane wave in free space. The refractive index of the scatterer is assumed to be smoothly varying in the general case, or be homogeneous (as in our tests), except at the scatterer boundary. The goal is to determine the backscattered field (RCS).

To represent the incident plane wave, a large number of rays are shot toward the dielectric sphere following the ray tube approach used in the physical model of the LACE RT Code in order to discretize the wavefront of a plane wave [5].

The incident rays encounter the scatterer boundary and reflected and refracted rays are generated, i.e. at point 1 in Fig.5.1. The refracted rays propagate inside the object and eventually encounter the scatterer boundary (point 2 in Fig. 5.1). Again reflected rays and refracted rays are generated, except this time the refracted rays exit the scatterer while the reflected rays bounce off the boundary and remain inside the inhomogeneous object.

The intensities of the reflected rays become weaker after every bounce against the boundary and this process can be terminated after several bounces.

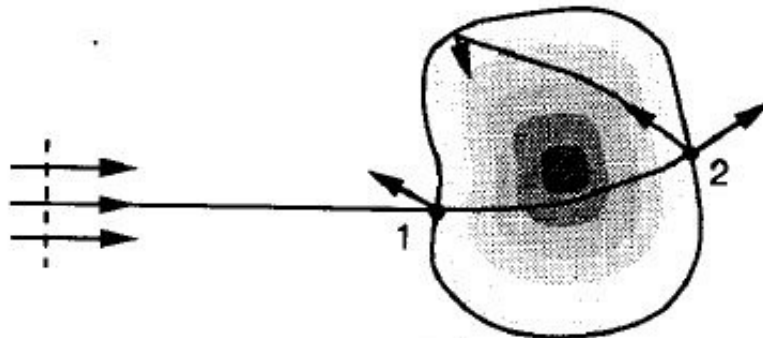


Figure 5.1: Geometry of the Scattering Problem

5.2 Reflection/Refraction at the Curved Scatterer Boundary

When a ray is incident upon the scatterer boundary, a reflected ray and a refracted ray are generated due to the discontinuity in the medium parameters. To determine the fields associated with the reflected and refracted rays as they propagate away from the boundary, their initial values including the ray directions, amplitudes, polarizations and wavefront curvatures are needed at the impact point.

The local coordinate system at the boundary used in order to take into account all these parameters is reported in the figure below:

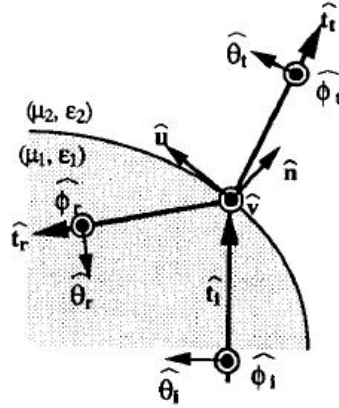


Figure 5.2: Local coordinate systems for the incident, reflected and refracted rays at the scatterer boundary.

The local coordinate system depicted in Fig.5.2 was taken from the literature[4] along with the respective decomposition of the incident field into its perpendicular and parallel components and the calculation of the amplitudes of the two transmitted and reflected fields.

Starting from a generic incident field decomposed into its parallel and perpendicular components as in [4]:

$$\underline{\mathbf{E}}_i = (\underline{\mathbf{E}}_i \cdot \hat{\phi}^i) \hat{\phi}^i + (\underline{\mathbf{E}}_i \cdot \hat{\theta}^i) \hat{\theta}^i \quad (5.1)$$

The reflected and transmitted fields at the impact point on the boundary are then obtained by using the planar reflection and transmission coefficients:

$$\underline{\mathbf{E}}_r = R_{\perp} (\underline{\mathbf{E}}_i \cdot \hat{\phi}^r) \hat{\phi}^r + R_{\parallel} (\underline{\mathbf{E}}_i \cdot \hat{\theta}^r) \hat{\theta}^r \quad (5.2)$$

$$\underline{\mathbf{E}}_t = T_{\perp} (\underline{\mathbf{E}}_i \cdot \hat{\phi}^t) \hat{\phi}^t + T_{\parallel} (\underline{\mathbf{E}}_i \cdot \hat{\theta}^t) \hat{\theta}^t \quad (5.3)$$

As for the reflection and transmission coefficients $R_{\perp}, R_{\parallel}, T_{\perp}, T_{\parallel}$ they are the same as those described in Chapter 2 which are recalled below for a lossy medium:

$$\begin{aligned}
 R_{\parallel} &= \frac{n_2 \cos \theta_i - n_1 \sqrt{1 - \frac{\epsilon_1}{\epsilon_2} \sin^2 \theta_i}}{n_2 \cos \theta_i + n_1 \sqrt{1 - \frac{\epsilon_1}{\epsilon_2} \sin^2 \theta_i}} \\
 R_{\perp} &= \frac{n_1 \sqrt{1 - \frac{\epsilon_1}{\epsilon_2} \sin^2 \theta_i} - n_2 \cos \theta_i}{n_1 \cos \theta_i + n_2 \sqrt{1 - \frac{\epsilon_1}{\epsilon_2} \sin^2 \theta_i}} \\
 T_{\parallel} &= (1 + R_{\parallel}) \frac{n_1}{n_2} \\
 T_{\perp} &= 1 + R_{\perp}
 \end{aligned} \tag{5.4}$$

In this case, ϵ_2 and consequently n_2 can be complex considering a lossy medium, and the transmission angle will become the 'true' angle of transmission given by the following expression[11]:

$$\theta_t = \arctan \left(\frac{\sqrt{\epsilon_1 \mu_1} \sin \theta_i}{\Re \left[\sqrt{\tilde{\epsilon}_2 \mu_2 - \epsilon_1 \mu_1 \sin^2 \theta_i} \right]} \right) \tag{5.5}$$

A more detailed description of the Fresnel equations applied to a lossy medium is given in Appendix D.

5.2.1 Numerical Simulation of Ray Trajectories

In Fig. 5.3 we show the calculated ray trajectories throughout a sphere with $\epsilon_r = 14$ with up to three interactions with the boundary interfaces.

Specifically, in red are indicated the rays incident to the first surface and those reflected on it, while in blue are indicated the rays transmitted after the first impact and those transmitted after the second impact (which will exit the sphere); finally, in black are indicated the reflected rays generated by the second impact with the surface of the sphere from the rays transmitted at the first interface. It can be seen that blue rays go to converge at a focal point that as described in Chapter 3 carries a phase shift of π .

The focal point of the black rays lays outside the scatterer.

These phase jumps generated in the focal points as in caustics must be correctly calculated to best reconstruct the radiated far field; for caustics arising outside the scatterer one solution to avoid taking them into account is to choose an appropriate distance of the equivalent surface, in this case it is chosen very close to that of the sphere so that the focal points fall outside it and the phase jumps do not affect the correct reconstruction of the far field.

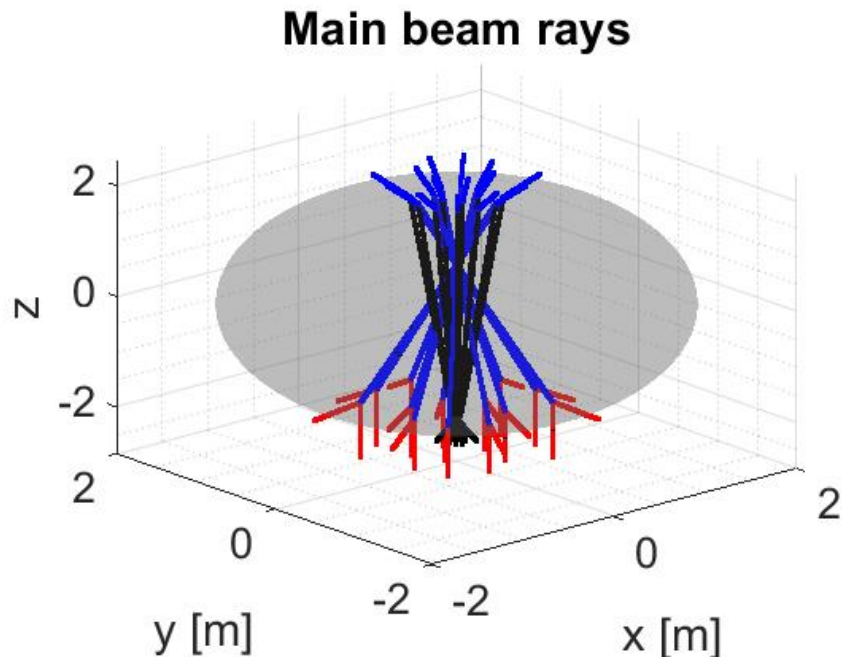


Figure 5.3: Results of simulation of ray reflections and refractions for an homogeneous dielectric sphere with $\epsilon_r = 14$. Two focal points can be seen: one inside the sphere generated by the the refracted wavefront at the first boundary; and one just outside the sphere generated by the wavefront encountering the boundaries three times and being transmitted-reflected-transmitted respectively.

5.3 Correct bookkeeping of rays

An important aspect to consider in order to have meaningful results is the proper bookkeeping of the rays. This is because each ray once it impacts the surface will generate two new rays that will both contribute to the far-field. Considering the numerical model implemented in the LACE RT code, the new trajectory of the reflected or transmitted ray will be calculated while the other will be saved in a data structure in memory and then, once the calculation of the trajectory of all the primary rays is finished, it will be taken from the latter and all the trajectory traveled will be calculated in turn; this procedure is also carried out one at a time on all the secondary rays generated by the first impact of the primary rays. The latter will in turn generate reflected and refracted rays, and the same bookkeeping criterion used previously will be applied. The energy associated with a primary ray will be splitted at each interaction with the boundary surface so that after a number of passes the secondary ray will carry a negligible amount of energy. Thus the process can be stopped after a specified number of reflections/transmissions or

when the associated energy goes below a threshold value. Another parameter that must be taken into account is the 'history' of each individual ray; this is because what you are going to 'follow' is the propagating wavefront (the rays represent the vertices of triangular patches used to discretize the wavefront); so once the rays are grouped by groups of three they must be of the same type: either all reflected or all transmitted, so that the transmitted or reflected wavefront can be reconstructed correctly. To overcome this problem, a vector was created containing codes representing the transmission or reflection of each ray. A schematic of the operation of the numeric code with the newly inserted modules is shown in the figure below.

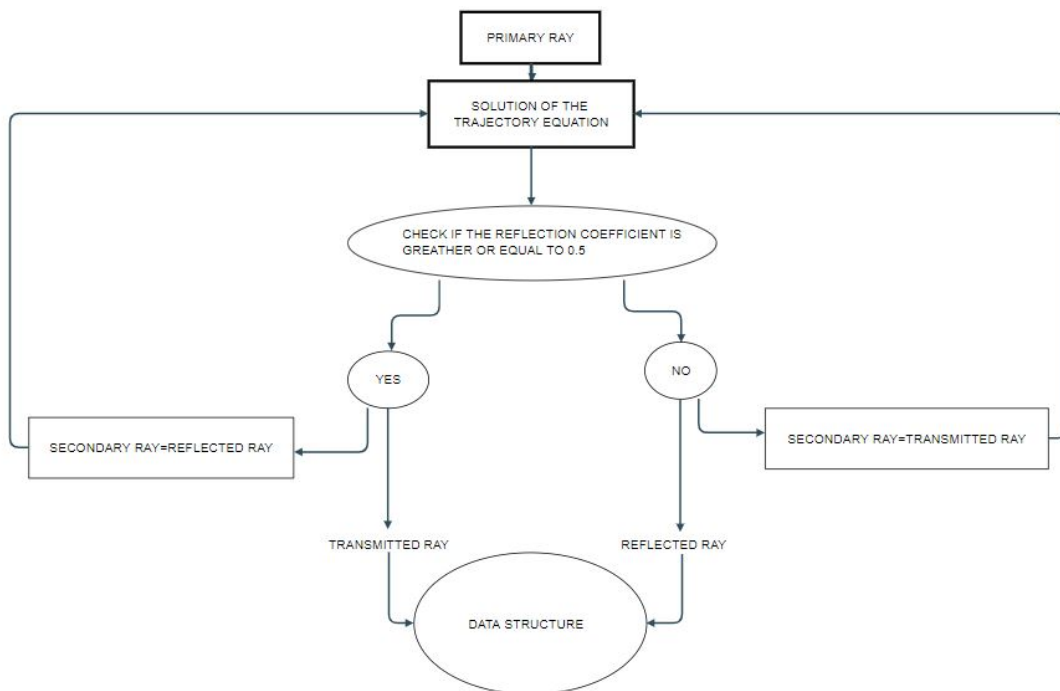


Figure 5.4: Schematic of the operation of the numerical code with the new modules.

5.4 Test Cases & Numerical Results

5.4.1 Dielectric With Losses

As a first test case for validating the proper functioning of the new subroutines inserted within the code, it was chosen to consider a material with high losses; meaning that the transmitted rays are completely absorbed before meeting the other surface and therefore the contribution to the RCS is made only by the reflected ones.

Considering the general expression of the dielectric permittivity of dissipative (lossy) materials:

$$\tilde{\epsilon} = \epsilon - j\frac{\sigma}{\omega} = \epsilon_0\epsilon_r - j\frac{\sigma}{\omega} \quad (5.6)$$

and considering dissipative media with conductivity equal to $\sigma = 7\epsilon_0\omega$, one obtain that the expression of the permittivity of the medium considered for this first test case is as follows:

$$\tilde{\epsilon} = \epsilon_0\epsilon_r - j\frac{\sigma}{\omega} = \epsilon_0\epsilon_r - j\frac{7\epsilon_0\omega}{\omega} = \epsilon_0(\epsilon_r - j7) \quad (5.7)$$

To test the applicability of the code by considering different types of materials, a scan on the relative permittivity (ϵ_r) was chosen starting from 0.1 up to 50 and taking the field value for $\theta = 0$ degrees (RCS Monostatic-backscattering) and taking as reference the same field given by Mie's series considering an electrical size of the object equal to $ka=35$.

The results are shown in the figure 5.4, and it can be seen that throughout the selected permittivity range the RCS values calculated using the numerical code almost perfectly follow those given by the Mie series theory going to justify a wide range of applicability of the code for different types of materials.

Once the correct operation of the code was ascertained for different permittivity values, a single value of it ($\epsilon_r = 2.2$) was selected and a scan on the electrical magnitude was performed.

The hybrid method used in the code (raggistic plus physical optics) had already been tested for a PEC [5] and the result was that for the simple case under consideration our method was equivalent to standard PO approximation (i.e. same results over the wavelength spectrum). For the dielectric what we wanted to show is that starting from the reference given in the literature on MECA[12] (Modified Equivalent Current Approximation, basically an extension of the PO method for penetrable dielectrics) it was seen that as the electrical magnitude of the object increases it tends to the exact solution given by the Mie series, but even in the areas where it is not asymptotically close to the exact solution the LACE RT Code

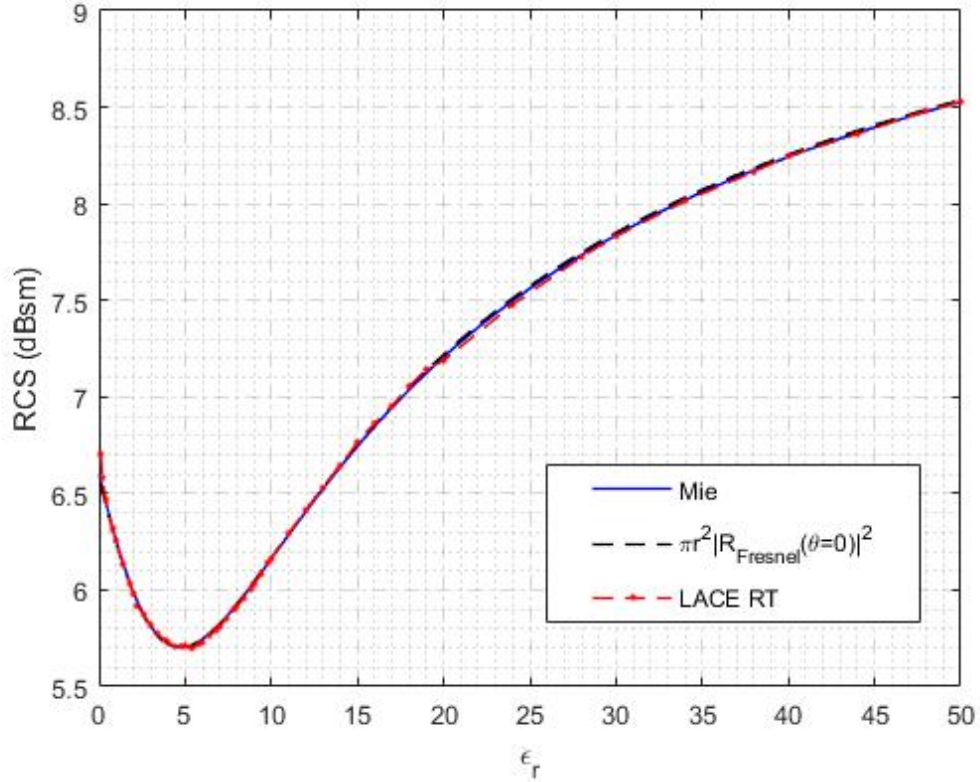


Figure 5.5: RCS for increasing ϵ_r and $ka=35$

gives solutions very similar to those given by MECA.

Fig.5.6 and 5.7 shows the results of the simulations, and what can be observed is that the results confirm what is expected since it has that as the electrical magnitude of the object increases, the results provided by the code tend to converge asymptotically to those given by the theory.

In order to compare the angular dependence (bistatic RCS) of the RCS with respect to the angle of observation between the results of the simulations and the exact ones provided by the series of Mie, a single permittivity ($\epsilon_r = 2.2$) and two electrical sizes ($ka=10;ka=35$) were selected.

The results of the simulations are shown in Figures 5.8-5.11.

What can be observed from the plots is that the described trend in Fig.5.7 is confirmed, because for $ka=10$ we have that the behavior of the bistatic RCS as the angle of observation varies differs from the exact behavior given by the Mie series much more than the case considered for $ka=35$ where, as verified above, there is an asymptotic approach to the exact solution. In both cases, however, the value of the

backscatterincg (RCS for $\theta = 0$) turns out to be practically exact and coincident with that given by theory.

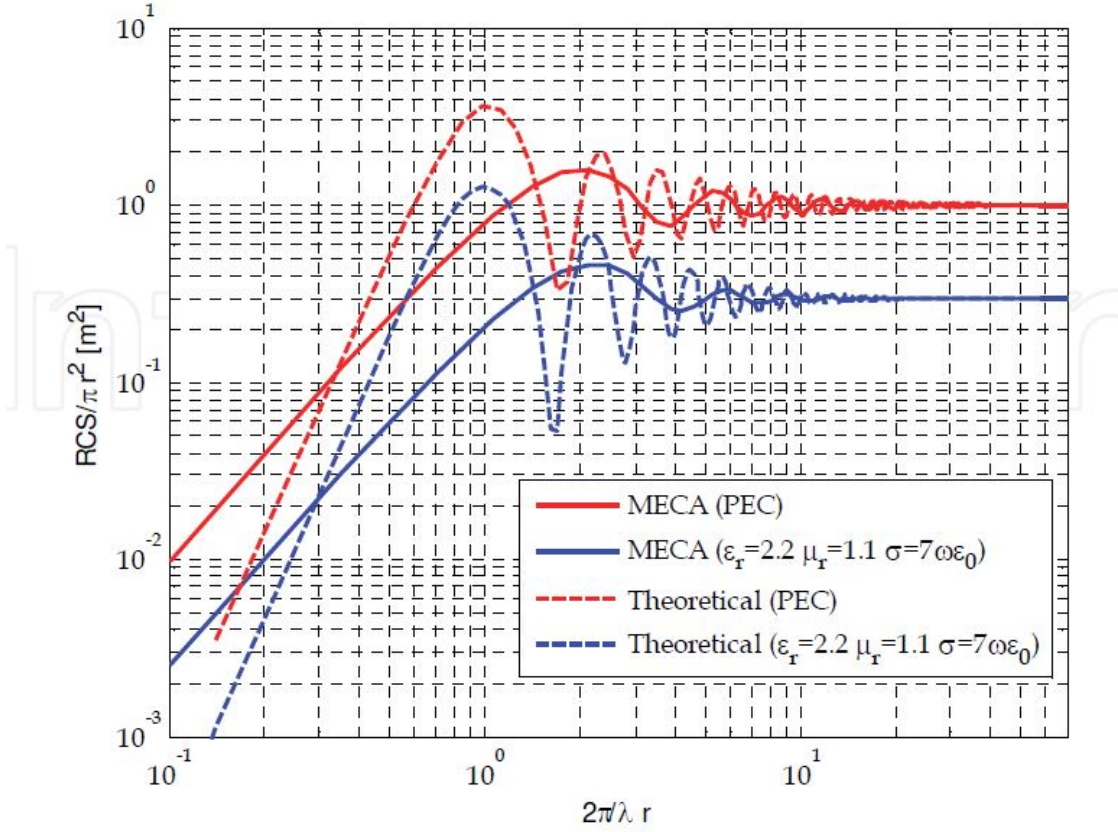


Figure 5.6: Monostatic RCS of a sphere. PEC and lossy characterization using the MECA method taken from [12]. An high degree of overlapping in the curves of Mie and MECA clearly demonstrates the accuracy of the high frequency technique.

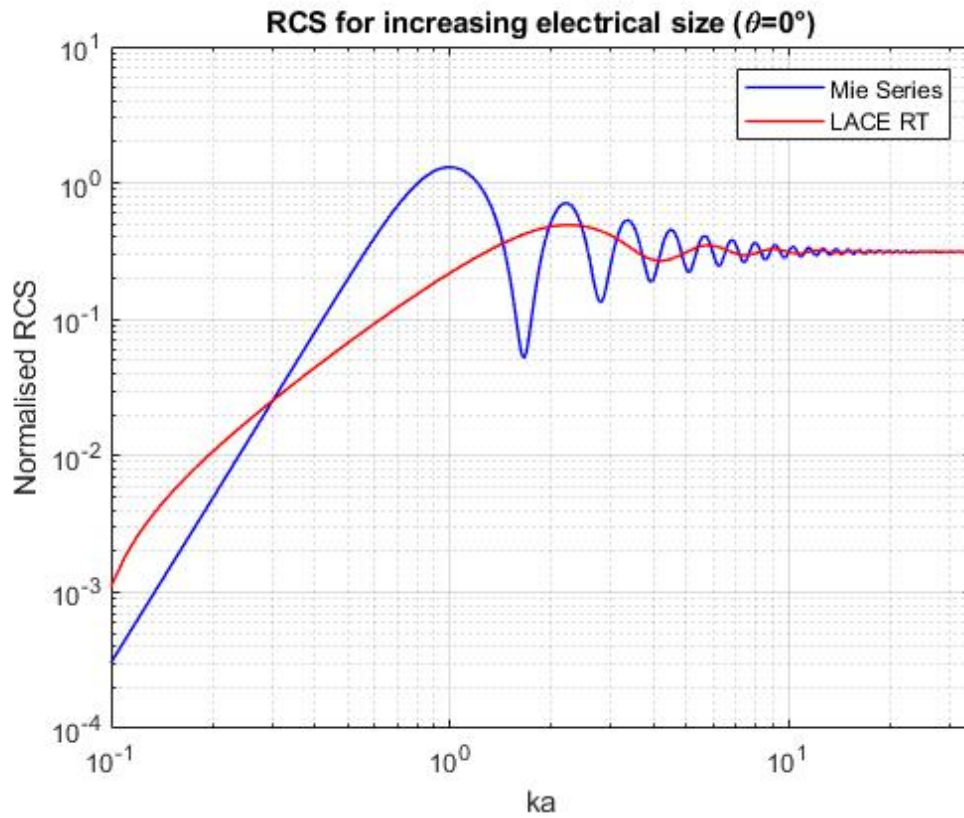


Figure 5.7: RCS comparison for increasing ka and fixed ϵ (2.2). The trend described turns out to be very similar to that in Fig. 5.6; this goes to confirm what was said earlier, namely, that even in areas where the solutions is not exact, the hybrid code tends to behave like the MECA numerical method for dielectrics and like the PO for PEC[5]

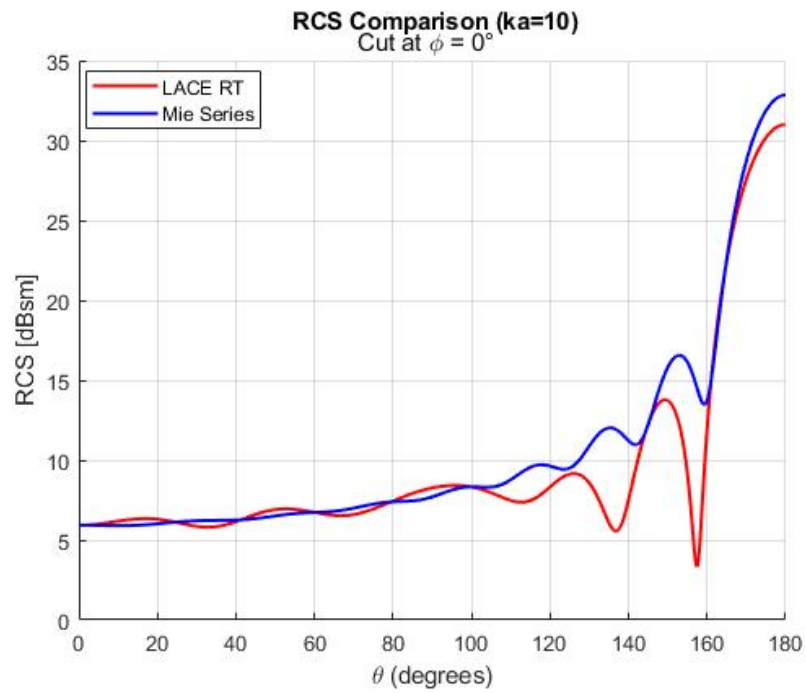


Figure 5.8: RCS comparison for ka=10 ($\phi = 0$); θ Polarization

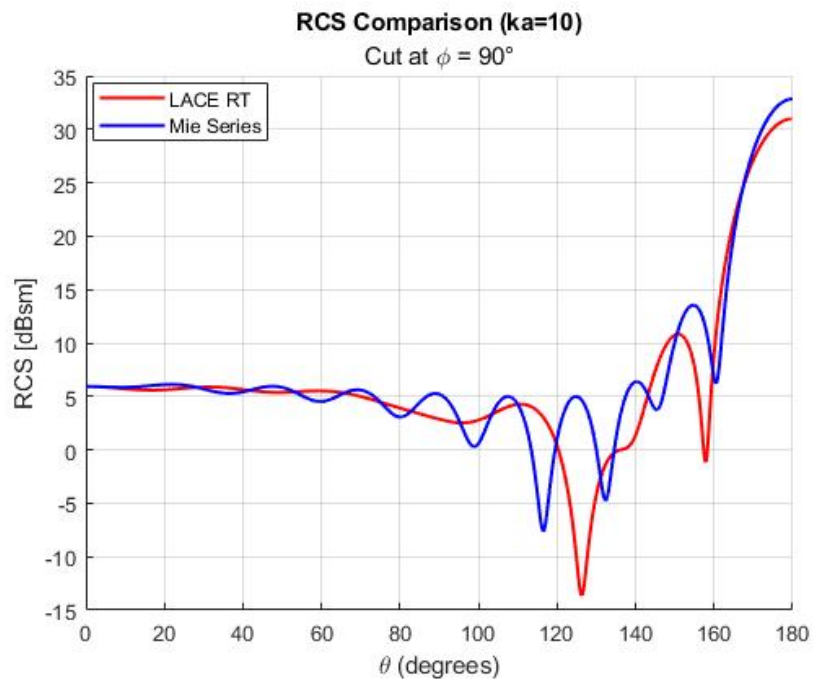


Figure 5.9: RCS comparison for ka=10 ($\phi = 90$); θ Polarization

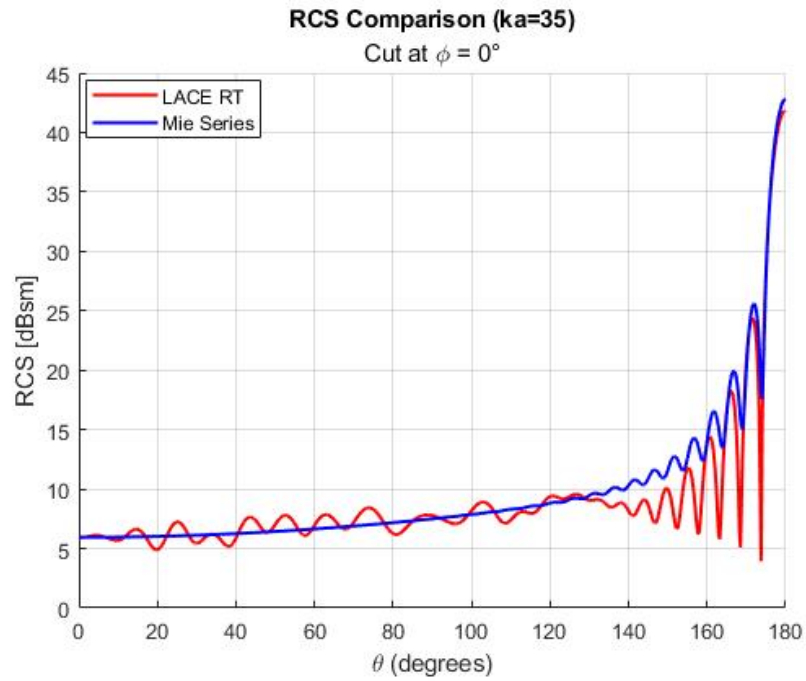


Figure 5.10: RCS comparison for $ka=35$ ($\phi = 0$); θ Polarization

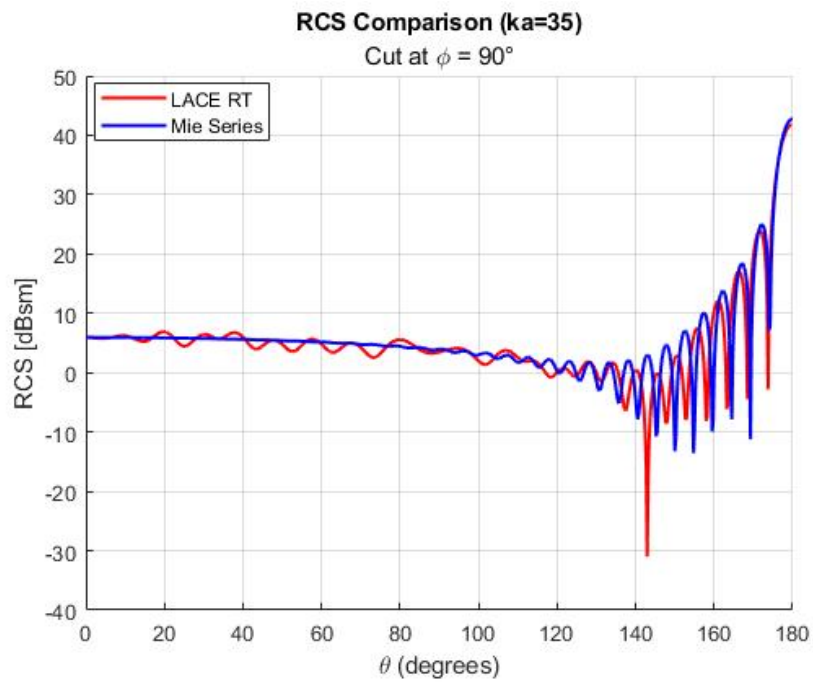


Figure 5.11: RCS comparison for $ka=35$ ($\phi = 90$); θ Polarization

5.4.2 Dielectric Without Losses

A lossless dielectric was chosen as the second test case; in this case we have an expression of the real permittivity therefore without an imaginary part. Specifically, the parameters chosen for the simulation were $\epsilon_r = 30, \epsilon_r = 14$ and an electrical sphere size of $ka = 31.44$.

The major difference with the previous test case is the fact that now the rays transmitted inside the interface are not absorbed by the material but reach the inner face of the sphere going on to generate another pair of rays.

Taking advantage of the data structure described earlier, it was chosen to follow three reflections of each ray: the first reflection on the first interface, the transmission inside the sphere, and the second reflection on the inner edge of the sphere. Proceeding in this way still managed to track more than 92% of the initial energy of the electromagnetic wave.

Referring back to Fig.5.3 and observing the ray trajectories, one can see focal points and caustics generated by reflections; as mentioned earlier, these physical phenomena generate wave phase jumps that must be correctly calculated in order to correctly reconstruct the radiated far field.

The method used in this test was to add phases to the entire wavefront for each front considered; then going to add or subtract the same phase to all the flux tubes constituting the entire wavefront.

After carrying out several tests considering different phases to be added, it was seen that making improvements on the back and forward scattering (the results of the simulations were very close to the exact solution) showed a worsening on the lateral part of the radiated field; while in the cases where the trend of the theoretical curves for the lateral field was followed almost perfectly, there was a worsening on the back and forward scattering.

The results of the simulations are shown in the figures 5.12-5.15.

Going on to investigate the possible causes of these worsening and complementary improvements led to the conclusion that in order to obtain a correct reconstruction of the field one must calculate the phases during the propagation of each individual flux tube and not apply a global phase on the entire wavefront; this procedure must be done on run within the code with the insertion of new subroutines.

Future work on further optimization of the numerical code can be done in this direction.

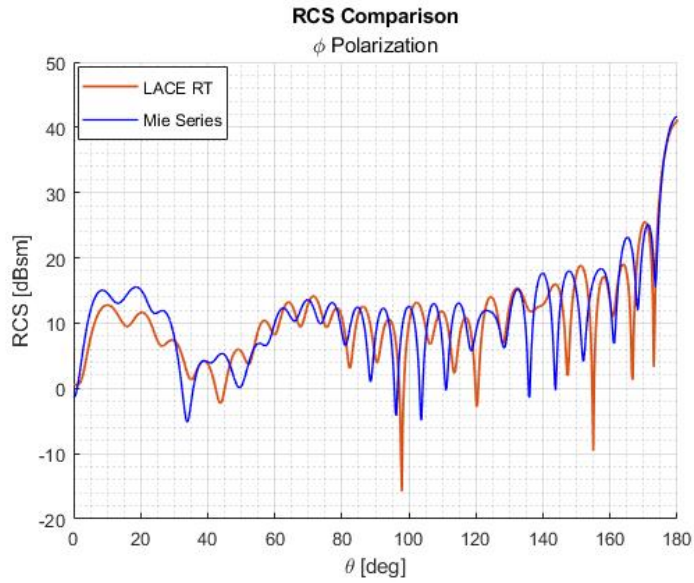


Figure 5.12: RCS comparison ($\epsilon_r = 30$) considering 3 reflections. Improvement can be observed in the calculation of back and forward scattering but a deterioration in the 'lateral' part of the field.

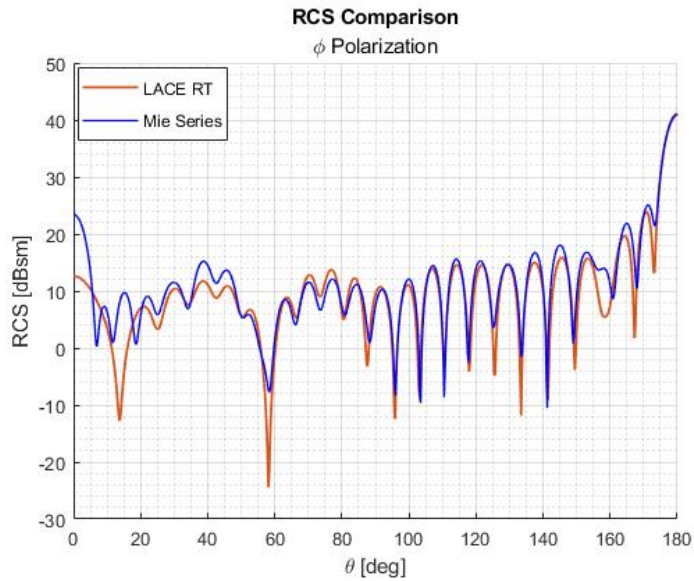


Figure 5.13: RCS comparison ($\epsilon_r = 14$) considering 3 reflections. Improvement can be observed in the calculation of the 'lateral' part of the field but a deterioration in back and forward scattering.

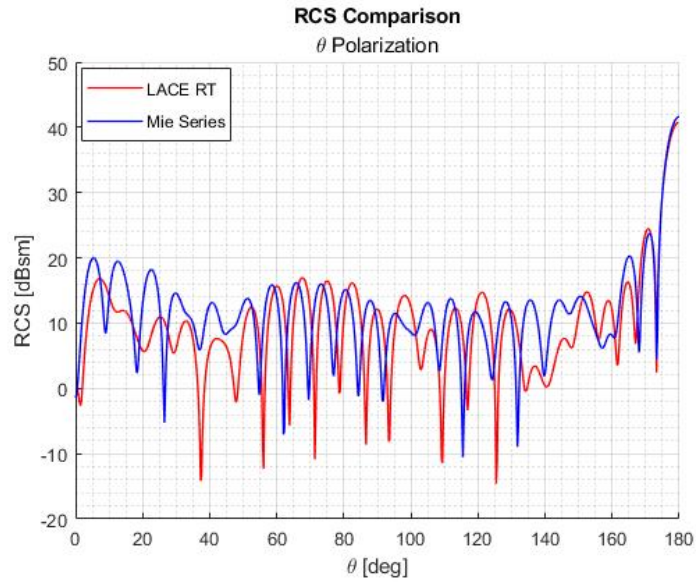


Figure 5.14: RCS comparison ($\epsilon_r = 30$) considering 3 reflections. Improvement can be observed in the calculation of back and forward scattering but a deterioration in the 'lateral' part of the field.

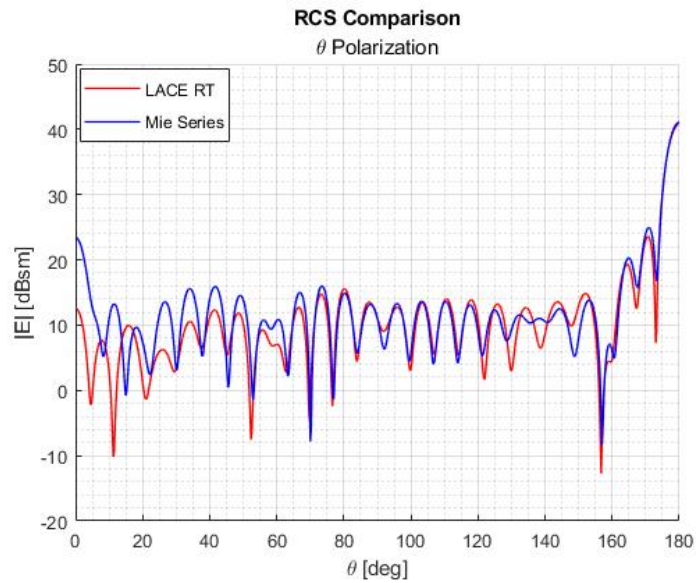


Figure 5.15: RCS comparison ($\epsilon_r = 14$) considering 3 reflections. Improvement can be observed in the calculation of the 'lateral' part of the field but a deterioration in back and forward scattering.

Chapter 6

Summary & Conclusions

Extreme heating of the air by strong shock waves during hypersonic atmospheric re-entry creates a plasma flow that blocks or strongly attenuates the radio frequency signal (RF black/brown-out). Several approaches have been explored in the past without finding a convincing direct solution to this well known disruption of RF communications in atmospheric re-entry. Clearly a way to minimise or remove the disruption would provide a significant advantage for future experiments and missions, allowing the transmission of more data and a safer control of the vehicle during a delicate phase or the re-entry. One possible solution to overcome this problem is to study the propagation of radio frequency waves within complex media such as the ionosphere, plasmas, and complex gas mixtures. Asymptotic techniques such as ray or beam tracing can be used to predict EM propagation in these inhomogeneous media where the radiation can be refracted, reflected and/or absorbed compared to free-space propagation.

The ray tracing method effectively decompose the wavefront with plane wave represented by one or more rays and follow the propagation using the Eikonal approximation valid for short wavelength. Contrary to ray tracing in homogeneous media, where the ray trajectories are straight lines, here a ray can be curved due to the continuous variation of the refractive index (inhomogeneity). One of the limitations of ray tracing (both for homogeneous and inhomogeneous cases) and consequently of the numerical code is the fact that in order to have reliable results, a sufficiently dense grid of rays must be generated which interacts with objects in the "scene" while traversing it (ray traversal); this involves an enormous amount of computational time.

The main purpose of this thesis work was to improve a numerical code developed at LINKS Foundation capable of using these asymptotic methods for two specific purposes:

1. Speeding up the ray traversal process; this was done by using special data

structures such as K-D Trees or Octrees that can subdivide the physical space (the scene) into boxes and then through an appropriate traversal algorithm identify which boxes were hit by the ray in such a way as to follow its trajectory.

2. Broaden physical situations that can be handled including penetrable dielectric and, in general, discontinuous dielectric interfaces.

Regarding the first part, a prototype was developed in MATLAB of the algorithm for the optimization of the Ray Traversal process; this is because in the classical (Brut Force) method of Ray Tracing, a check is made to find the intersection of the ray with each of the patches constituting the mesh of the geometry; leading to a very rapid increase in computational time as the complexity of the geometry and the density of the mesh increase. In the new algorithm, on the other hand, this check will be performed only on a small subset of patches that will be present within the boxes generated by dividing the volume of the space thanks to the aforementioned data structures. In a first step, a comparison was made on the two well-known partitioning methods based on Octree and Kd-tree structures; this comparison was made in terms of the number of levels (subdivisions) generated and the number of 'leaf' boxes i.e., the box containing a fixed number of points of the mesh of the geometry that constitutes the lowest level of the tree. Four different types of geometries with increasing complexity and number of patches were used to make this comparison; what was observed was that while with the use of the KD-Tree the number of levels and box leaves remained almost constant as the geometry increased, with the use of the Octree this was not the case and for complex geometries there was an explosion in the number of box leaves generated, bringing as a consequence a vast memory occupancy leading to the choice of the K-D Tree as the data structure to be used.

Once the subdivision of the space (scene) was implemented, we moved on to the actual traversal phase comprising two main algorithms: the Ray Traversal and its sub-part Point Location. It was chosen to compare 3 different versions of this algorithm: one that used the classical Point Location method (Sequential), one that used an new version of the Point Location called Integer Location inspired by a publication [13], in which a mapping matrix has been created that can directly output the index of the data structure corresponding to the box containing the point to be located, by simply selecting the corresponding matrix cell; and finally a structure that used another data structure called Neighbor Links in which all possible neighbors of each individual leaf node were stored so that the intersection check was performed on a smaller number of elements once the first leaf box was pierced by a ray. The algorithm was tested on a CAD model of the ESA re-entry vehicle (Intermediate eXperimental Vehicle) IXV, and testing all the three versions against the classical Brut Force one (in which the intersection check is performed on each individual patch constituting the mesh); the simulations were

carried out considering an increasing number of rays generated up to a maximum of 5000, and the results show that as the number of rays considered increases, all three optimization algorithms converge to the same performance and while they differ little by going to consider few rays. In general, we find an improvement in computational time of $10^2 - 10^3$ was obtained in the region of performance convergence.

Once the algorithm had been successfully tested on the classical rays represented with straight lines; we adapted the method for the case of curved rays (as they in inhomogeneous media) represented by a segmented line. In this way it is possible to model the curved trajectories that rays assume during propagation in this type of media and build the trajectories one step at a time.

The adapted algorithm works by going forward along the trajectory one step at a time and checking the intersection between a single segment and a patch (the check on the intersection is no longer of the line-triangle type), if there is a successful intersection we move on to the next ray, if not, one goes to see in which box leaf the end point of the current segment falls, if it is one of the neighbors of the previous box one again performs the intersection test with the patches contained in the neighboring boxes, if not one starts with the Ray Traversal for straight lines by having it stop in the box leaf where the end point of the current segment lies.

Significant improvements in computational time (on the order of 10^3) were also found in this version of the algorithm; comparison was made with a Brut Force method also adapted to segmented lines.

Future work inherent in this first part involves incorporating this algorithm within the Fortran90 code developed at LINKS Foundation so that simulation time can be optimized and speeded up.

In the second part, on the other hand, enhancements were made directly to the numerical code and in particular to the physical model used. In the original code the ray reflections were considered only on a completely reflective and impenetrable material (PEC), what was desired was to also consider the impact of the rays on a penetrable object; this leading to the generation of a second ray at each intersection with the dielectric interface. The generation of this second ray is governed by Snell's laws of reflection and refraction. Considering the rays as constituent elements of the wavefront of a plane wave, we made use of Fresnel's formulas to calculate the reflection and transmission coefficients at the interface and consequently calculate the respective amplitudes of the transmitted and reflected fields. In this regard, several subroutines were added to the original source code capable of decomposing the incident field at the interface and calculating the respective reflection and transmission coefficients and then reconstructing the reflected and transmitted fields; and other routines capable of deciding which of the two generated beams to follow and saving the other in memory and then restarting with ray tracing from it once all the primary beams to follow are finished (rays book-keeping).

To validate the proper functioning of the new features, it was chosen to consider a sphere with constant dielectric properties. Two test cases were chosen for validation of the correct operation of the code. A first one considering a lossy dielectric and assuming that all rays entering the surface were absorbed by the material and the contribution of the far field was given only by the reflections on the first interface; two scans were carried out on the permittivity parameters prime and electrical size (equivalent to a frequency or wavelength scan) after, the first was carried out by fixing the losses and going to vary the real part of permittivity in such a way as to verify the applicability of the code for different types of materials, all of which was confirmed by simulations after being compared with the exact scattering solution given by Mie's series; the second on the other hand was carried out by going to fix the permittivity and losses, what was observed is that as for PEC also for dielectric the hybrid method (raggistic plus PO) implemented within the code as the electrical magnitude of the object increases tends to the exact solution given by the theory and in the regions where the solutions do not converge it behaves like a pure PO method for PEC and to its extension for penetrable dielectric called MECA method. A second test case going to consider a lossless dielectric and thus multiple ray reflections, in particular we focused on 3 reflections and still managed to follow more than 92% of the initial energy. What was seen from the results is that by analyzing the ray trajectories, focal points and caustics are formed that go to cause phase jumps to be properly calculated to reconstruct as faithfully as possible the radiated field.

Future work can be directed toward further optimizing the code in terms of calculating phase on each individual flux tube and not applying a constant phase shift over the entire wavefront.

Appendix A

Discussion on Eikonal validity for inhomogeneous media

The necessary condition for the applicability of the ray theory can be cast into the following relations:

$$\delta \equiv \frac{|\nabla \log(|\epsilon_r|)}{k_0} \ll 1 \quad (\text{A.1})$$

$$\frac{|\nabla \log(|\mathbf{E}|)}{k_0} \ll 1 \quad (\text{A.2})$$

$$\frac{\text{Im}(\epsilon_r)}{\text{Re}(\epsilon_r)} \sim \delta \quad (\text{A.3})$$

The first two demand the properties of the medium and the wave amplitude to vary slowly over the distance of a wavelength (i.e. weakly dependent on the spatial coordinate r). The last equation requires a weak energy exchange between the media and the EM wave and partly overlaps with eq. A.2. As well known, these conditions are typically violated near caustics (even in free-space), cut-off and resonance regions. In an inhomogeneous media, a high density, high gradient region may be generated and cut-off layers may appear. The ray is expected to suffer reflection at cut-off, since the wave is evanescent on the other side. Actually, reflection must occur before the cut-off is reached. Indeed, for oblique propagation, only the component of k parallel to the density gradient goes to zero, whereas the group velocity is still well defined. This kind of reflection does not lead to a global breakdown of the Eikonal approximation, but is associated with the formation of a

caustic or of a focal point, so that some care has to be taken in the determination of the phase along the ray. Thus, even in this extreme case, a good approximation is expected away from the cut-off layer (i.e. at the equivalent surface).

Appendix B

Octree/K-D Tree comparison for different geometries

Below are plots of the volume division around the considered object as described in Chapter 4. The data structure construction algorithms used were the K-D Tree and the Octree.

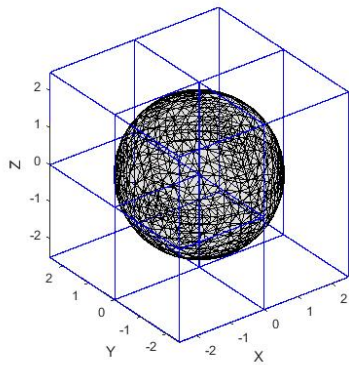


Figure B.1: K-D Tree Sphere

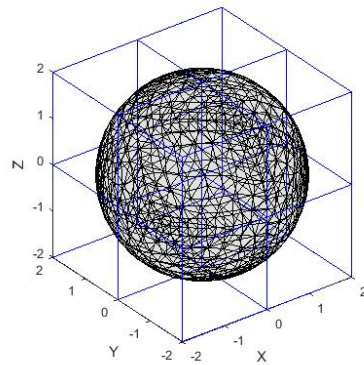


Figure B.2: Octree Sphere

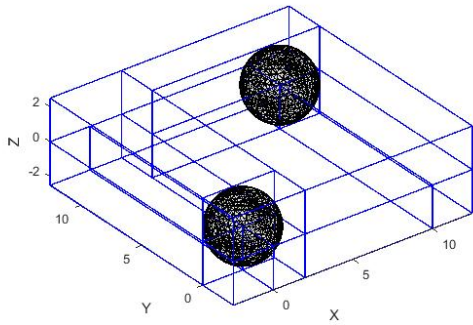


Figure B.3: K-D Tree 2 Spheres

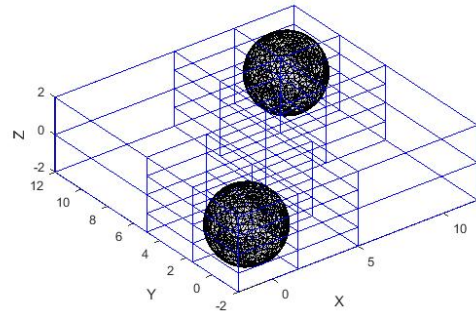


Figure B.4: Octree 2 Spheres

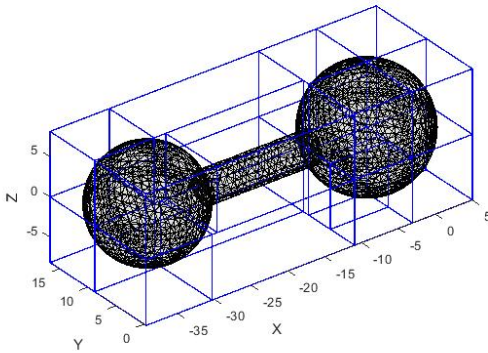


Figure B.5: K-D Tree Spheres & Cylinder

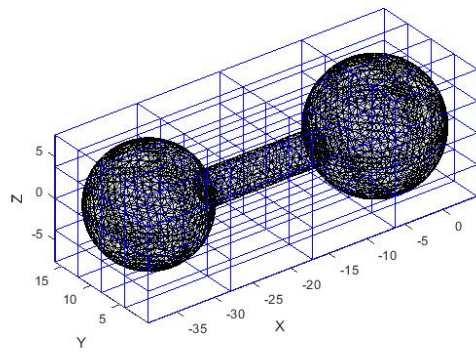


Figure B.6: Octree Spheres & Cylinder

Appendix C

Benchmark of Numerical Model

The simulation results for the remaining geometries are shown below; they exhibit similar behaviors as seen for the vehicle except for the single sphere where the algorithm where Integer Location was used seems to have even better performance.

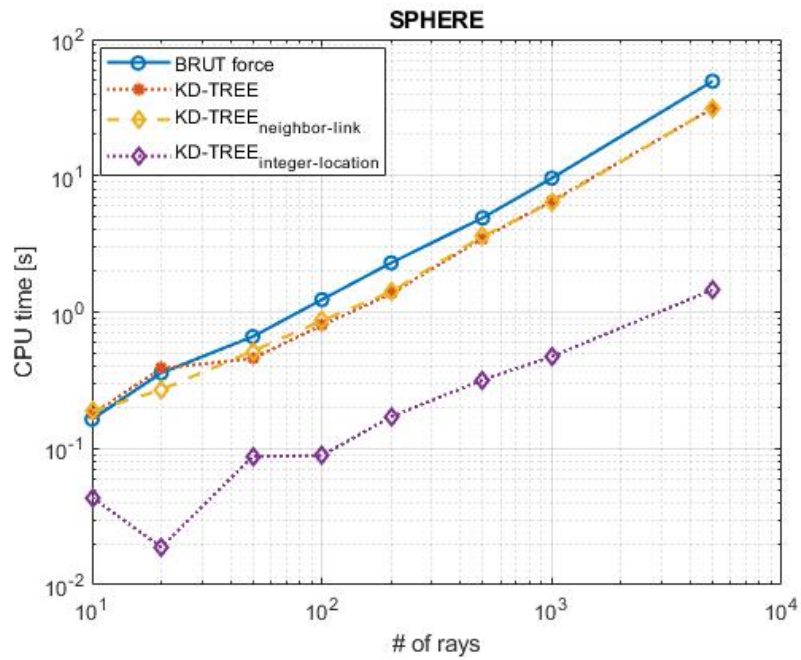


Figure C.1: Computational Time Performance (Sphere)

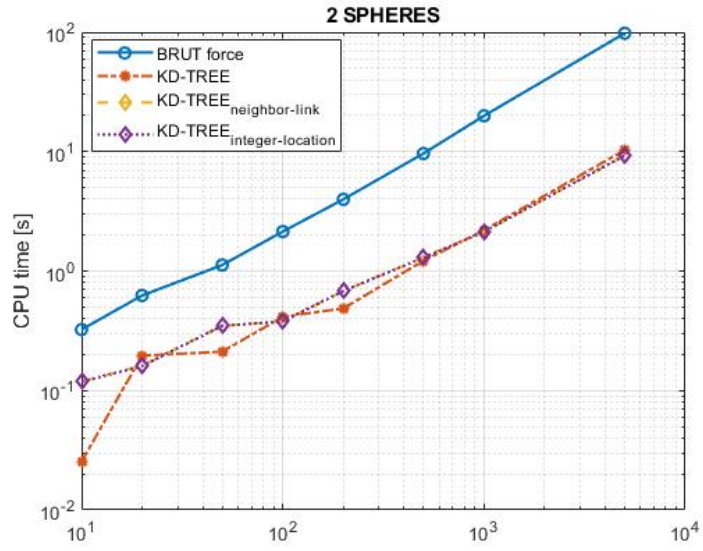


Figure C.2: Computational Time Performance (2 Sphere)

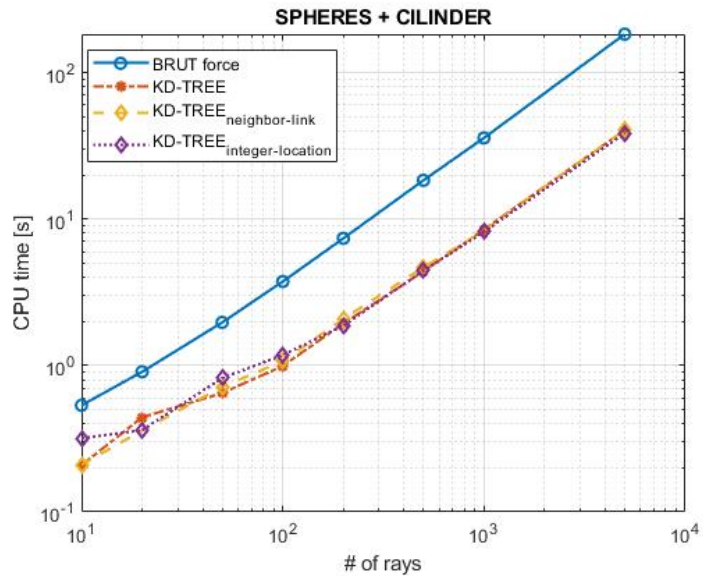


Figure C.3: Computational Time Performance (Sphere & Cylinder)

Appendix D

Fresnel Coefficients for Lossy Materials

Consider a uniform plane wave in medium 1 impinging obliquely on medium 2, characterized by finite conductivity and occupying the region $z \geq 0$. Medium 1 is described by a wavenumber $\beta_1 = \omega\sqrt{\epsilon_1\mu_1}$, expressed in terms of the angular frequency ω , the real permittivity ϵ_1 , and the real permeability μ_1 . Medium 2 is a lossy dielectric with complex wavenumber given by

$$\beta_2 = \omega\sqrt{\epsilon_2\mu_2} = \omega\sqrt{\mu_0\mu_2\epsilon_0\epsilon_{2r}} = \frac{\omega}{c}\sqrt{\mu_{2r}(\epsilon'_{2r} + i\epsilon''_{2r})} \quad (\text{D.1})$$

where c is the speed of light in vacuum, μ_{2r} is the relative permeability of medium 2 (assumed to be real), and ϵ'_{2r} and ϵ''_{2r} are respectively the real and imaginary part of the complex relative permittivity of the second medium.

D.1 TE Polarization

It is assumed that the incident electric-plane field in medium 1 is linearly polarized in the positive y direction, and propagates along the incident wave vector $\underline{\beta}_i = \beta_1(\sin\theta_i\hat{x} + \cos\theta_i\hat{z})$, where θ_i is the angle of incidence and the caret sign denotes a unit vector. The incident electric field and its corresponding magnetic field are thus given as:

$$\underline{E}_i = \hat{y}E_0e^{i\underline{\beta}_i \cdot \underline{r}} \quad (\text{D.2})$$

$$\underline{H}_i = \frac{1}{i\omega\mu_1}\nabla \times \underline{E}_i \quad (\text{D.3})$$

suppressing and $e^{-i\omega t}$ time dependence. The reflected fields in medium 1 and the transmitted fields in medium 2 are given as follows[11]:

$$\underline{E}_r = \hat{y}E_0\Gamma_{TE}e^{i\beta_r \cdot r} \quad (D.4)$$

$$\underline{H}_r = \frac{1}{i\omega\mu_1}\nabla \times \underline{E}_r \quad (D.5)$$

$$\underline{E}_t = \hat{y}E_0\tau_{TE}e^{i\beta_t \cdot r} \quad (D.6)$$

$$\underline{H}_t = \frac{1}{i\omega\mu_1}\nabla \times \underline{E}_t \quad (D.7)$$

Here:

$$\underline{\beta}_r = \beta_1(\sin \theta_r \hat{x} - \cos \theta_r \hat{z}) \quad (D.8)$$

and

$$\underline{\beta}_t = \beta_2(\sin \theta_t \hat{x} + \cos \theta_t \hat{z}) \quad (D.9)$$

are respectively the reflection and transmission wave vectors, involving the real angle of reflection θ_r and the complex angle of refraction θ_t ; Γ_{TE} is the fresnel **reflection** coefficient, and τ_{TE} is the Fresnel **transmission** coefficient.

Following the standard approach of equating the tangential components of the total electric and magnetic fields at the interface $z=0$ results in equality of the angle of reflection and the angle of incidence, the "complex" Snell's law:

$$\beta_1 \sin \theta_i = \beta_2 \sin \theta_t \quad (D.10)$$

and the Fresnel reflection and transmission coefficients:

$$\Gamma_{TE} = \frac{\mu_2\beta_1 \cos \theta_i - \mu_1\beta_2 \cos \theta_t}{\mu_2\beta_1 \cos \theta_i + \mu_1\beta_2 \cos \theta_t} \quad (D.11)$$

$$\tau_{TE} = \frac{2\mu_2\beta_1 \cos \theta_i}{\mu_2\beta_1 \cos \theta_i + \mu_1\beta_2 \cos \theta_t} \quad (D.12)$$

D.2 TM Polarization

It is assumed that the incident magnetic field in medium 1 is linearly polarized in the positive y direction, and propagates along the incident wave vector $\underline{\beta}_i = \beta_1(\sin \theta_i \hat{x} + \cos \theta_i \hat{z})$. The incident magnetic field and its corresponding electric field are thus given as follows:

$$\underline{H}_i = \hat{y} H_0 e^{i \underline{\beta}_i \cdot \underline{r}} \quad (\text{D.13})$$

$$\underline{E}_i = \frac{1}{-i\omega\epsilon_1} \nabla \times \underline{H}_i \quad (\text{D.14})$$

The reflected fields in medium 1 and the transmitted fields in medium 2 are expressed as:

$$\underline{H}_r = \hat{y} H_0 \Gamma_{TM} e^{i \underline{\beta}_r \cdot \underline{r}} \quad (\text{D.15})$$

$$\underline{E}_r = \frac{1}{-i\omega\epsilon_1} \nabla \times \underline{H}_r \quad (\text{D.16})$$

$$\underline{H}_t = \hat{y} H_0 \tau_{TM} e^{i \underline{\beta}_t \cdot \underline{r}} \quad (\text{D.17})$$

$$\underline{E}_t = \frac{1}{-i\omega\epsilon_2} \nabla \times \underline{H}_t \quad (\text{D.18})$$

where $\underline{\beta}_r, \underline{\beta}_t, \theta_r$ and θ_t are defined as in the TE-polarization case.

Equating the tangential components of the total electric and magnetic fields at the interface $z=0$ yields the equality of the angle of reflection and the angle of incidence, Snell's law and the Fresnel reflection and transmission coefficients:

$$\Gamma_{TM} = \frac{\epsilon_2 \beta_1 \cos \theta_i - \epsilon_1 \beta_2 \cos \theta_t}{\epsilon_2 \beta_1 \cos \theta_i + \epsilon_1 \beta_2 \cos \theta_t} \quad (\text{D.19})$$

$$\tau_{TM} = \frac{2\epsilon_2 \beta_1 \cos \theta_i}{\epsilon_2 \beta_1 \cos \theta_i + \epsilon_1 \beta_2 \cos \theta_t} \quad (\text{D.20})$$

D.3 True Angle of Refraction

From the complex Snell's law given in Equation D.11, it follows that:

$$\beta_2 \cos \theta_t = \beta_2 \sqrt{1 - \sin^2 \theta_i} = \sqrt{\beta_2^2 - \beta_1^2 \sin^2 \theta_i} \equiv p + iq \quad (\text{D.21})$$

where p and q are real quantities, and $q > 0$. Consequently, the exponential term associated with the refracted fields in either polarization can be rewritten as:

$$\begin{aligned} e^{i\beta_t \cdot r} &= \\ e^{i\beta_2(x \sin \theta_t + z \cos \theta_t)} &= \\ e^{i[x\beta_1 \sin \theta_i + z(p+iq)]} &= \\ e^{-qz} e^{i(x\beta_1 \sin \theta_i + pz)} & \end{aligned} \quad (\text{D.22})$$

The surfaces of constant amplitude are defined as $qz = \text{constant}$; thus, the wave decays along the positive z direction. On the other hand, the surfaces of constant phase are given by the planes $x\beta_1 \sin \theta_i + pz = \text{constant}$. The true (real) angle of refraction is then defined as follows:

$$\theta_t = \arctan \left(\frac{\beta_1 \sin \theta_i}{p} \right) \quad (\text{D.23})$$

Using the notation introduced in Eq. D.23, the Fresnel coefficients for both polarizations are rewritten as follows:

$$\Gamma_{TE} = \frac{\mu_2 \beta_1 \cos \theta_i - \mu_1 (p + iq)}{\mu_2 \beta_1 \cos \theta_i + \mu_1 (p + iq)} \quad (\text{D.24})$$

$$\tau_{TE} = \frac{2\mu_2 \beta_1 \cos \theta_i}{\mu_2 \beta_1 \cos \theta_i + \mu_1 (p + iq)} \quad (\text{D.25})$$

$$\Gamma_{TM} = \frac{\beta_1 \cos \theta_i - \frac{\epsilon_1}{\epsilon_2} (p + iq)}{\beta_1 \cos \theta_i + \frac{\epsilon_1}{\epsilon_2} (p + iq)} = \frac{\sqrt{\epsilon_1 \mu_1} \cos \theta_i - \frac{\omega \epsilon_1 \mu_2}{\beta_2^2} (p + iq)}{\sqrt{\epsilon_1 \mu_1} \cos \theta_i + \frac{\omega \epsilon_1 \mu_2}{\beta_2^2} (p + iq)} \quad (\text{D.26})$$

$$\tau_{TM} = \frac{2\beta_1 \cos \theta_i}{\beta_1 \cos \theta_i + \frac{\epsilon_1}{\epsilon_2} (p + iq)} = \frac{2\sqrt{\epsilon_1 \mu_1} \cos \theta_i}{\sqrt{\epsilon_1 \mu_1} \cos \theta_i + \frac{\omega \epsilon_1 \mu_2}{\beta_2^2} (p + iq)} \quad (\text{D.27})$$

Bibliography

- [1] M. Born and E. Wolf. *Principles of Optics*. sixth edition. Vol. 6. Pergamon, 1980 (cit. on p. 3).
- [2] John David Jackson. *Classical Electrodynamics*. Wiley, 2018 (cit. on p. 25).
- [3] G. Ruck. *Radar Cross Section Handbook*. Plenum Press, 1970 (cit. on p. 26).
- [4] H. Kim and L. Ling. «Electromagnetic Scattering by Inhomogeneous Object by Ray Tracing». In: *IEEE Transactions on Antennas and Propagation* 40.5 (May 1992), pp. 512–525. DOI: 10.1109/8.142626 (cit. on pp. 34, 38, 68, 70).
- [5] «Radiation and Scattering of EM Waves in Large Plasmas Around Objects in Hypersonic Flight». In: *IEEE Transactions on Antennas and Propagation* 70 (2022) (cit. on pp. 36, 69, 74, 77).
- [6] H. Lin Y. B. Tao and H. J. Bao. «KD-TREE BASED FAST RAY TRACING FOR RCS PREDICTION». In: *Progress In Electromagnetics Research PIER* 81 (2008), pp. 329–341 (cit. on p. 45).
- [7] Lei Zhao Xin Yang Duan-qing Xu. «A fast SAH-based construction of Octree». In: () (cit. on p. 46).
- [8] M.Hapala and V. Havran. «Review: Kd-tree Traversal Algorithms for Ray Tracing». In: *Journal compilation* 30.1 (Nov. 2011), pp. 199–213 (cit. on pp. 52–54).
- [9] J.Amanatides and A.Woo. «A Fast Voxel Traversal Algorithm for Ray Tracing». In: *Jopurnal compilation* () (cit. on p. 59).
- [10] E.Haines and T.Hakenine Moller. *Ray Tracing Gems*. Apress Open, 2021 (cit. on p. 59).
- [11] «Comment on the 'Corrected Fresnel Coefficients for Lossy Materials». In: *IEEE Antennas and Propagation Magazine* 53.4 (Aug. 2011) (cit. on pp. 71, 94).

- [12] José Á. Martínez-Lorenzo Javier Gutiérrez-Meana and Fernando Las-Heras. «High Frequency Techniques: the Physical Optics Approximation and the Modified Equivalent Current Approximation (MECA)». In: (2011) (cit. on pp. 74, 76).
- [13] S.F.Frisken and R.N.Perry. «Simple and Efficient Traversal Method for Quadrees and Octrees». In: *Journal Compilation* (Nov. 2002) (cit. on p. 84).